GEOMECHANICS MODEL FOR WELLBORE STABILITY ANALYSIS IN FIELD “X” NORTH SUMATRA BASIN

by

Aidil Adham

A thesis submitted to the Faculty and the Broad of Trustees of the Colorado School of Mines in partial fulfillment of the requirements for the degree of Master of Science (Petroleum Engineering).

Golden, Colorado

Date ____________________________

Signed: _____________________

Aidil Adham

Signed: _____________________

Dr. Azra N. Tutuncu

Thesis Advisor

Golden, Colorado

Date ____________________________

Signed: _____________________

Dr. Erdal Ozkan

Professor and Head

Petroleum Engineering Department

ABSTRACT

Wellbore instability problems significantly increase the cost of drilling and operations in the oil and gas industry. These problems can occur in a variety of forms including stuck pipe, loss circulation, hole enlargement, unintentionally induced tensile fractures or difficult directional control incidents. In this research, we investigate the wellbore instability issues in Field “X”, a mature oil and gas sandstone reservoir located in North Sumatra, Indonesia. An integrated wellbore-stability study was implemented to help avoid wellbore instability problems in this field.

To narrow down the possible causes of wellbore instabilities in this field, a problem-diagnostic scheme was done by analyzing well log data, drilling reports, mud logging reports, and pore pressure measurements. The availability of data is the main problem in developing a good geomechanical model. Numerous methods for data acquisition were discussed in this study to gather reliable geomechanics data as inputs for the model, especially log based methods.

Geomechanics model was coupled with mechanical stress, temperature alteration, chemical iteration effects, and flow induced stress using Mohr-Coulomb and Mogi-Coulomb failure criteria. A numerical model was built using MATLAB programming software that results in the critical mud weight to avoid wellbore breakout and tensile failure in arbitrary wellbore inclination and azimuth.

TABLE OF CONTENTS

LIST OF FIGURES

LIST OF TABLES

ACKNOWLEDGEMENTS

I would like to thank my thesis advisor Dr. Azra Tutuncu, who has supported me throughout this research, without her guidance and support this research would not have been possible to complete. I would also like to thank my committee members, Dr. Erdal Ozkan and Dr. Mark Miller for their time and feedback with this research.

I would like to thank my sponsor, PT. Pertamina (Persero) for the financial means to conduct this study and providing me the data for this study. I would also like to thank my colleagues, the graduate students from the Petroleum Engineering department and PERMIAS student organization, for their support and help.

CHAPTER 1

INTRODUCTION

1.1 Motivation

Wellbore instability problems bring significant cost increases to drilling operations. These problems can occur in a variety of forms including stuck pipe, loss circulation, hole enlargement, unintentionally induced tensile fractures or difficult directional control incidents. In severe conditions, wellbore instability can increase non-productive time and create simultaneous occurrences of multiple instability incidents, which potentially can lead to losing the well if they are not handled with proper mitigation.

Wellbore instability is a function of imbalance in the required wellbore pressure applied and the fluid pressure in the formation, in addition to chemical interactions between the formation and the drilling or completion fluids, and interactions between these fluids and native formation fluid. Deviation and azimuth of the well also influence the wellbore stability as the stress distribution around the wellbore is dependent on the orientation of the wellbore, with respect to the in-situ stresses and the hoop stresses introduced through drilling the wellbore. To avoid wellbore instability problems in drilling, a proper well design needs to be developed for the formations to be drilled and completed for production, which requires understanding of the in-situ stress state, pore pressure, and geomechanical properties of the reservoir formation.

In this research study, we investigate the wellbore instability issues in Field “X”, a mature oil and gas sandstone reservoir located in North Sumatra, Indonesia. This field was first explored and started producing in 1970. The decline in production has resulted implementation of an infill drilling strategy in the Middle block of the reservoir to boost the production rate and increase the hydrocarbon recovery. However, the drilling success rate in the Middle block is relatively low compared to the already exploited West block. Four out of nine wells drilled in this block experienced instability issues during drilling including stuck pipe and loss circulation incidents. These problems not only cost the company a fortune, but also hinder the development program through low success rate.

The lack of knowledge on the accurate in-situ stress magnitudes and geomechanics characteristics of the reservoir formation and its overburden seal formation are the main reasons behind the instability and well integrity issues in the field. A detailed wellbore stability analysis with accurate input parameters for the original formation petrophysical and geomechanical properties, in-situ stress magnitudes and orientations prior to production will provide better guidance in designing wells in field "X" that will minimize the instability issues. In most of the drilling design and operations in this field, these key factors have not been taken into consideration in the well design and field development. The results of this research study is anticipated to be beneficial for providing a better understanding of the formation in-situ stress state and geomechanical characteristics and their evolvement over the lifecycle of the field that can be used to enhance the field development plan.

1.2 Overview of North Sumatra Basin

Field "X" is an oil and gas producer from a mature sandstone reservoir located in the northwest of the island of Sumatra, Indonesia, and a part of North Sumatra basin (Figure 1.1). North Sumatra basin is one of the thirteen basins in the Asia Pacific region with hydrocarbon reserves greater than 5 billion barrels of oil equivalent (BBOE). The discovered gas reserve of this basin is 25 trillion cubic feet (TCF) or 4.5 BBOE and 1.5 BBOE of oil and condensate (Meckel, 2012).

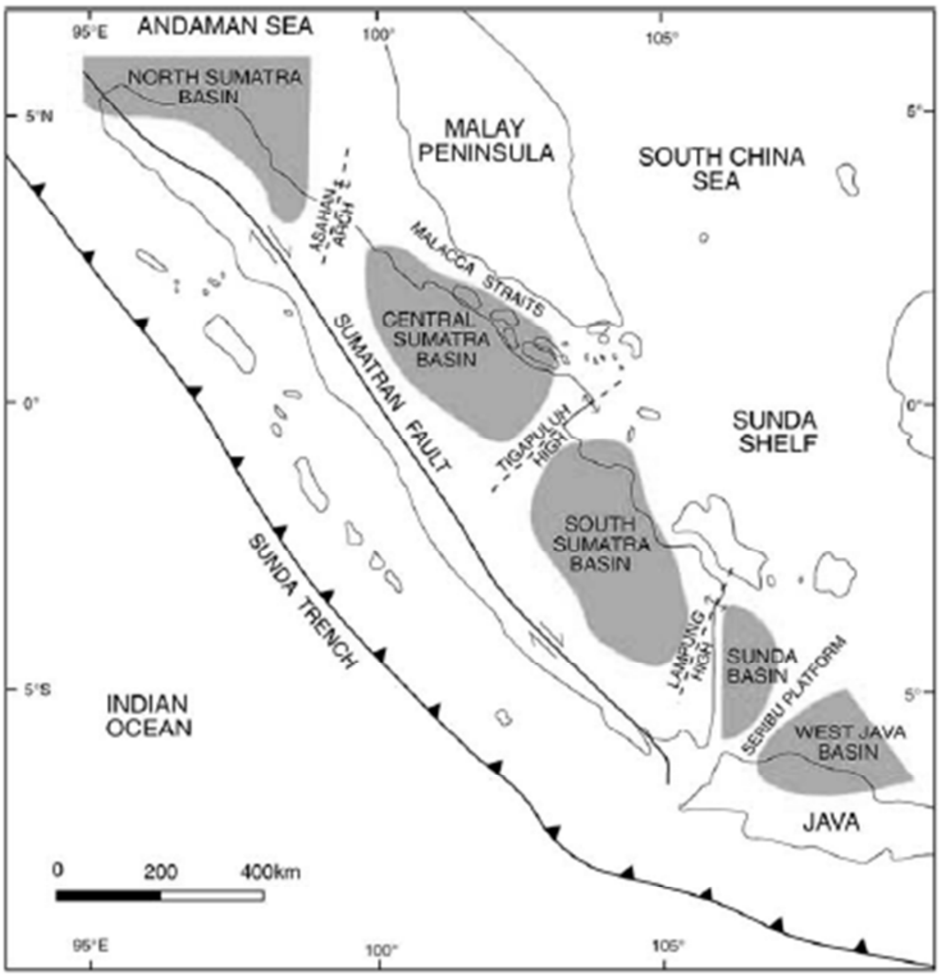

Figure 1.1 Petroleum basins in Sumatra (Barber et al., 2005).

The offshore portion of the field makes up around 75% of the basin. However, the early attempts to extend the exploration effort into the offshore section were deemed unsuccessful with relatively small discoveries. Because of the lack of remarkable exploration success to find significant new resources in Indonesia, oil and gas production has declined fast and highly depended on the production from mature fields.

1.3 Tectonic Background

The island of Sumatra is located at the westernmost of Indonesia’s archipelago with an area of 435,000 km^2 and oriented northwest-southeast (Barber et al. 2005). This island is part of Sunda microplate, a fragment that broke away from Eurasian plate through continental crustal splitting and rotating movement within the plate during the Palaeogene.

The margin of Eurasian plate is located at the southwest offshore corner area of Sumatra, where the Eurasian plate comes into contact with the north-northeastward of the Indian-Australian plate. Both plates are constantly active with the Indian-Australian plate downthrusts toward Eurasian plate in the oblique direction, creating a subduction zone. The subduction zone extends from the Himalayan front southward through Myanmar, Andaman Sea, Sumatra and south of Java. The prominent subduction system is the Great Sumatran Fault, a 1900 km-long strike-slip fault system that is running the entire length of the island. This fault accommodates the strike slip motion and oblique convergence of the two plates.

The Sumatra subduction zone affects the main geographical trendline of the island (Figure 1.2). Generally from southwest to northeast Sumatra can be described as: subducting oceanic plate, the forearc high, the offshore forearc basins, Sumatran fault, Barisan Mountains, and oil-bearing back arc basins (North, Central, and South Sumatra basin).

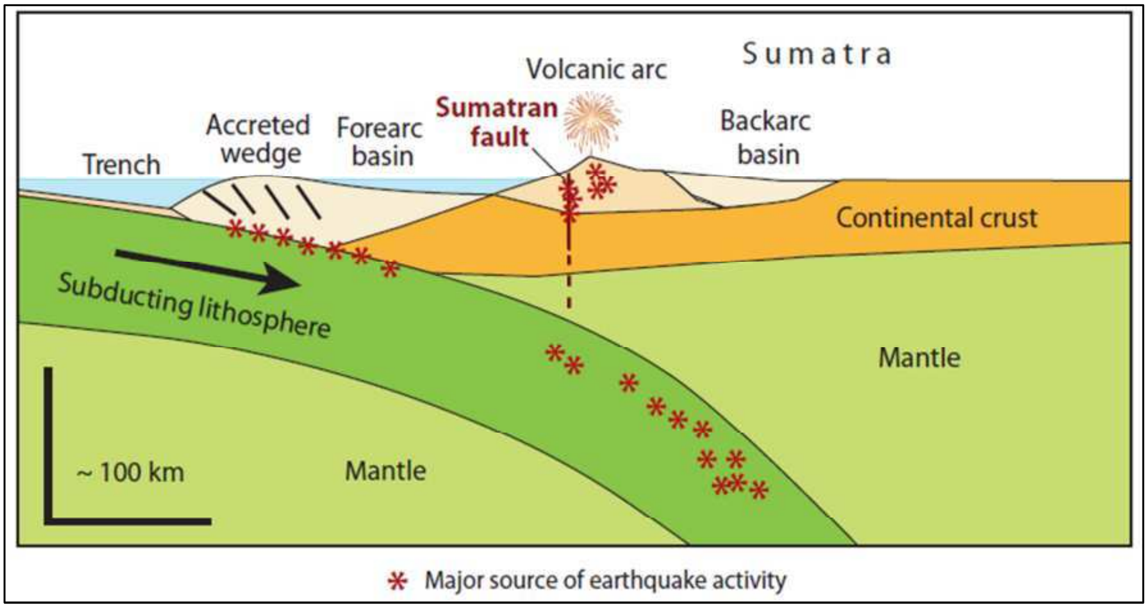

Figure 1.2 Schematic cross-section of Sumatra geology plate (Mcaffrey, 2008).

According to Davies (1984), the basin was formed in Eocene-Oligocene (Early Tertiary), consists of a series of sub-basins that were separated by basement highs. The regional stratigraphy system of North Sumatra presented by Rhiady et al. (1998) shown in Figure 1.3. The tectonic evolution can be described in the following paragraphs.

- Early Eocene to Early Oligocene Sumatra was aligned north-south, major Sumatran fault system was developed at this time. The sedimentation was characterized by undeformed clastic of Meucampli formation in the west which graded eastward into widespread shelf carbonates of Tampur formation.
- Late Oligocene to Early Miocene, rifting of continental crust in Malay and Thai basin affected the motion of Sunda microplate, causing counter-clockwise rotation and Sumatra moved away from Malay Peninsula. At this time, North Sumatra basin developed under a tensile stress regime, right lateral fault formed along the area. The faults configuration of the North Sumatra basin was north-south trending strike-slip, and northeast to southwest

normal faults. The sedimentation in this era consisted of deposition of basal conglomerates (Parapat formation) and graben fill in fluvial to paralic environment (Bruksah formation), while restricted thick marine shales (Bampo formation) also deposited elsewhere.

- Early Miocene to Middle Miocene, Sunda microplate rotation stopped, and Sumatra already aligned in northwest-southeast direction, with Indian-Australian plate subducted in acute angle. Breakup in Andaman Sea caused regional uplift in North Sumatra basin which reactivated the horst and graben structures. This led to widespread erosion and unconformities across the basin. The subsequent basin subsidence in early middle Miocene allowed rapid marine water invasion into North Sumatra basin. Thick inner neritic to bathyal shales (Peutu and Baong formation) were deposited.
- Late middle Miocene to recent, the second phase of Sunda microplate counter-clockwise rotation occurred, while Indian-Australian plate approached with increasing convergence angle. The result was inception of a compressive stress regime, which results the uplift of Barisan Mountains, frequent volcanic activity, and the spread of regressive sedimentation across North Sumatra basin. In this era, Baong formation and coarse clastic Keutapang formation were deposited.

The continued rotation of Sunda microplate exposed North Sumatra to two major compressive stresses:

a. Sumatran stress oriented N020^{o}E caused by convergence of the plates
b. Andaman stress oriented N170^{o}E and N160^{o}E caused by movements in Andaman Sea.

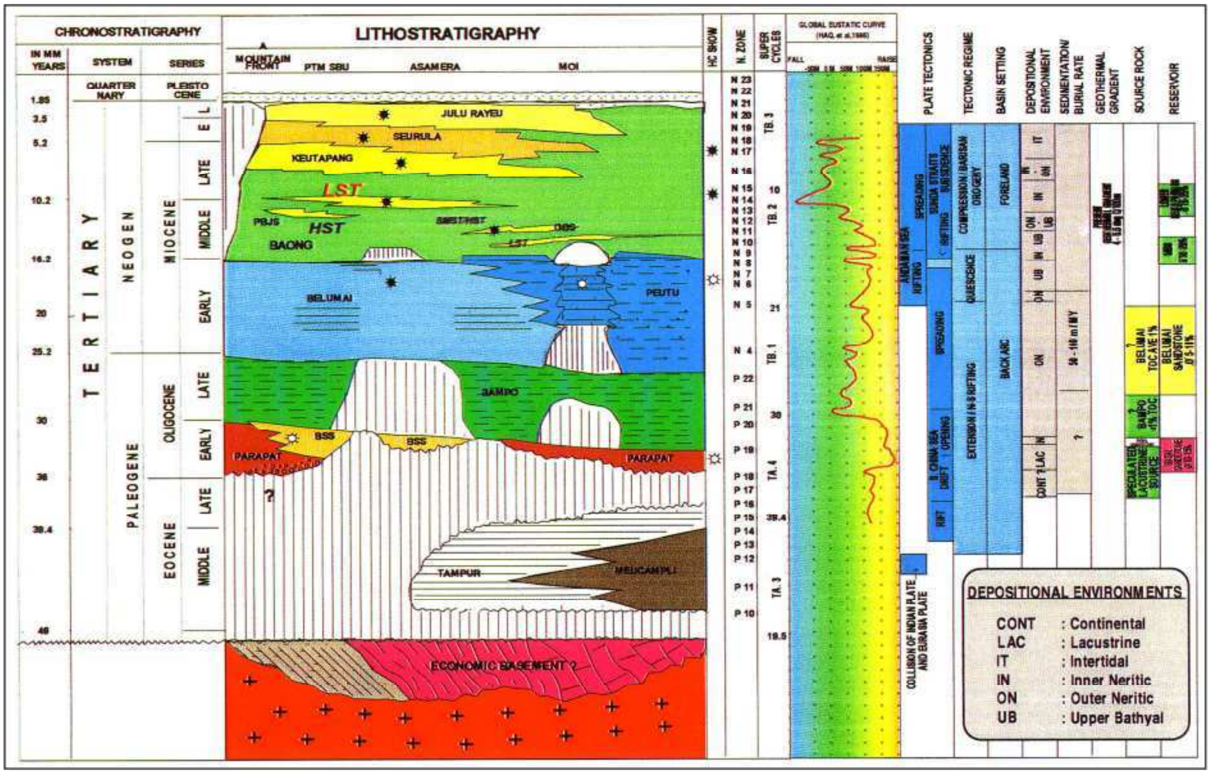

Figure 1.3 Regional stratigraphy system of North Sumatra Basin (Riadhy et al., 1998).

1.4 Middle Baong Sandstone

Baong formation can be categorized into three stratigraphy units: upper shale member, Middle Baong Sandstone (MBS) which is the producing reservoir in field "X", and lower shale member. The sediment of the MBS unit was deposited in deep marine area. Due to Barisan Mountains uplifting on the southwestern part of the basin, the sediments on the edge of the basin became unstable and slid down along the slope to the center of the basin, and finally stopped at the upper slope. On its way, the rock mass was sliding and turning into turbulent mass flow and finally deposited as the seafloor turbidite. This depositional process affects the shape of the formation, the gross thickness of the sandstone is decreasing from southwest to the northeast, north, east, and southeast, and the grain size is changing into clay size.

1.5 Field “X” Development

Field “X” is divided into three blocks: East, Middle, and West. These blocks are separated by normal and reverse faults. West and Middle blocks are known to be gas and oil producers, while no hydrocarbon has been produced from the East block so far. Currently, 54 wells have been drilled in this field.

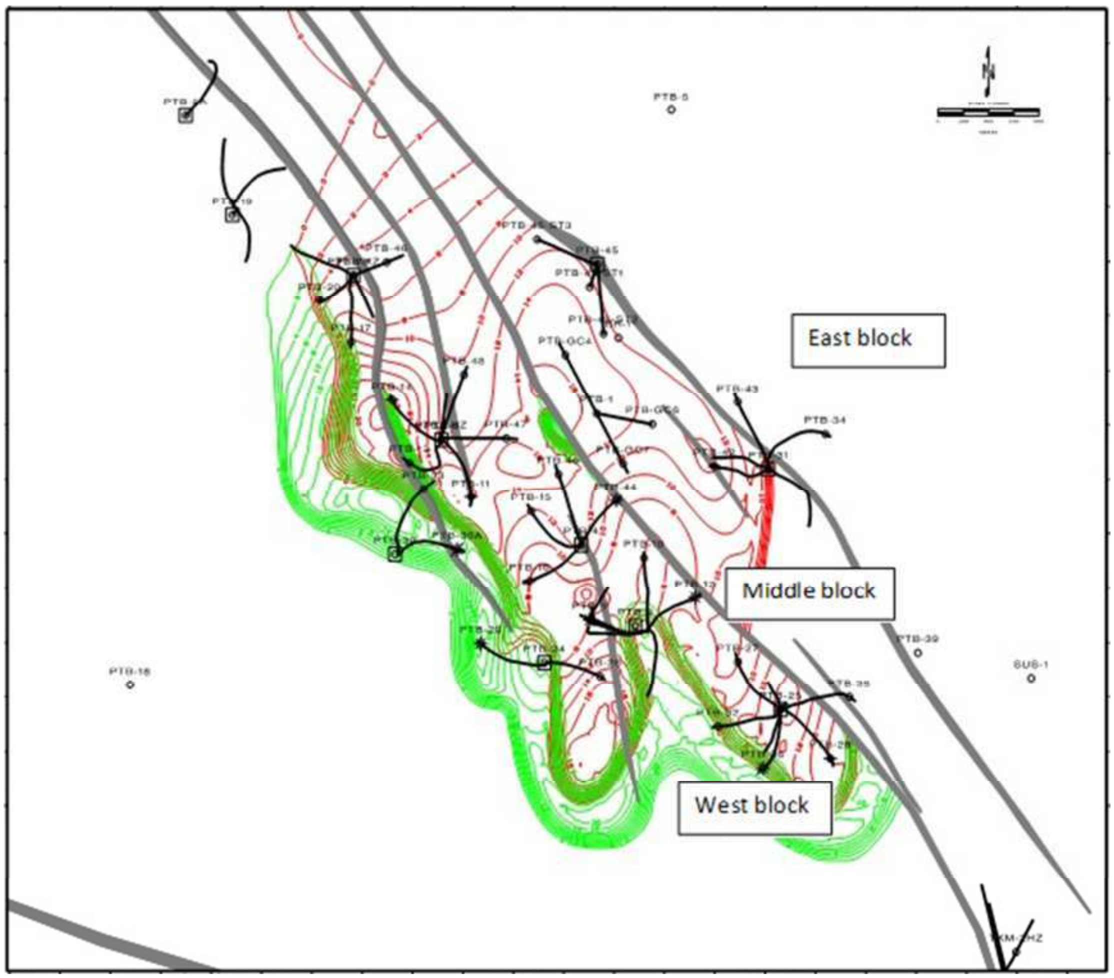

Figure 1.4 Iso netpay map with well trajectory.

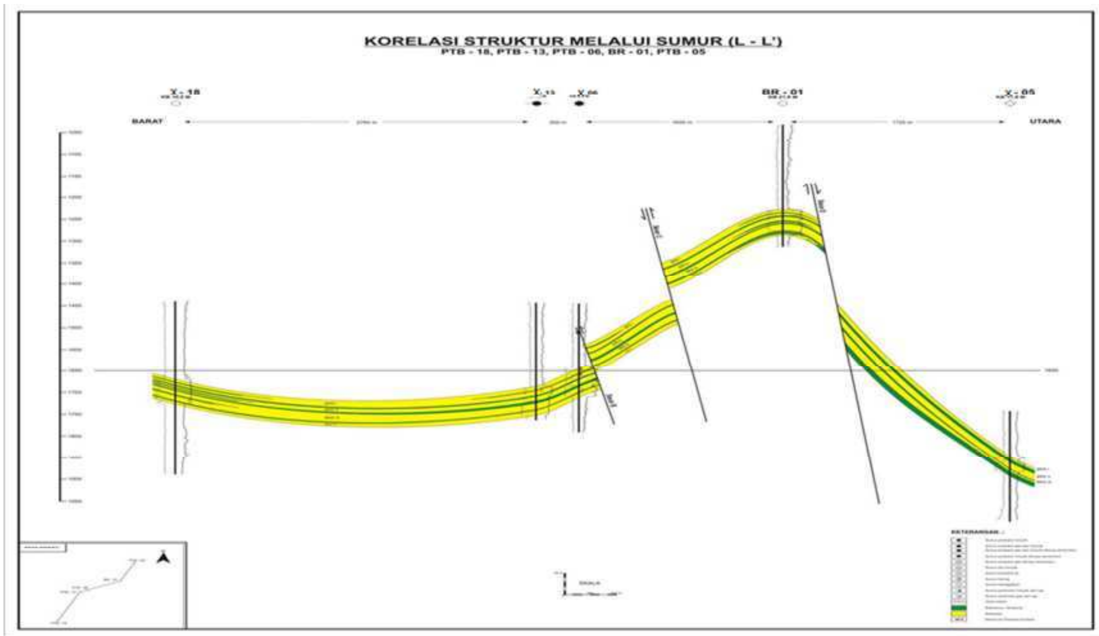

Figure 1.5 Blocks are separated by normal and reverse fault.

The surface area of field “X” is surrounded by swamps where the water level is changing because of low and high tide. This condition presents challenges to the logistics and drilling activity which also affects the field development plan. With limited space for drilling activity, wells have to be drilled through cluster systems with many of them are drilled in the directional or horizontal direction. Among 54 wells in this field, 37 of them are directional wells, five horizontal wells, and twelve vertical well.

Since the MBS sandstone distribution started from the southwest of this field, the west block became the main focus of the field development, where the sand formation is thicker and fewer shale breaks. There are 41 wells that have been drilled to date in this block, this number is relatively high compared to only nine wells in the Middle block and four wells in the East block.

1.6 Objectives

The main objective of this research study is to determine the causes of instability problems that occurred in field "X" by using an integrated wellbore stability analysis. Other objectives of this study include:

1. Developing one dimensional Mechanical Earth Model (1D MEM).
2. Determining the suitable correlations for geomechanics characterization in this field.
3. Building a wellbore-stability model incorporating the effects of geomechanics properties and in-situ stresses.
4. Determining the optimum drilling fluid density for any given azimuth and trajectory.

By carrying out this study we hope to have a better understanding in geomechanical characteristic of this field, which can be utilized for future developments in the field as well as improving the production.

1.7 Available Data

Data availability is the main challenge in characterizing the geomechanic properties in this field. Geomechanics was not considered as an important part of reservoir characterization in the past in this field. Therefore, there is minimum data or study related to geomechanical properties for this field. New core samples for laboratory measurements are also unavailable at the time of this study. This research is aimed to achieve the objectives by maximizing the utilization of available data by choosing suitable methods for calculations. The available data are listed as follows:

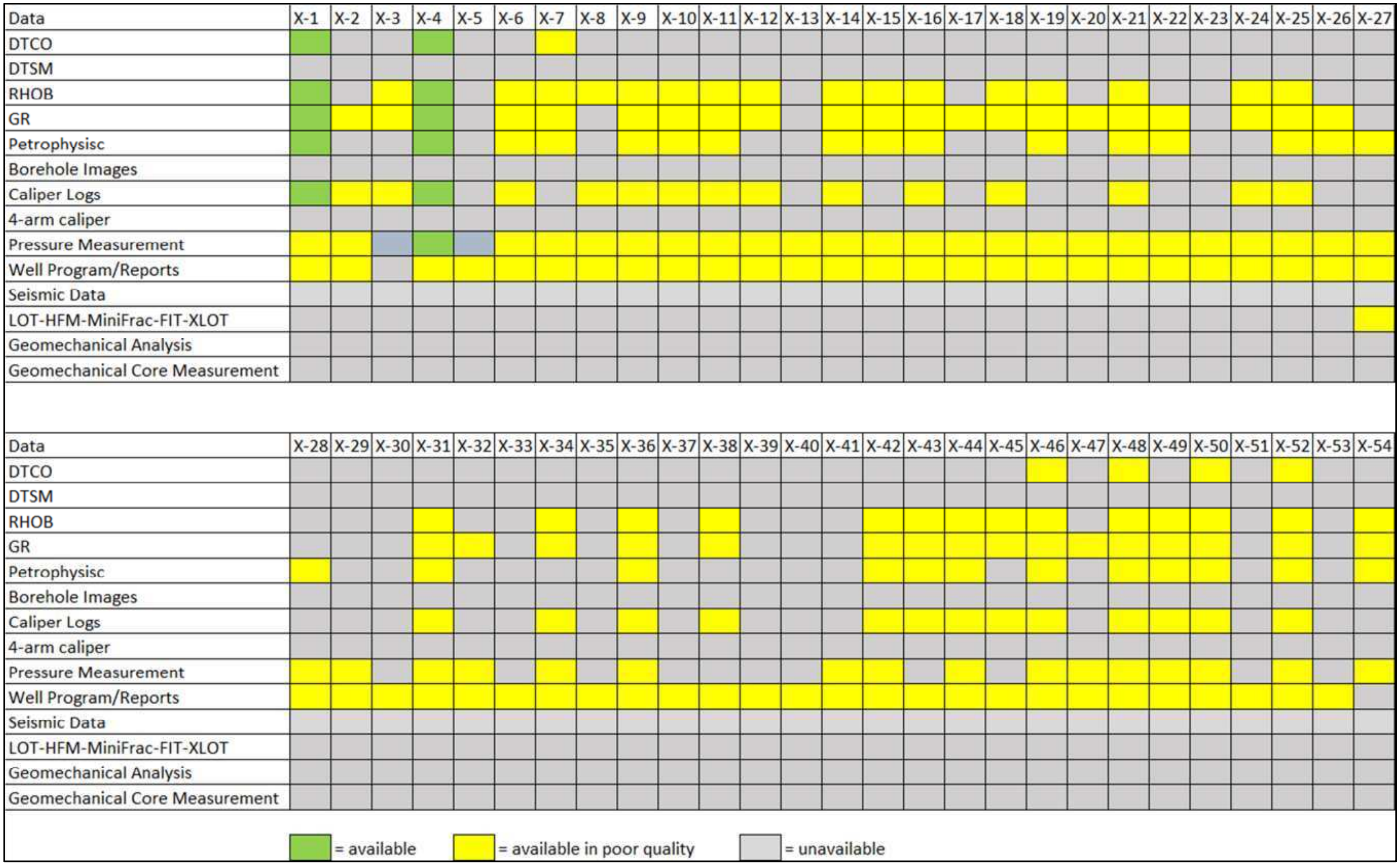

Figure 1.6 Available Data

1.7.1 Well Logging Data

Wireline logs are the key source of geomechanical characterization in this research study. The log data are used to determine the petrophysical properties, the in-situ stress state, rock elastic, and rock mechanical and formation strength properties. Combined with the drilling data, wireline logs were used to specify the problematic horizon. For this field, the well logs needed for this research are only available only for several wells and most of them are collected only in the sandstone reservoir formation. In addition, hydraulic fracturing data has been utilized to calibrate the minimum horizontal stress that was calculated using well log data.

1.7.2 Daily Drilling Reports

Daily drilling reports contains compiled data of instability instances that will be useful to identify the reason for the rock failure. From this reports, drilling progress chart has been created showing many challenges that caused non-productive time (NPT) during drilling. This data is useful to determine the main cause of wellbore instabilities.

1.7.3 Mud Logging Reports

This mud logging reports supply the examination results of the rocks cuttings that were circulated to the surface. From this report we can determine the lithology with respect to depth and indicate the presence of hydrocarbon. These logs are also useful for well safety monitoring, to quickly recognize the overpressure zones, lost circulation, and gas kicks.

1.7.4 Pore Pressure Measurements

Pressure measurements in this field are available for the producing sandstone reservoir only. This data has been used to calibrate the log-derived pore pressure.

1.8 Workflow

The research was conducted with the following workflow:

1. Evaluating the available methods to determine the geomechanics properties and in-situ stress state, and choosing the methods that suitable for the available data.
2. Constructing the 1D Mechanical Earth Model using Techlog well log interpretation software.
3. Determine the best correlations that are suitable for the field based on wellbore stability model.
4. Modeling the wellbore stability with sensitivity analysis using Matlab software.
5. Determining the mud weight required for drilling in various azimuth and inclination.

CHAPTER 2

PROBLEM DIAGNOSTIC

The effort to develop the Middle block in field "X" has been quite challenging because of the unusual rate of well failures during the drilling phase. Out of the nine wells that were drilled in this block, four had experienced severe wellbore stability issues, failed to reach the target depth, and eventually were abandoned. This number is relatively high compared to the West block, where only one out of 41 wells failed to reach the target because of mechanical issues encountered. A problem diagnostic has been conducted to determine the main cause of the instability issues in this field.

2.1 Problem Diagnostic Methodology

To identify the causes of instability problems encountered in this field, a problem diagnostic procedure was performed, which includes studying the well plans, drilling programs, daily drilling reports, and various logs for all well. Wellbore stability issues can be caused by combination of many factors, which can be classified into controllable and uncontrollable in origin. Pasic et al. (2007) listed these factors as shown in Table 2.1.

To narrow down the possible key factors that cause the wellbore instabilities in field "X", a comparative study was conducted among three wells with and without severe instability issues. These three wells are located in adjacent to each other and drilled from the same cluster group at the surface. Since the three wells are drilled in relatively identical subsurface condition, we can assume that the uncontrollable (natural) factors affect all wells in similar magnitude, including the well without severe wellbore instability issues, and therefore, these factors can be eliminated from possible key causes of instabilities.

Table 2.1 Causes of wellbore instabilities

Causes of Wellbore Instability	
Uncontrollable (Natural) Factors	**Controllable Factors**
Naturally Fractured or Faulted Formations	Bottom Hole Pressure (Mud Density)
Tectonically Stressed Formations	Well Inclination and Azimuth
High In-situ Stresses	Transient Pore Pressures
Mobile Formations Physico/chemical	Rock-Fluid Interaction
Unconsolidated Formations	Drill String Vibrations
Naturally Over-Pressured	Shale Collapse Erosion
Induced Over-Pressured	Shale Collapse Temperature

The key operational data that will be analyzed for this problem diagnosis are the non-productive time at a horizon or lithology, measured depth (MD), true vertical depth (TVD), mud weight, borehole inclination, azimuth, and lithology.

2.2 Case Study for Well X-51

Well X-51 was proposed as development well with expected production of 2 MMSCFD gas and 30 BCFD of condensate from Besitang River Sand (BRS) formation (structure and wells correlations are shown in Figure 2.1 and 2.2). The well was planned to be drilled directionally with azimuth N 330^o and inclination 42.9^o, as illustrated in well diagram in Figure 2.3. The kick off point starts at 730 m, with final depth at 1814.7 m MD (meter measured depth) or 1600 m TVD (meter true vertical depth). According to the plan, the drilling process would have taken 23 days to complete.

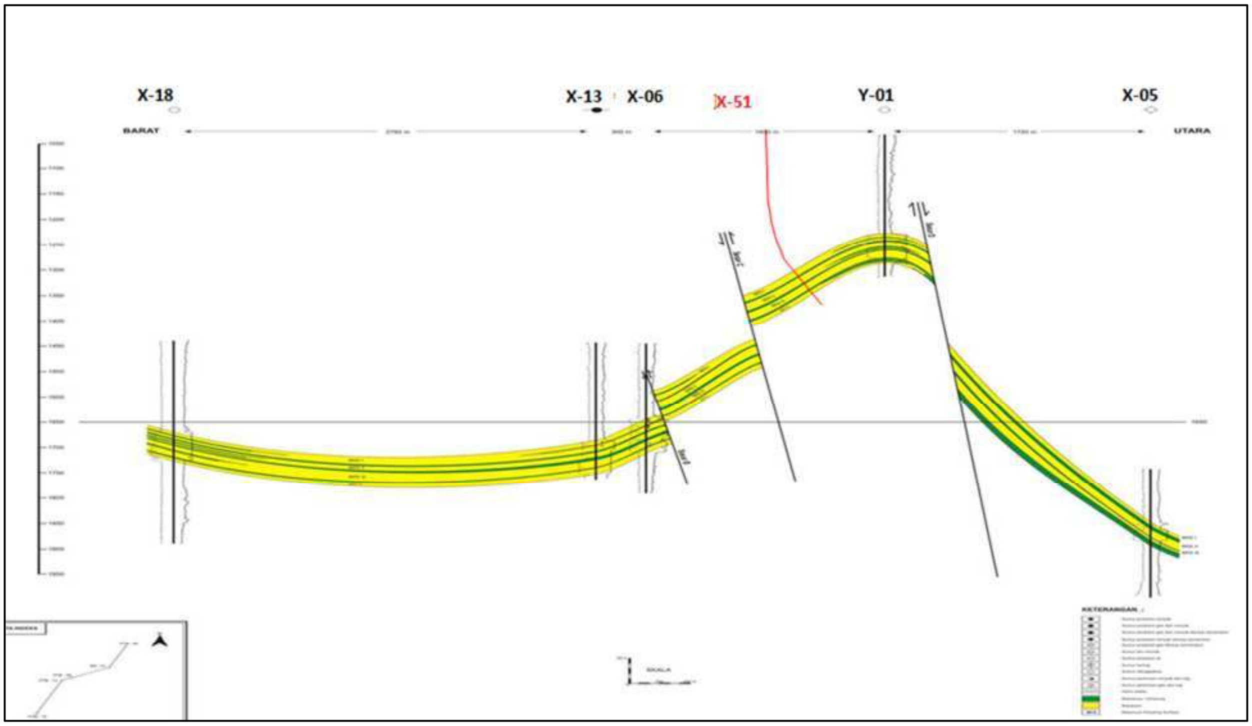

Figure 2.1 Structure correlations for BRS formation.

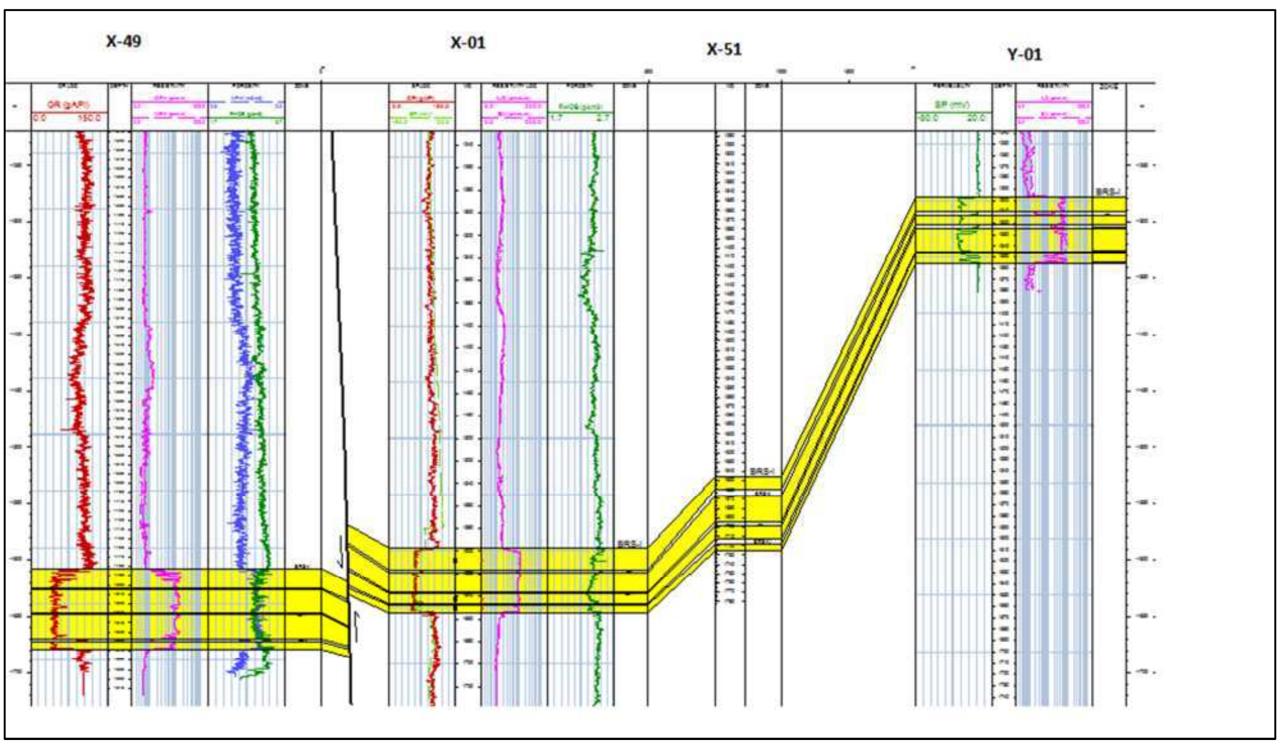

Figure 2.2 Wells correlation for BRS formation.

To reach the target depth at BRS sandstone formation, the drilling process will pass through Seurula formation, thin Keutapang formation, and the upper Baong shale formation. Seurula formation consists mostly of sandstone, shale and clay, while Keutapang formation composed mainly of fine grained sandstone, interbedded with clay, shale, and limestone streaks.

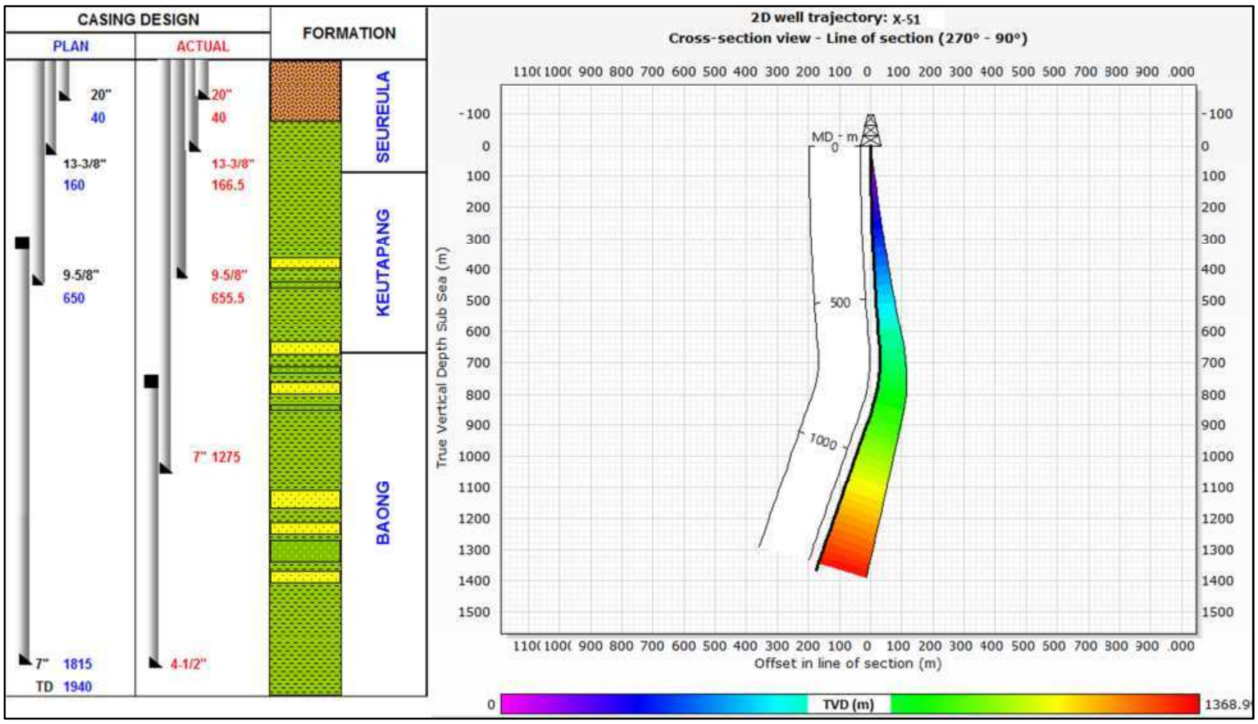

Figure 2.3 Wellbore diagram and actual wellbore trajectory X-51.

2.2.1 Eight and Half Inch Section

The actual kick off point for directional drilling is at 724 m MD, with the target depth at 1054 m MD. The mud weight used in this section is 1.2 gr/cm^3 (SG). Severe wellbore-stability issues were experienced while drilling this section that led to Bottomhole Assembly (BHA) stuck at 1040 m MD due to pack-off. Several types of efforts were done to overcome this problem including optimizing the mud circulation, jarring, and utilizing the dissolving chemicals. All of these efforts were unable to free the stuck pipe and the hole was plugged. The key operational parameter for this section is presented in Table 2.2. A new sidetrack well program was then prepared for this well with increased mud weight from 1.2 to 1.24 SG.

2.2.2 Eight and Half Inch Section (first sidetrack)

The sidetrack window was drilled at 891 m MD using 1.24 SG mud weight, first indication of wellbore instabilities occurred at 1172 m MD, shale cuttings were observed at shale shakers and BHA got stuck. Optimization of mud circulation successfully freed the stuck BHA. However, while running the BHA back into the current depth, the BHA sat at 978 m MD. The drilling fluid from the wash down operation indicated that the hole was filled with shale cutting.

Another pack off and overpull occurred at 1495 m MD, the mud weight was increased to 1.3 with higher viscosity and successfully free the stuck BHA. Unfortunately the next pack off and overpull at 1478 m MD cannot be surmounted, the BHA was cut with top of fish (TOF) at 1418 m MD, and the hole was plugged with top of cement (TOC) at 1305 m MD. The amount of shale cuttings from drilling fluid circulation indicated that they were the causes of pack off in both occurrences.

2.2.3 Eight and Half Inch Section (second sidetrack)

The second sidetrack window was drilled at 1305 m MD and immediately experienced overpull at 1359 m MD. Jarring, optimized circulation, wash down and reaming failed to release the stuck BHA. The well was plugged back and abandoned.

2.2.4 Drilling Progress Chart

The drilling progress for X-51 showed the time that was spent for specific depth. The depth of the unstable area can be easily recognized immediately based on the amount of non-productive time spent at this depth.

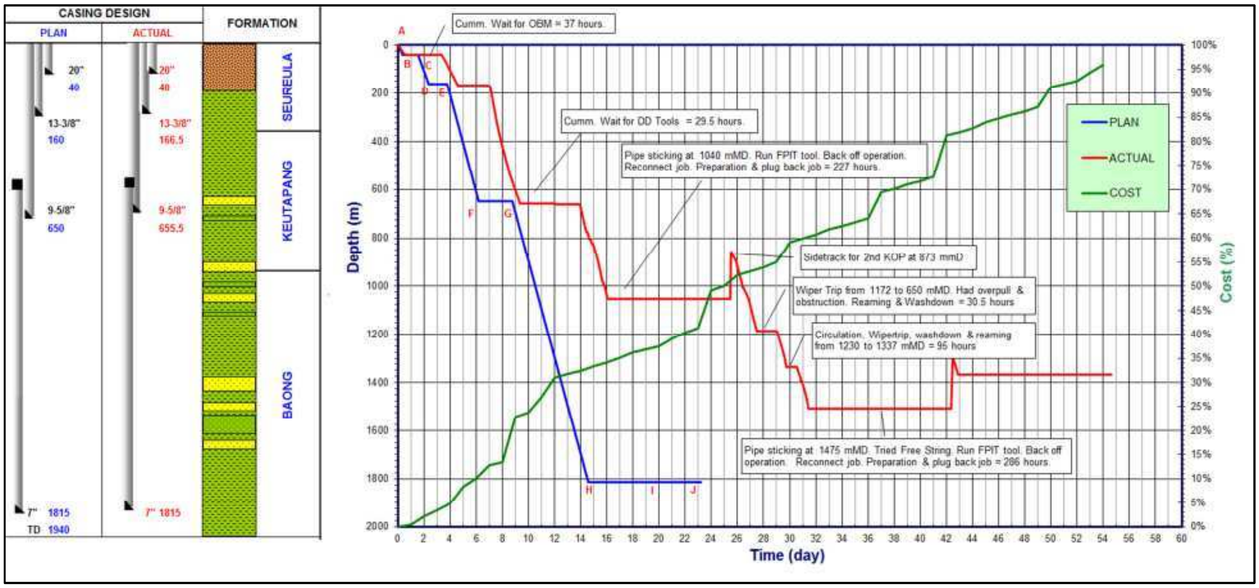

Figure 2.4 Drilling progress chart well X-51.

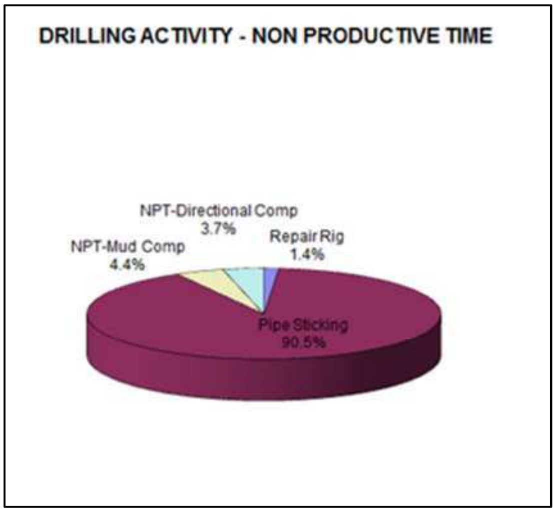

Figure 2.5 Non-productive time chart for well X-51.

It is evident from the non-productive time chart that 90.5% of the non-productive time was caused by the stuck pipe incident. This percentage is very high compared to other causes of non-productive time for this well.

2.2.5 Mud Log Data

Mud log data, as shown in Figure 2.6, were used to show the lithology, mud properties, and cutting description at the problematic depths, which were derived from daily drilling reports and drilling progress chart. The key operational parameters at the investigated depths were listed in Table 2.2.

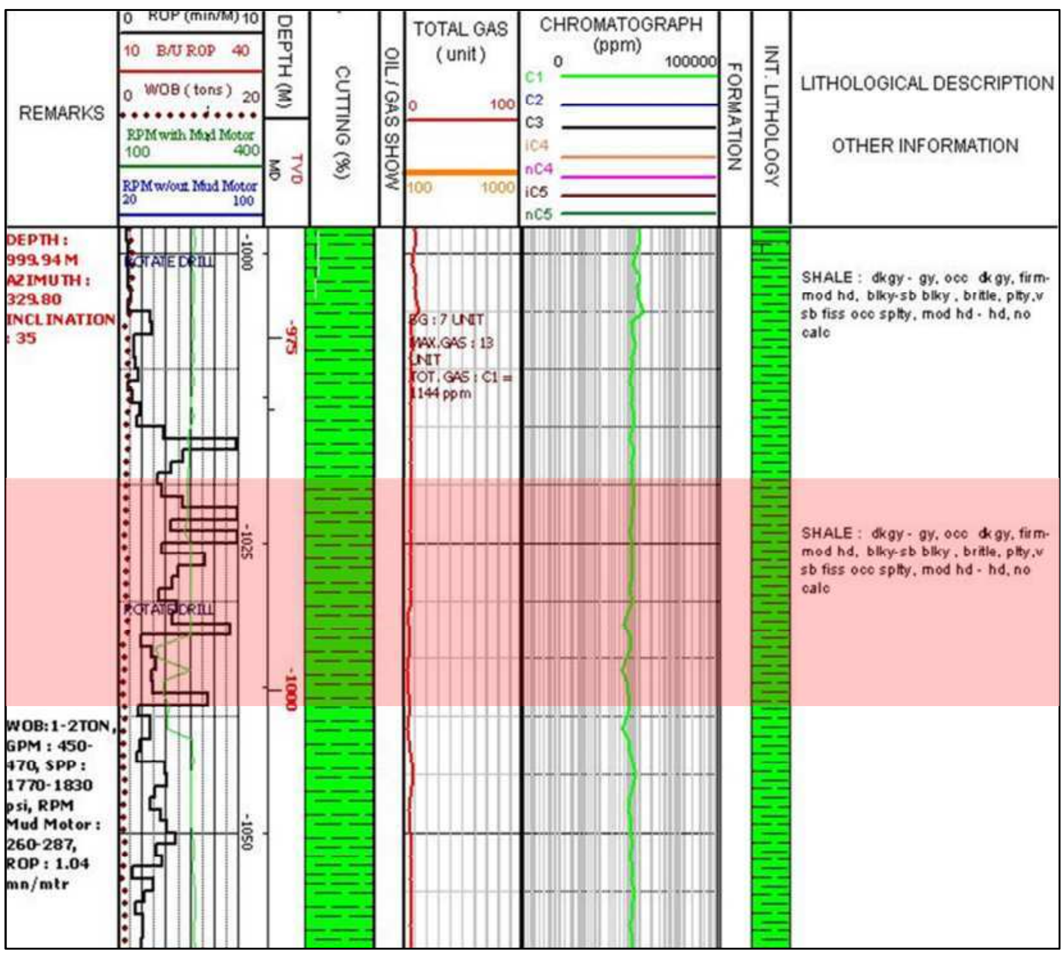

Figure 2.6 Mud log data for eight and half inch section.

Table 2.2 Key operational parameters used for drilling in well X-51

No.	Section	MD m	TVD m	Lithology	Azimuth degree	Inclination degree	Mud Weight gr/cm^3	Mud Viscosity	Mud Type
1	Eight and half inch section	1040	999	Shale	329.8	35	1.24	90	Oil based mud
2	Eight and half inch section (first sidetrack)	1172	1106	Shale	327.9	33	1.25	88	Oil based mud
3	Eight and half inch section (first sidetrack)	1495	1381	Shale	331	32.1	1.27	95	Oil based mud
4	Eight and half inch section (first sidetrack)	1478	1359	Shale	331	32.1	1.27	95	Oil based mud
5	Eight and half inch section (second sidetrack)	1359	1260	Shale	325.5	32.3	1.26	90	Oil based mud

2.3 Case Study for Well X-53

Well X-53 was planned to be a development well that was drilled from the same cluster group as well X-51. Like well X-51, the target reservoir for this well is also Besitang River Sand formation. To reach this formation, the drilling process will pass through Seurula formation, thin Keutapang formation, and the upper Baong shale formation. The initial plan for the well is directional with azimuth N 133.7^o and inclination 35.6^o. The kick off point starts at 600 m, with final depth at 1825 m MD/ 1640 m TVD. According to the plan, the drilling process would have taken 24 days to complete. The wellbore diagram is shown in Figure 2.7.

2.3.1 Eight and Half Inch Section

The actual directional section starts from the kick off point at 580 m MD and reach 1690 m MD. The designed mud weight for this section was 1.2-1.3 SG and viscosity 45-50 cp, this mud weight is higher than what was used in well X-51 to avoid similar problems. However, wellbore instabilities still occurred in this section. The first problem happened while pulling out the BHA, there was indication of pack off which lead to stuck BHA at 1565 m MD with an overpull of 60 ton. Jarring and optimized circulation were failed to release the BHA, and finally it was decided to cut the BHA using severing tool at 1545 m MD. The wellbore was then plugged, and a new drilling program for a sidetrack well was prepared.

2.3.2 Eight and Half Inch Section (first sidetrack)

The new program for this well started with creating a sidetrack window at 1035 m MD. A number of well instability issues occurred during drilling this section. The first problem happened while running down the BHA for sidetrack, the string sat at 1054 m and experienced pack off which led to stuck BHA. Large amount of shale cuttings were found at the shale shaker. Eventually, jarring successfully freed the BHA, and then the mud weight was increased from 1.56 to 1.58 SG. Another try running down the BHA for sidetrack experienced pack off and stuck. After being released by jarring, the mud weight was increased from 1.59 to 1.61 SG.

The next attempt to create the planned sidetrack well was hampered after a deviation from the designed trajectory was detected. This deviation was predicted to be caused by the reaming and wash down from releasing the stuck BHA. A new program with new trajectory was created.

The new drilling program running well without severe instability issues throughout the Baong upper shale formation. However, total loss occurred at 1782 m MD followed by stuck BHA. The mud weight during total loss was 1.68 SG. The efforts to release BHA eventually failed, and the string was cut at 1310 m.

2.3.3 Eight and Half Inch Section (second sidetrack)

The attempts to create a new sidetrack well keep failing during BHA trip, the string sat at 1042 m and was not placed into the new sidetrack borehole. There were also indications of pack off at 1020 m. The well was then plugged back at 950-1050 m MD and left as suspended well.

2.3.4 Drilling Progress Chart

The drilling progress chart in Figure 2.8 shows the time that was spent for specific depth. From this chart the depth of the unstable area can be recognized immediately based on the amount of non-productive time spent at a depth. Unlike well X-51, there are two types of formation where the instabilities occurred, the upper shale Baong formation and BRS sand formation.

Similar to well X-51, the non-productive time chart (Figure 2.9) shows that most of the non-productive time was caused by pipe sticking. The next bigger cause of non-productive time in this well is reaming during drilling the first sidetrack well.

2.3.5 Mud Log Data

Mud log data in Figure 2.10 and 2.11 were used to determine key operational parameters at the investigated depths. The lithology, mud properties, and cutting description at the problematic depths were observed and listed in Table 2.3. Other mud related data that was found is a warning letter from the Oil Company to the drilling fluids provider regarding the unmatched properties between the required specifications to the actual drilling fluids.

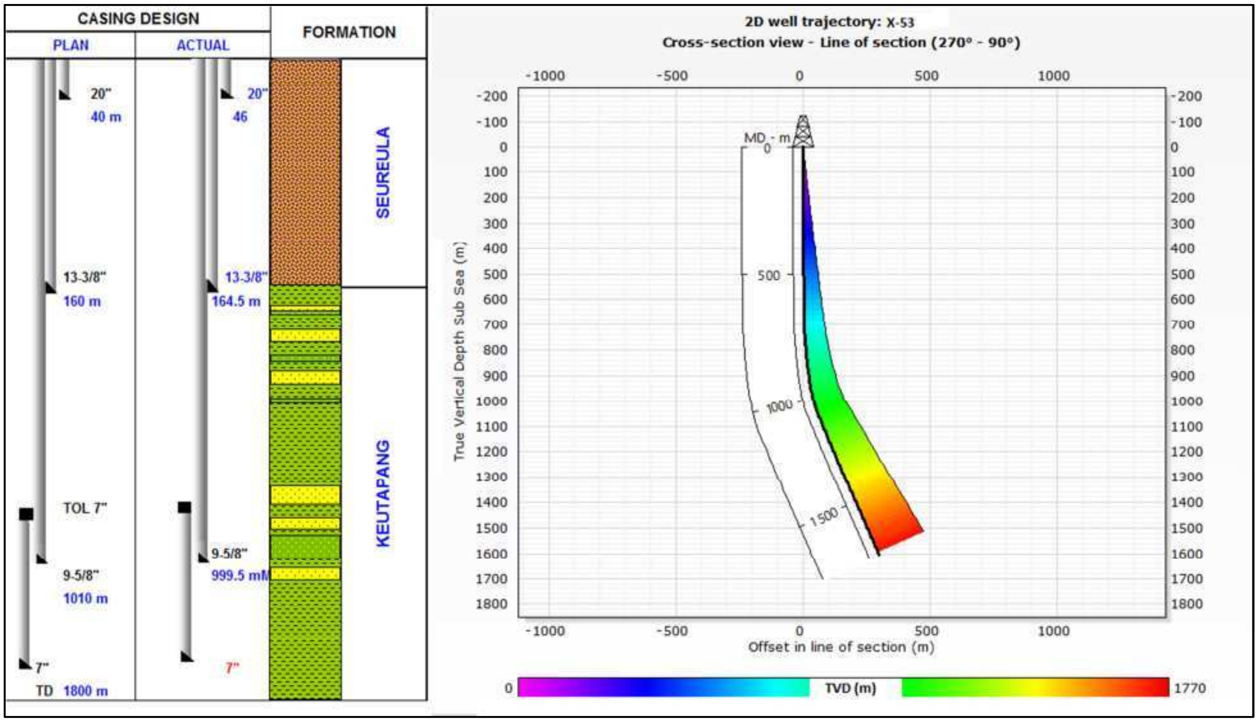

Figure 2.7 Wellbore diagram and actual wellbore trajectory X-53.

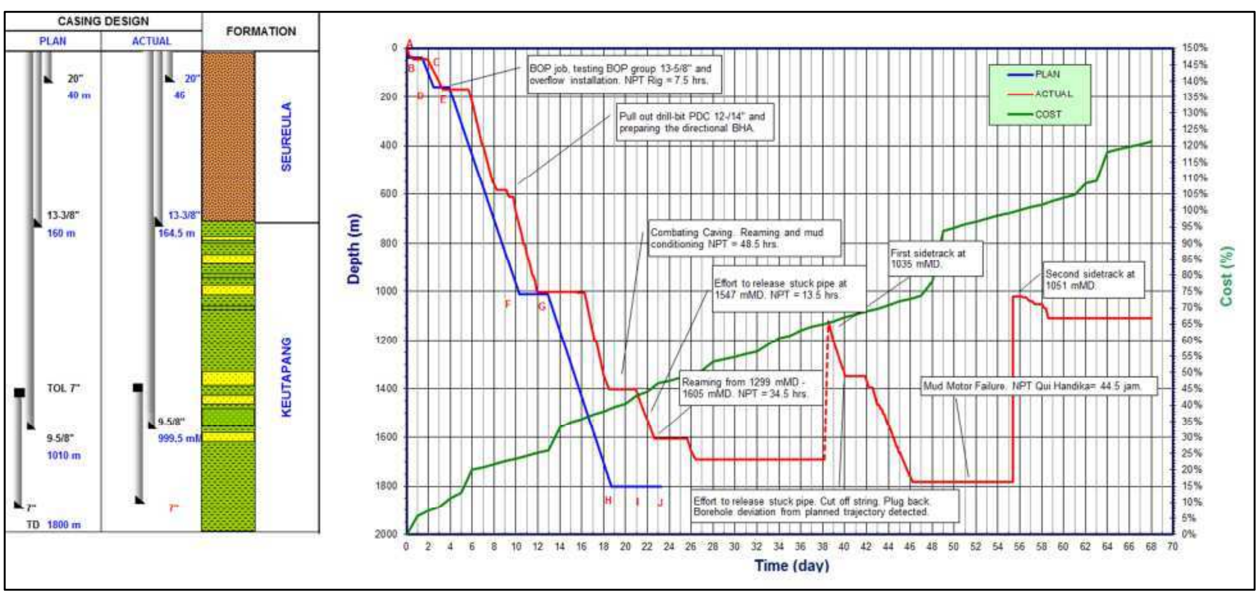

Figure 2.8 Drilling progress chart well X-53.

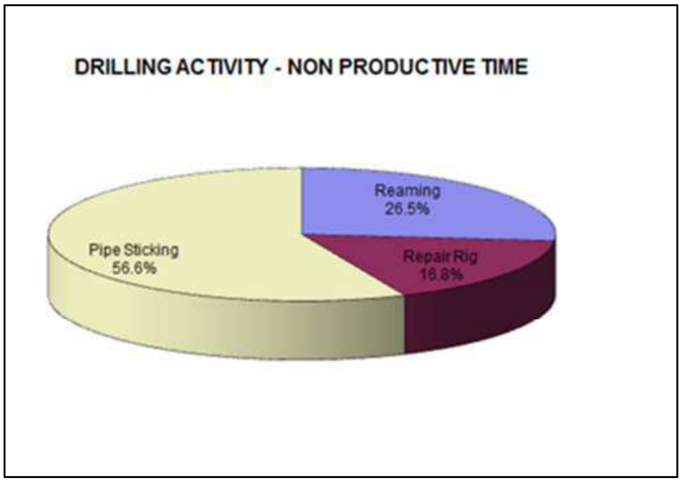

Figure 2.9 Non-productive time chart for well X-53.

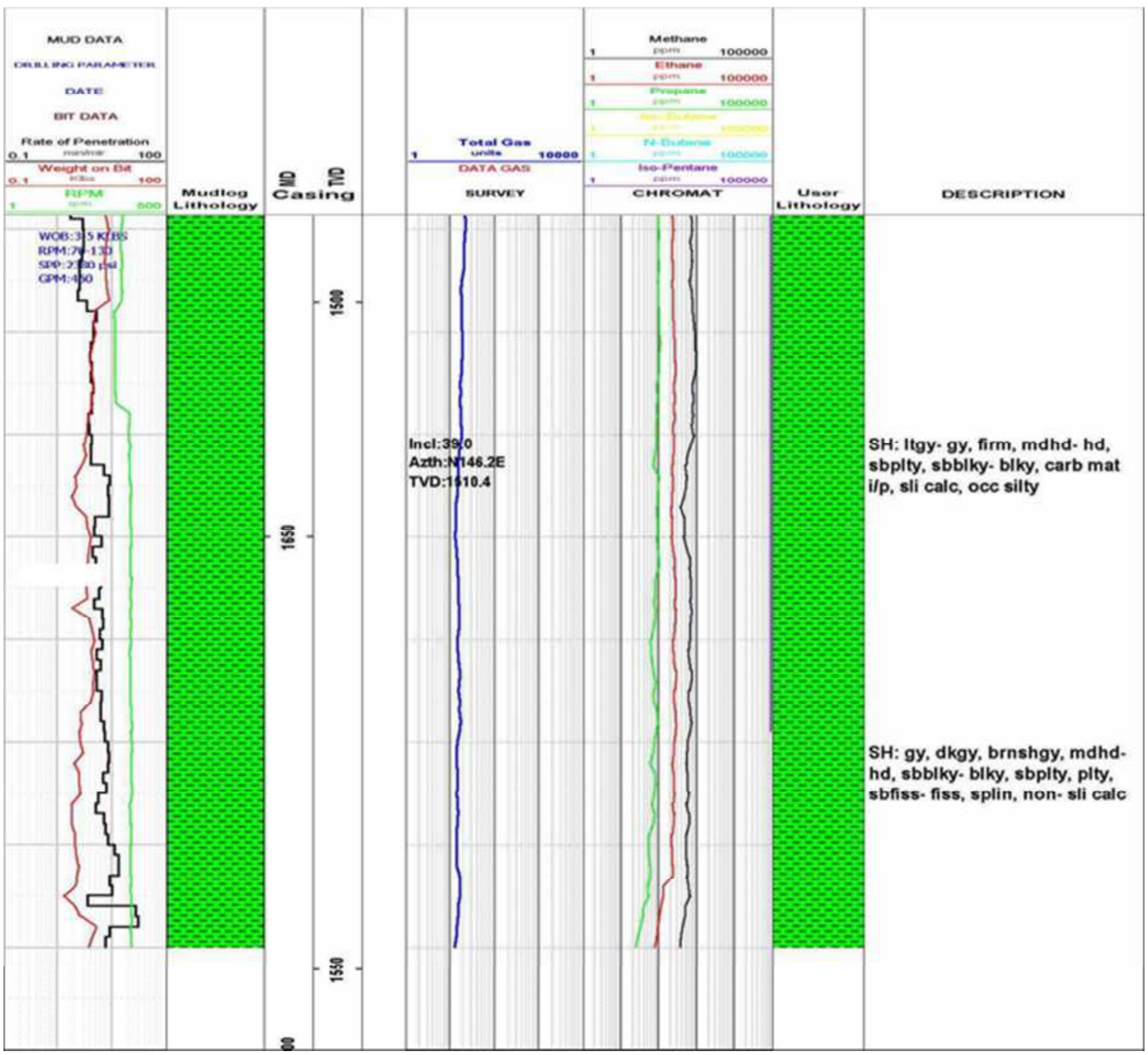

Figure 2.10 Mud log data for eight and half inch section at shale formation.

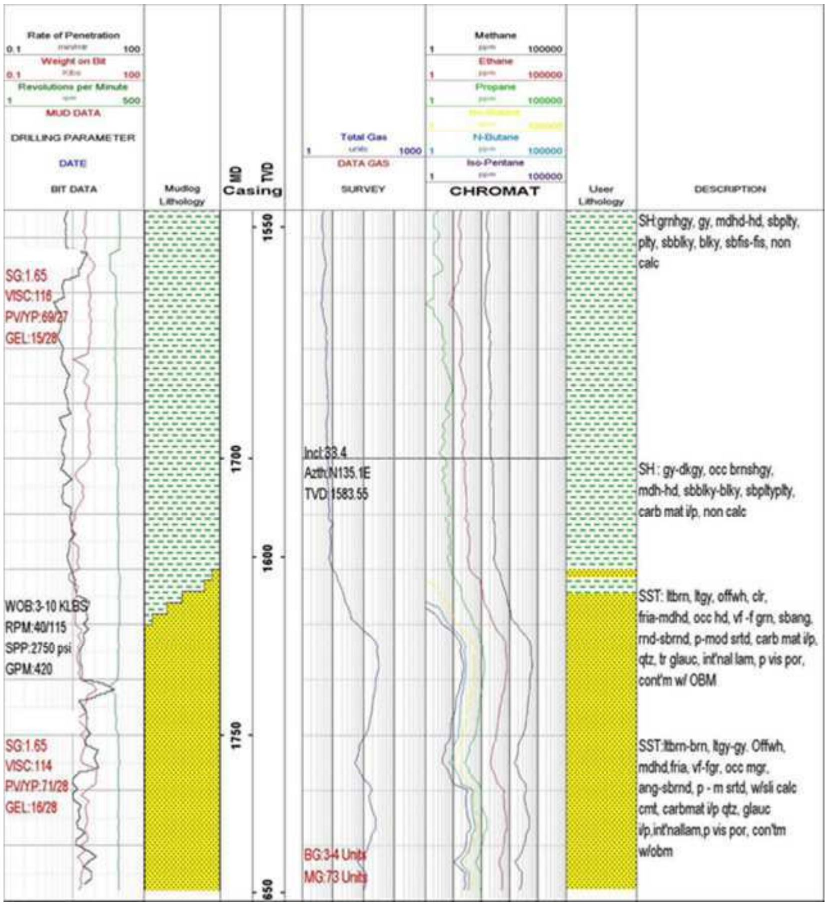

Figure 2.11 Mud log data for eight and half inch section at sand formation.

Table 2.3 Key operational parameters used for drilling well X-53

No.	Section	MD m	TVD m	Lithology	Azimuth degree	Inclination degree	Mud Weight gr/cm^3	Mud Viscosity	Mud Type
1	Eight and half inch section	1565	1472	Shale	134.1	34.2	1.65	120	Oil based mud
2	Eight and half inch section (first sidetrack)	1782	1640	Sandstone	135.1	33.4	1.65	114	Oil based mud

2.4 Case Study for Well X-52

Well X-52 is a development well drilled from the same cluster group as well X-51 and X-53. Unlike the other two, well X-52 reach the drilling of well X-52 successfully reach the target depth, although with some wellbore instability issues during drilling. The well was drilled directional with inclination 32^o and azimuth N 98.3^o. The wellbore diagram is shown in Figure 2.12.

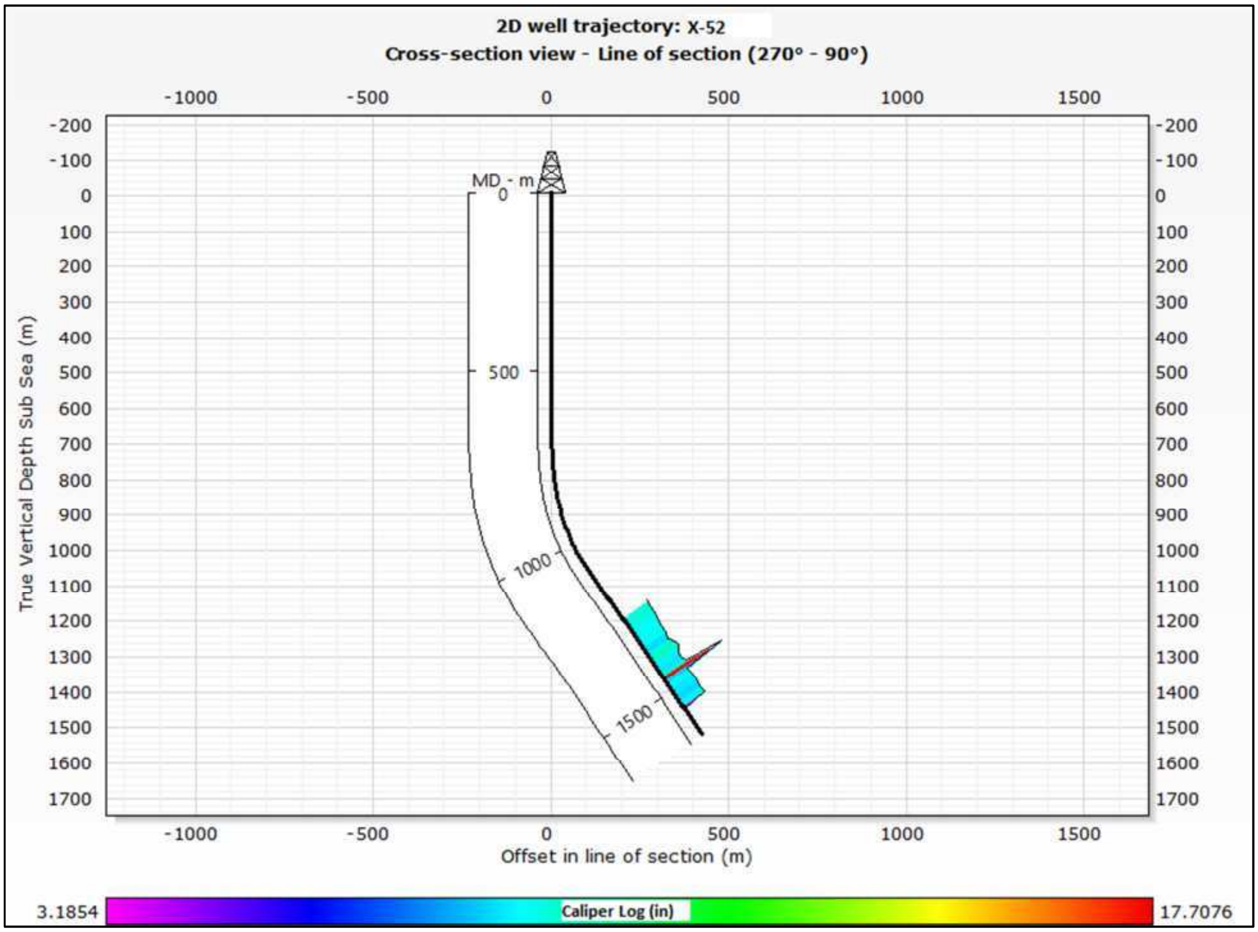

Figure 2.12 Diagram for well X-52.

The first wellbore instability problem occurred at 1478 m MD (shale formation) with mud weight 1.27 SG. After successfully releasing the BHA, the drilling of this section was done by using mud weight 1.28 SG until it reach the sandstone formation (target reservoir). Another pack off happened at 1650 m MD at shale formation (below the target reservoir). Pack off detected followed by stuck BHA. The mud weight used at this section was 1.29 SG.

2.4.1 Mud Log Data

The mud log in Figure 2.13 data shows the key drilling parameter at the problematic depth, which were listed in Table 2.4.

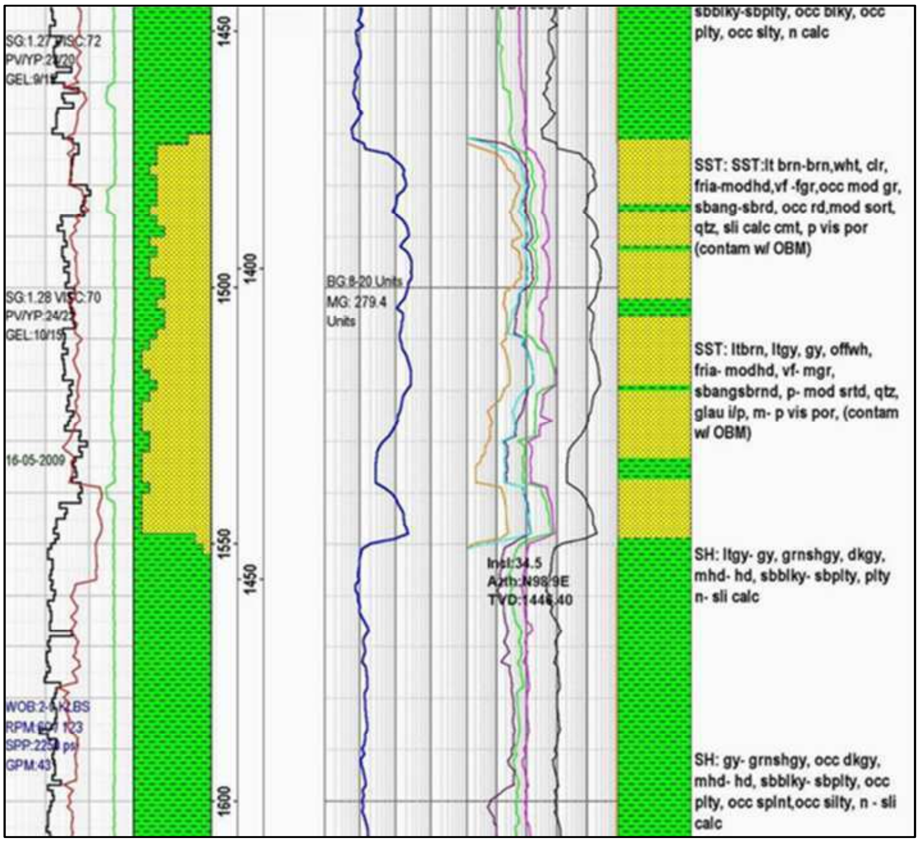

Figure 2.13 Mud log data for eight and half inch section well X-52.

Table 2.4 Key operational parameters used for drilling well X-52

No.	Section	MD m	TVD m	Lithology	Azimuth degree	Inclination degree	Mud Weight gr/cm^3	Mud Viscosity	Mud Type
1	Eight and half inch section	1478	1380	Shale	98.3	34.5	1.27	72	Oil based mud
2	Eight and half inch section	1650	1528	Shale	98.1	33.5	1.29	70	Oil based mud

2.4.2 Caliper Log

The Besitang River Sand formation is the target reservoir in this well, located right in the middle of Baong shale formation. The caliper log in Figure 2.14 shows indications of wash out above and below the reservoir using mud weight 1.27 - 1.29 SG. Compared to other wells, the mud weight that was used in this well is higher than well X-51, but a lot lower than the mud weight of well X-53. There was still indication of loss circulation in well X-52, however the degree of severity much lower than well X-53.

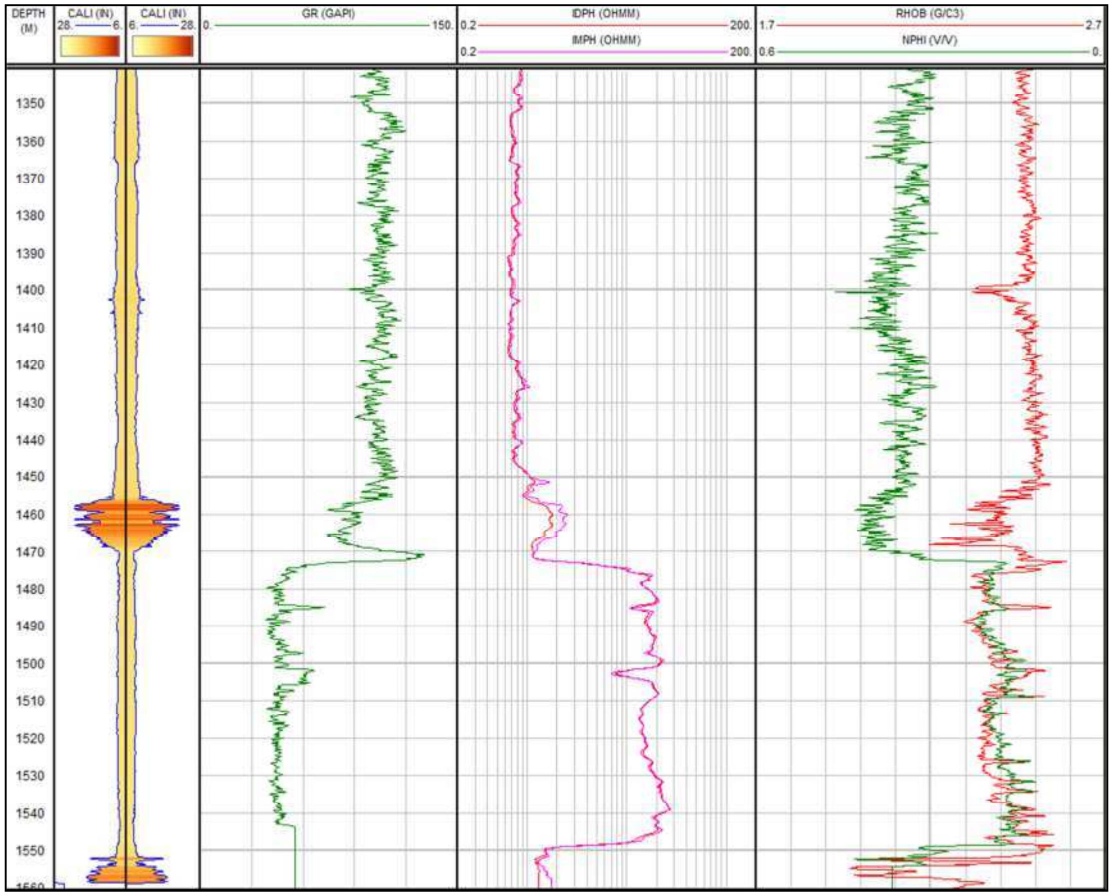

Figure 2.14 Caliper log of well X-52.

2.5 Field “X” Instability Problems

Based on the problem diagnostic of the case studies, there are several conclusions were reached.

1. Instability problems occurred in all three stratigraphic units of Middle Baong Sandstone: the upper shale, sandstone, and the lower shale.
2. The types of instability issues are different based on the lithology, wellbore breakouts happened in shale formation, and loss circulation happened in sandstone formation.
3. The drilling fluids properties for well X-53 cannot be used as reference due to the unmatched specification to the actual fluids.

4. All instability issues occurred at the inclined section of the well, therefore the effects of wellbore inclination needs to be analyzed.
5. Proper mud weight determination is the key factor for successful drilling in these wells.

CHAPTER 3

LITERATURE REVIEW

The subsurface formations are subjected to a stress field that is largely influenced by the overburden formation, topography, tectonic activities, rock material behavior, and geological history. Accurate knowledge of in-situ stress state in creating geomechanical model is important to prepare for the effects of subsurface conditions prior to the drilling. In this chapter, important parameters in understanding in-situ stress state in the subsurface formations and around the wellbore will be reviewed.

3.1 Stress

Stress is defined as force acting per unit area which pushes or pulls a body of a material. The magnitude of the force and the properties of the material determine the response of the material toward the applied stress. In general, the equation for stress is:

$$\sigma = \frac{Force}{Area} = \frac{F}{A} \tag{3.1}$$

In earth sciences, stress commonly measured in psi or megapascals (MPa). The area of the cross section and the direction of the force is important in defining the state of stress.

The force that is acting on the area can be divided into two components: F_n which is acting in the normal direction to the cross section, and F_s which is acting parallel to the section. The normal stress is quantified as:

$$\sigma_n = \frac{F_n}{A} \tag{3.2}$$

while the parallel stress is also known as shear stress and is quantified as:

$$\tau = \frac{F_S}{A} \tag{3.3}$$

Material failure can be caused by the normal stress (tensile or compressive failure), or the shear stress (shear failure) by shearing the material along a plane, as shown in Figure 3.1.

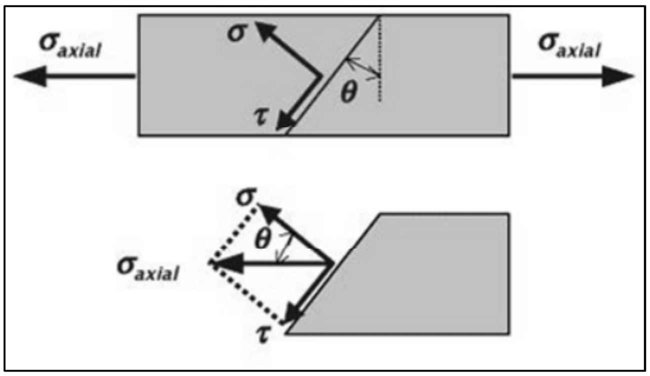

Figure 3.1 Stress components showing the normal and shear stress (Aadnoy and Looyeh, 2011).

Zoback (2010) describes stress as a second-rank tensor with nine components which construe the density of forces acting on all surfaces passing through a given point. All of these nine components are shown as:

$$S = \begin{bmatrix} S_{11} & S_{12} & S_{13} \\ S_{21} & S_{22} & S_{23} \\ S_{31} & S_{32} & S_{33} \end{bmatrix}, \tag{3.4}$$

The nine components define the direction the force and the face it is acting on. Since each component is acting perpendicular to two axis and acting in one direction, there are nine magnitudes and three directions to define, as shown in Figure 3.2.

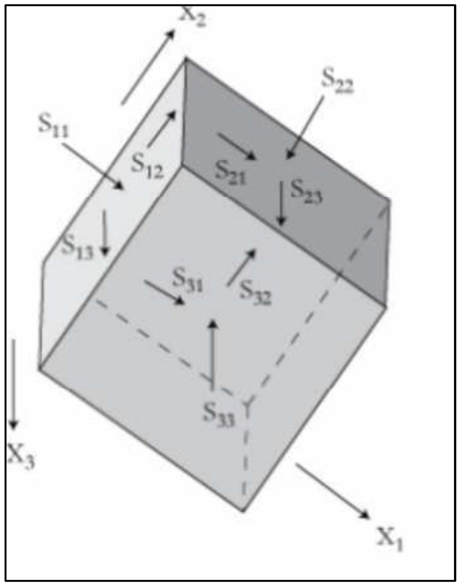

Figure 3.2 Stress tensor in arbitrary Cartesian coordinate system (Zoback, 2010).

3.2 Stress Magnitude at Depth

For the application of the stress concept in the subsurface, it helps to simplify the stress tensor into three principle stresses, which are the stresses that are acting in a direction such that there is no shear stress. Hence, the tensor becomes:

$$S = \begin{bmatrix} S_{11} & S_{12} & S_{13} \\ S_{21} & S_{22} & S_{23} \\ S_{31} & S_{32} & S_{33} \end{bmatrix} = \begin{bmatrix} \sigma_x & \tau_{xy} & \tau_{xz} \\ \tau_{yx} & \sigma_y & \tau_{yz} \\ \tau_{zx} & \tau_{zy} & \sigma_z \end{bmatrix} = \begin{bmatrix} \sigma_1 & 0 & 0 \\ 0 & \sigma_2 & 0 \\ 0 & 0 & \sigma_3 \end{bmatrix} \tag{3.5}$$

σ_1, σ_2, and σ_3 are known as maximum, intermediate, and minimum principal stresses. In earth's subsurface, principle stresses are addressed as S_v, S_{Hmax}, and S_{hmin}, respectively are vertical stress, maximum horizontal stress, and minimum horizontal stress. The vertical stress is affected by the overburden of the sediments above, while the horizontal stresses are caused by the tectonic and geological depositional processes.

Anderson classifies the stress regime of an area based on the magnitudes of the horizontal stress with respect to the vertical stress. The Anderson classification is described in Table 3.1.

Table 3.1 Relatives magnitudes and stress regimes

Regime	Stress		
	S_1	S_2	S_3
Normal	S_v	S_{Hmax}	S_{hmin}
Strike-slip	S_{Hmax}	S_v	S_{hmin}
Reverse	S_{Hmax}	S_{hmin}	S_v

The magnitude of vertical stress or overburden stress at depth is depended on the weight of the overlaying rock above it. The overburden stress is the integration of densities of rock and its magnitude increases with increasing depth. It can be written as:

$$S_v = \int \rho(z) g z = \tilde{\rho} g z \tag{3.6}$$

where $\rho(z)$ is density as a function of depth and g is gravitational acceleration. For offshore areas, the equation considers the water above the surface:

$$\mathrm{S}_v = \rho_w \mathrm{g} \mathrm{z}_w + \int \rho(\mathrm{z})\mathrm{gz} \tag{3.7}$$

where ρ_w is water density, and z_w is the water depth.

There is no direct method to measure the magnitude of maximum horizontal stress. However, there are techniques to predict S_{hmax} based on the fact that pore pressure should not exceed the least principle stress to avoid tensile fracturing, and the difference of maximum and minimum stress cannot exceed the crustal strength. In an isotropic environment the magnitude of both horizontal stresses will be equal, which is possible in an area without influences of earthquake and tectonic movements, usually in the shallow intervals to approximately 600 m.

Several types of lab measurements techniques are available to predict the in-situ stresses in laboratory. Those techniques are hydrostatic, uniaxial, triaxial, and polyaxial tests. There are also some correlations to predict the magnitudes of horizontal stresses at depth for specific regions in literatures. However, these methods should not replace lab measurements.

3.3 Stress Around A Vertical Wellbore

During the drilling process, the excavation and removal of material from the borehole cause the formation surrounding the wellbore wall to be subjected to stress concentrations whose magnitude varies based on the position around the well. The stress alteration around the wellbore can cause compressive failure in the form of wellbore breakouts or tensile failure of the wellbore wall. Therefore, the induced stresses should be adjusted through mud pressure. In severe condition these breakouts can lead into major wellbore instability problems, such as stuck pipe and hole enlargement. The formation response toward drilling is dependent on its rock strength and the in-situ stress field.

As reported in Aadnoy and Loyeh (2011), a theoretical approach was introduced by Ernst Gustav Kirsch in 1898, which is widely used to mathematically determine the stresses around a wellbore of a previously stressed virgin rock. Kirsch's equations are based on linear elasticity and assume the rock properties are homogeneous and isotropic. He calculates the effective stresses at a point in cylindrical coordinate (r, θ) around the wellbore, which can be described as:

$$\sigma_{rr} = \left(\frac{\sigma_x^0 + \sigma_y^0}{2}\right)\left(1 - \frac{a^2}{r^2}\right) + \left(\frac{\sigma_x^0 - \sigma_y^0}{2}\right)$$
$$\left(1 + 3\frac{a^4}{r^4} - 4\frac{a^2}{r^2}\right)\cos 2\theta + \sigma_{xy}^0\left(1 + 3\frac{a^4}{r^4} - 4\frac{a^2}{r^2}\right)\sin 2\theta + P_w\frac{a^2}{r^2} \quad (3.8)$$

$$\sigma_{\theta\theta} = \left(\frac{\sigma_x^0 + \sigma_y^0}{2}\right)\left(1 + \frac{a^2}{r^2}\right) - \left(\frac{\sigma_x^0 - \sigma_y^0}{2}\right)\left(1 + 3\frac{a^4}{r^4}\right)\cos 2\theta - \sigma_{xy}^0\left(1 + 3\frac{a^4}{r^4}\right)\sin 2\theta - P_w\frac{a^2}{r^2}$$

(3.9)

$$\sigma_{zz} = \sigma_z^0 - v\left[2\left(\sigma_x^0 - \sigma_y^0\right)\frac{a^2}{r^2}\cos 2\theta + 4\sigma_{xy}^0\frac{a^2}{r^2}\sin 2\theta\right] \tag{3.10}$$

$$\tau_{r\theta} = \left[-\left(\frac{\sigma_x^0 - \sigma_y^0}{2}\right)\left(1 - 3\frac{a^4}{r^4} + 2\frac{a^2}{r^2}\right)\sin 2\theta\right] + \tau_{xy}^0\left(1 - 3\frac{a^4}{r^4} + 2\frac{a^2}{r^2}\right)\cos 2\theta \tag{3.11}$$

$$\tau_{rz} = \left(\tau_{xz}^0\cos\theta + \tau_{yz}^0\sin\theta\right)\left(1 - \frac{a^2}{r^2}\right) \tag{3.12}$$

$$\tau_{\theta z} = \left(-\tau_{xz}^0\sin\theta + \tau_{xz}^0\cos\theta\right)\left(1 + \frac{a^2}{r^2}\right) \tag{3.13}$$

where "a" is the radius of the wellbore, *r* is distance from the borehole, p_w is the internal wellbore pressure, and v is Poisson's ratio, angle θ is measured clockwise from x-axis, σ_{rr} is the radial stress, $\sigma_{\theta\theta}$ is tangential stress, σ_{zz} is axial stress, $\tau_{\theta z}$, $\tau_{r\theta}$, and τ_{rz} are three components of the shear stress.

At the wellbore of anisotropic rock, where a=*r*, Kirsch equations can be written as:

$$\sigma_{rr} = P_w \tag{3.14}$$

$$\sigma_{\theta\theta} = \left(\sigma_x^0 + \sigma_y^0\right) - 2\left(\sigma_x^0 - \sigma_y^0\right)\left(1 + 3\frac{a^4}{r^4}\right)\cos 2\theta - 4\,\sigma_{xy}^0\sin 2\theta - P_w \tag{3.15}$$

$$\sigma_{zz} = \sigma_z^0 - 2v\left(\sigma_x^0 - \sigma_y^0\right)\cos 2\theta - 4v\,\tau_{xy}^0\sin 2\theta \tag{3.16}$$

$$\tau_{r\theta} = 0 \tag{3.17}$$

$$\tau_{rz} = 0 \tag{3.18}$$

$$\tau_{\theta z} = 2\left(-\tau_{xz}^0\sin\theta + \tau_{xz}^0\cos\theta\right) \tag{3.19}$$

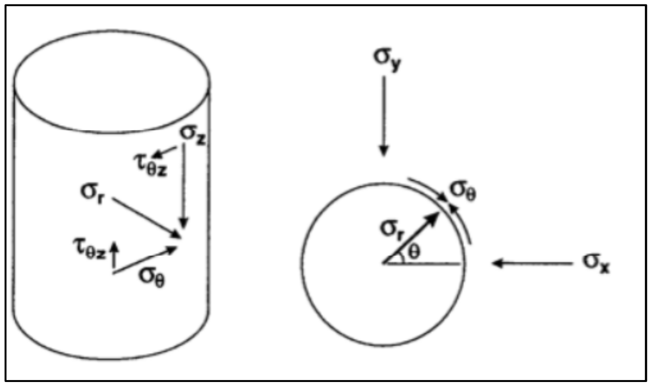

Figure 3.3 Position of stresses around a wellbore in the rock formation (Aadnoy and Looyeh, 2011).

3.4 Stress Distribution Around Inclined Wellbore

For inclined wells, stress components should be transformed and adjusted to the well inclination from vertical (γ), geographical azimuth of the wellbore (φ), and the wellbore position from the x-axis (θ). Aadnoy and Looyeh (2011) explained the coordinate transformation of the in-situ stresses in inclined wellbore into a new Cartesian coordinate system, as shown in Figure 3.4. This transformation is important before deriving the stresses around the wellbore using Kirsch concept.

The stress transformation is written as follows:

$$\sigma_x = (\sigma_{Hmax} cos^2\varphi + \sigma_{hmin} sin^2\varphi)\ cos^2\gamma + \sigma_v sin^2\gamma \tag{3.20}$$

$$\sigma_y = \sigma_{Hmax} sin^2\varphi + \sigma_{hmin} cos^2\varphi \tag{3.21}$$

$$\sigma_{zz} = (\sigma_{Hmax} cos^2\varphi + \sigma_{hmin} sin^2\varphi)\ sin^2\gamma + \sigma_v cos^2\gamma \tag{3.22}$$

$$\tau_{xy} = 0.5(\sigma_{hmin} - \sigma_{Hmax}) sin2\varphi . cos\ \gamma \tag{3.23}$$

$$\tau_{xz} = 0.5(\sigma_{Hmax} cos^2\varphi + \sigma_{hmin} sin^2\varphi - \sigma_v) sin2\gamma \tag{3.24}$$

$$\tau_{yz} = 0.5(\sigma_{hmin} - \sigma_{Hmax}) sin2\varphi . sin\,\gamma \tag{3.25}$$

where σ_x, σ_y, σ_{zz}, τ_{xy}, τ_{xz}, and τ_{yz} are the transformed stress components. σ_{Hmax}, σ_{hmin}, σ_v are the principle stresses, φ is the wellbore azimuth from the direction of σ_{Hmax}, and γ is the wellbore inclination from the vertical.

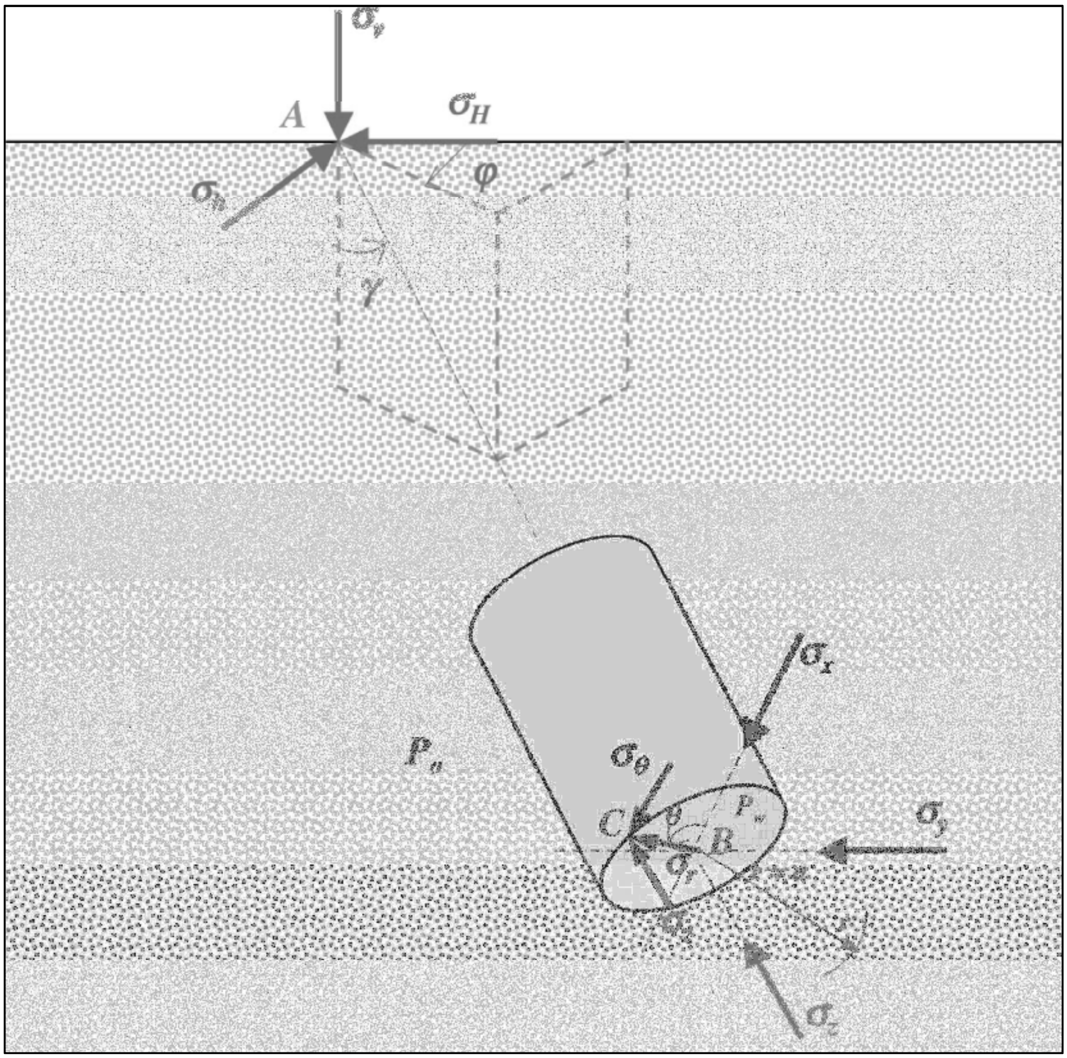

Figure 3.4 Position of stresses around a wellbore (Aadnoy and Looyeh, 2011).

Equations 3.20–3.25 can also be shown in matrix format:

$$\begin{bmatrix}\sigma_x\\ \sigma_y\\ \sigma_{zz}\end{bmatrix}=\begin{bmatrix}cos^2\varphi\, cos^2\gamma & sin^2\varphi\, cos^2\gamma & sin^2\gamma\\ sin^2\varphi & cos^2\varphi & 0\\ cos^2\varphi sin^2\gamma & sin^2\varphi sin^2\gamma & cos^2\gamma\end{bmatrix}\begin{bmatrix}S_{Hmax}\\ S_{hmin}\\ S_v\end{bmatrix} \tag{3.26}$$

$$\begin{bmatrix}\tau_{xy}\\ \tau_{xz}\\ \tau_{yz}\end{bmatrix}=\begin{bmatrix}-sin2\varphi cos\gamma & sin2\varphi cos\gamma & 0\\ cos^2\varphi sin2\gamma & sin^2\varphi sin2\gamma & -sin2\gamma\\ -sin2\varphi sin\,\gamma & sin2\varphi sin\,\gamma & 0\end{bmatrix}\begin{bmatrix}S_{Hmax}\\ S_{hmin}\\ S_v\end{bmatrix} \tag{3.27}$$

After the transformation, these components are converted into stresses components in Kirsch's cylindrical coordinate system, as follows:

$$\sigma_r = \frac{1}{2}\left(\sigma_x+\sigma_y\right)\left(1-\left(\frac{a}{r}\right)^2\right)+\frac{1}{2}(\sigma_x-\sigma_y)(1+3\left(\frac{a}{r}\right)^4-4\left(\frac{a}{r}\right)^4\cos 2\theta+\tau_{xy}(1+3\left(\frac{a}{r}\right)^4 - 4\left(\frac{a}{r}\right)^2\sin 2\theta+\Delta p_w\left(\frac{a}{r}\right)^2, \tag{3.28}$$

$$\sigma_\theta = \frac{1}{2}\left(\sigma_x+\sigma_y\right)\left(1+\left(\frac{a}{r}\right)^2\right)-\frac{1}{2}(\sigma_x-\sigma_y)(1+3\left(\frac{a}{r}\right)^4\cos 2\theta-\tau_{xy}(1+3\left(\frac{a}{r}\right)^4\sin 2\theta - \Delta p_w\left(\frac{a}{r}\right)^2, \tag{3.29}$$

$$\sigma_z = \sigma_{zz}-2v\left(\sigma_x+\sigma_y\right)\left(\frac{a}{r}\right)^2\cos 2\theta-4v\tau_{xy}\left(\frac{a}{r}\right)^2\sin 2\theta \tag{3.30}$$

$$\tau_{\theta z} = \left(\tau_{yz}\cos\theta-\tau_{xz}\sin\theta\right)\left(1+\left(\frac{a}{r}\right)^2\right) \tag{3.31}$$

$$\tau_{rz} = \left(\tau_{xz}\cos\theta+\tau_{yz}\sin\theta\right)\left(1-\left(\frac{a}{r}\right)^2\right) \tag{3.32}$$

$$\tau_{r\theta} = \left(\frac{1}{2}(\sigma_x - \sigma_y)\sin 2\theta + \tau_{xy}\cos 2\theta\right)\left(1 - 3\left(\frac{a}{r}\right)^4 + 2\left(\frac{a}{r}\right)^2\right), \tag{3.33}$$

where a is the radius of wellbore, r is the outer radius, θ is the wellbore position from the x-axis, Δp_w is the internal wellbore pressure which is the difference between the wellbore pressure and pore pressure:

$$\Delta p_w = P_w - P_p \tag{3.34}$$

For the stresses component at the wellbore wall, where a=r, the equations become:

$$\sigma_r = \Delta p_w \tag{3.35}$$

$$\sigma_\theta = (\sigma_x + \sigma_y - \Delta p_w) - 2(\sigma_x - \sigma_y)\cos 2\theta - 4v\tau_{xy}\sin 2\theta \tag{3.36}$$

$$\sigma_z = \sigma_{zz} - 2v(\sigma_x - \sigma_y)\cos 2\theta - 4v\tau_{xy}\sin 2\theta \tag{3.37}$$

$$\tau_{r\theta} = \tau_{rz} = 0 \tag{3.38}$$

$$\tau_{\theta z} = 2(\tau_{yz}\cos\theta - \tau_{xz}\sin\theta) \tag{3.39}$$

The arbitrarily effective principle stresses at the wellbore wall can be calculated using the following equations:

$$\sigma_{tmax} = \frac{1}{2}(\sigma_\theta + \sigma_z) + \frac{1}{2}\sqrt{(\sigma_\theta - \sigma_z)^2 + 4\tau_{\theta z}{}^2} \tag{3.40}$$

$$\sigma_{tmin} = \frac{1}{2}(\sigma_\theta + \sigma_z) - \frac{1}{2}\sqrt{(\sigma_\theta - \sigma_z)^2 + 4\tau_{\theta z}{}^2} \tag{3.41}$$

$$\sigma_{rr} = \sigma_r = \Delta pw \tag{3.42}$$

where σ_{tmax} and σ_{tmin} respectively are the largest and the smallest principle stresses around the wellbore. These calculations are used to assess the wellbore stability described in the following sections.

3.5 Effects of Chemical Interaction, Temperature, and Flow-Induced Stresses

3.5.1 Chemical Interaction

The difference between the chemical composition of the drilling mud and the formation fluids may cause chemical interaction between them. Chemical interaction in shale formation can be critical because of the reactive swelling clay minerals. Therefore, careful mud selection should be conducted to minimize the interaction. The low permeability of shale makes creating mud cake at the wellbore wall difficult, causing water and pressure penetrating within the shale matrix and pores and increasing the pore pressure (Mese and Tutuncu 2011). This increase in pore pressure can lead to stress alteration at the wellbore and cause yielding of shale. When the mud pressure applied within the wellbore cannot support the formation fluid pressure, shale yielding can take place in the form of sloughing into the wellbore. Depending on the compatibility of the chemical composition of the formation fluid and the drilling fluid, the shale formation creates an additional pressure called "swelling pressure" that needs to also be included in the mud pressure calculations and drilling fluid design. Hence, the effects of chemical interaction on the stress state around the wellbore should be considered in the calculation.

To calculate the effect of chemical interaction, numeral equations for osmotic pressure can be derived from several equations by Chen et al. (2001) and equations provided in the Well Integrity class (Tutuncu, 2015), as follows:

$$\sigma_r{}' = 0 \tag{3.44}$$

$$\sigma_\theta{}' = \alpha \frac{1-2v}{1-v} \Delta\Pi \tag{3.45}$$

$$\sigma_z{}' = \alpha \frac{1-2v}{1-v} \Delta\Pi \tag{3.46}$$

where σ_r', σ_θ' and σ_z' are the alteration of radial, hoop and axial stresses due to the introduction of the osmotic pressure, α is the Biot's coefficient, v is Poisson's ratio, and $\Delta\Pi$ is the osmotic pressure.

The effects of excess pore pressure on the osmotic potential can be expressed as (Tutuncu, 2012):

$$\Delta\Pi = I_m * \left(\frac{RT_o}{V_w}\right) \ln \frac{a_{w,df}}{a_{w,sh}} \tag{3.47}$$

where I_m is a reactivity coefficient which characterizes membrane efficiency, a dimensionless parameter and ranges from 0 to 1, R is the universal gas constant and equals 8.314 J/K.mole, T_o is the absolute temperature, K. V_w is the molar volume of the water (18.104 m^3), $a_{w,df}$ and $a_{w,sh}$ are chemical activities of the drilling fluid and shale pore water, respectively. Chemical activity for fresh water equals to 1, and for salt water is less than 1.

3.5.2 Temperature Alteration

Circulation of cold drilling fluid into the wellbore can cause stress alteration due to rock temperature change. Aadnoy and Looyeh (2011) calculate the thermal stress induced as follows:

$$\sigma_T = \frac{\alpha_m * E * (T - T_o)}{1 - v} \tag{3.48}$$

where v is the Poisson's ratio, E is Young modulus, α_m is a volumetric thermal expansion coefficient of rock matrix (°K^{-1}), T is the circulation temperature (°K), and T_o is virgin rock temperature (°K).

3.5.3 Flow Induced Stress

Kadyrov (2012) describes the effects of flow-induced stresses in the equations that define the stress alteration at the wellbore when a radial flow is introduced due to the overbalanced or underbalanced drilling.

$$\sigma_r{}^{"} = 0 \tag{3.49}$$

$$\sigma_\theta{}^{"} = -(1-\alpha)\frac{1-2v}{1-v}(P_w - P_o) \tag{3.50}$$

$$\sigma_z{}^{"} = -(1-\alpha)\frac{1-2v}{1-v}(P_w - P_o) \tag{3.51}$$

where P_w-P_o =ΔP_w

By adding the effects of chemical interaction, temperature alteration, and flow induced stress, the numerical model can be expressed as:

$$\sigma_r = \Delta p_w \tag{3.52}$$

$$\begin{aligned}\sigma_\theta = {} & \left(\sigma_x + \sigma_y - \Delta p_w\right) - 2\left(\sigma_x - \sigma_y\right)\cos 2\theta \\ & - 4v\tau_{xy}\sin 2\theta + \alpha\frac{1-2v}{1-v}\Delta\Pi + \frac{\alpha_m * E * (T - T_o)}{1-v} - (1 \\ & - \alpha)\frac{1-2v}{1-v}(P_w - P_o)\end{aligned} \tag{3.53}$$

$$\begin{aligned}\sigma_z = {} & \sigma_{zz} - 2v\left(\sigma_x - \sigma_y\right)\cos 2\theta \\ & - 4v\tau_{xy}\sin 2\theta\alpha\frac{1-2v}{1-v}\Delta\Pi + \frac{\alpha_m * E * (T - T_o)}{1-v} \\ & - (1-\alpha)\frac{1-2v}{1-v}(P_w - P_o)\end{aligned} \tag{3.54}$$

$$\tau_{r\theta} = \tau_{rz} = 0 \tag{3.55}$$

$$\tau_{\theta z} = 2(\tau_{yz}\cos\theta - \tau_{xz}\sin\theta) \tag{3.56}$$

3.6 Rock Failure Modes

Understanding the types and reasons of formation failures is important as prevention and also for mitigation. Wellbore log data such as caliper and image logs are helpful to provide information identifying wellbore failures during drilling. Analyzing wellbore image data also help in providing reliable information about the failure mode, whether it is tensile, compressional, or shear failure.

3.6.1 Tensile Failure

Tensile failure in a wellbore occurs when the tensile strength acting across the plain exceed the maximum limit of the rock tensile strength. One of the examples of tensile failure is drilling induced hydraulic fractures. These fractures are occurs due to the concentration of in-situ regional stresses, pore pressure, drilling mud pressure, and thermal stresses due to cooling of borehole during drilling. Tensile strength has the same unit as stress, usually rocks have very low tensile strength and in most applications where the formation contains natural fractures, tensile strength is assumed to be zero.

3.6.2 Shear Failure

Shear failure is also known as compressive failure; it takes place when the compressive loading makes the shear stress along the plane high enough to cause the rock undergo shear failure. Borehole collapse during drilling is an example of shear failure.

The shape of the collapse is determined by the stresses around the wellbore. Various shapes of wellbore collapse based on their stresses are shown in Figure 3.5. If the mud pressure in the well is the same as the formation pore pressure, the wellbore will still be in the circular shape. In the case when the stresses are different, the shape of the wellbore will be elongated due to collapse. In a vertical well wellbore, breakout will occur in the direction of the minimum in-situ stress direction.

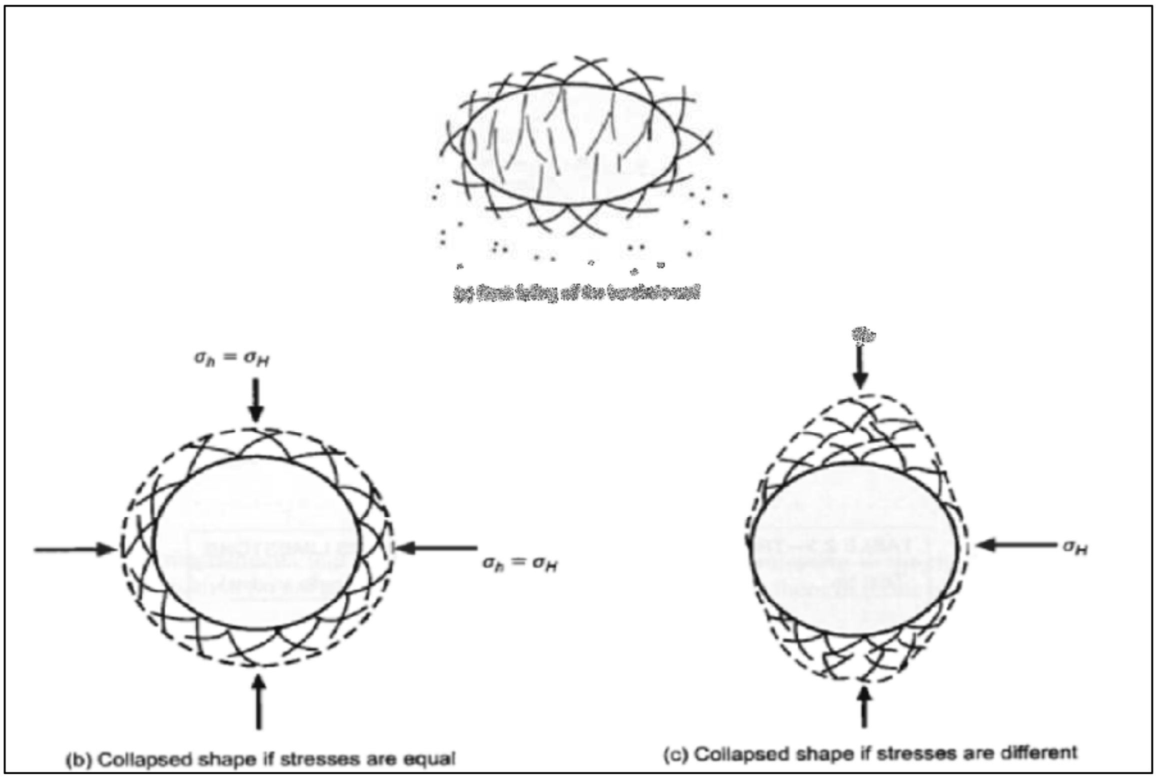

Figure 3.5 Collapse of borehole wall (Mitchell et al., 2011).

3.6.3 Creep Failure

Creep failure takes place when the rock formation undergoes deformation under constant stress over time. There are three stages of creep failure based on the mechanism for creep applies to a specific case. The first stage is transient creep, when the stresses cause microfractures in the rock, but if the stresses are reduced to zero, the deformation will eventually disappear. The second stage is the steady state creep, where the deformation will not disappear completely even after the stresses that caused it are released to zero. The third stage is accelerating creep, where the creep will accelerate over time and quickly lead to failure (Fjær et al. 2008).

3.6.4 Pore Collapse or Comprehensive Failure

Pore collapse takes place when the effective stress (in situ overburden stress minus pore pressure) exceeds the compressive strength of the formation causing failure. Pore collapse typically occurs in a depleted reservoir due to compaction. Pore collapse can be seen as shear failure within the material, because in microscopic manner it happens due to local excessive shear forces acting through grains and grains contacts.

3.7 Rock Failure Criteria

Wellbore failure can be caused by many different mechanisms as mentioned in section 3.6. Different lithologies will fail in different manners, sandstones may fail in shear, while claystones can fail due to plastic deformation. To predict the wellbore stability, an appropriate failure criterion should be used and representing the true in situ stress and pore pressure conditions. There are several of rock failure criteria. In the following section, a brief review of two failure criteria that were used for case study analysis are briefly discussed.

3.7.1 Mohr Coulomb Criterion

This method is the most commonly used failure criterion used in the oil and gas industry to predict wellbore failure due to its simplicity. A relationship between the shearing resistance to the contact forces and friction is provided using this criterion. The Mohr-Coulomb criterion is based on the assumption that the shear strength linearly increases with the effective mean stress and the relationship can expressed in the equation below

$$\tau_{max} = C + \sigma_{m,2} \tan \phi \tag{3.57}$$

$$\tau_{max} = \frac{\sigma_1 - \sigma_3}{2} \tag{3.58}$$

$$\sigma_{m,2} = \frac{\sigma_1 + \sigma_3}{2} \tag{3.59}$$

where τ_{max} is shear stress, $\sigma_{m.2}$ is the normal stress, C and ϕ are cohesion and internal friction angle. The compressional failure occurs when the value of the maximum shear stress (τ_{max}) is enough to overcome the formation cohesion (*C*) and frictional force. Therefore, the Mohr-Coulomb compressional failure depends only on two principal stress magnitudes, the maximum (σ_1) and minimum principal stresses (σ_3). The failure envelope is determined using minimum three core measurements for creating the Mohr's circles where each circle is one triaxial test, as shown in the Figure 3.7.

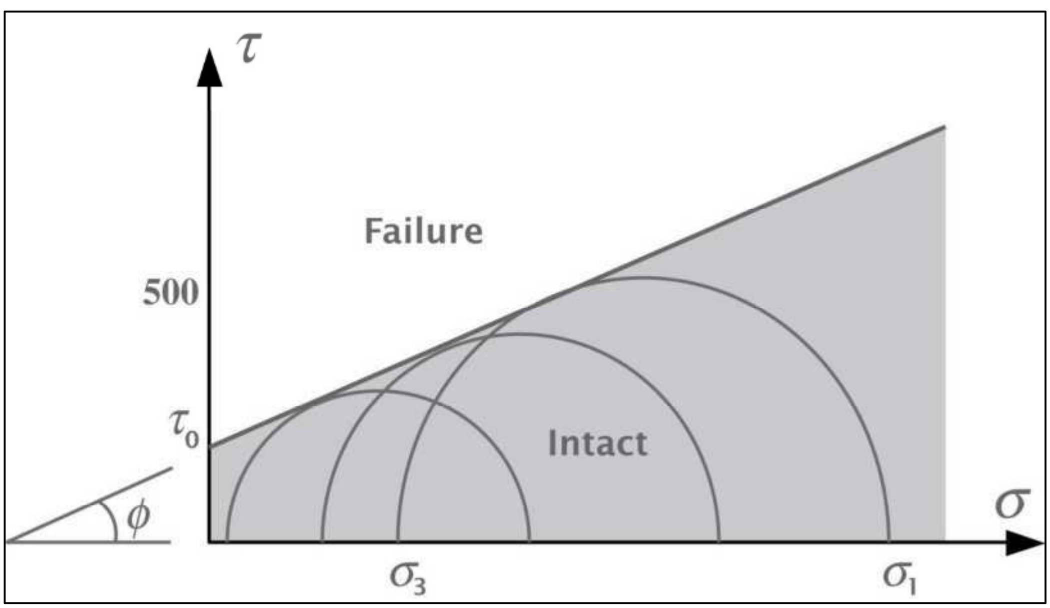

Figure 3.6 Mohr-Coulomb failure model from triaxial test data (Aadnoy and Looyeh, 2011).

Islam et al. (2010) developed the numerical solution for the Mohr-Coulomb failure criterion which can be expressed in equation 3.46.

$$F = C * \cos\phi + \sin\phi * \left(\sigma_{m,2} - P_p\right) - \tau_{max} \tag{3.60}$$

where P_p is pore pressure. Compressional failure occurs when F is less than or equal to zero.

As stated in many publications including in Vernik and Zoback (1992), Ewy (1999), Al-Ajmi and Zimmerman (2006), Mohr-Coulomb criterion delivers over-predicted results, therefore application of this criterion should be with caution to represent the true in situ stress state.

3.7.2 Mogi-Coulomb Failure Criterion

Al-Ajmi and Zimmerman (2006) have used the Mogi-Coulomb failure criterion to reduce the weakness introduced in the Mohr-Coulomb criterion. They have brought the fact that the intermediate principle stress has an effect on the rock failure, and express it as follows:

$$\tau_{oct} = a + b\sigma_{m,2}$$

where τ_{oct} is octahedral stress, a and b are the Coulomb strength parameters, and $\sigma_{m,2}$ is the mean stress. The octahedral shear stress and the Coulomb strength parameters are expressed as:

$$\tau_{oct} = \frac{1}{3}\sqrt{(\sigma_1 - \sigma_2)^2 + (\sigma_2 - \sigma_3)^2 + (\sigma_3 - \sigma_1)^2} \tag{3.61}$$

$$a = \frac{2\sqrt{2}}{3} c \cos\emptyset \tag{3.62}$$

$$b = \frac{2\sqrt{2}}{3} c \sin\emptyset \tag{3.63}$$

If $\sigma_1 = \sigma_2$ or $\sigma_2 = \sigma_3$ the Mogi-Coulomb failure criterion is reduced to the Mohr-Coulomb failure criteria. Therefore, Mogi-Coulomb criterion can be considered as an extension of Mohr-

Coulomb criterion into a polyaxial stress state in which $\sigma_1 \neq \sigma_2 \neq \sigma_3$. Based on their experimental study results, Al-Ajmi and Zimmerman concluded that the Mogi-Coulomb criterion is currently the most accurate failure model for hard sedimentary rocks formations.

3.7.3 Tensile Failure Criterion

In this criterion, the formation will fail in tensile mode when the least compressive principle stress at the wellbore exceeds the tensile strength of the rock, which can be expressed as follows (Yu et al. 2001):

$$F = \tau_{t\,min} + T_s \tag{3.64}$$

where τ_{tmin} is the effective minimum compressional principle stress at the wellbore and T_s is the tensile strength of formation.

CHAPTER 4

INPUT PARAMETERS FOR WELLBORE STABILITY ANALYSIS

To create a realistic and representative geomechanical model for wellbore stability analysis, it is important to prepare the input parameters accurately. The same input parameters used for constraining earth models are used in the numerical geomechanical model. The list of the input parameters in this study and the methodologies used to obtain the input data are described in the subsequent sections.

4.1 Overburden Stress

Overburden stress is the confining pressure imposed by the lithostatic column on a layer of soil or rock at a given depth due to the weight of the overlying materials. The value of overburden pressure can be calculated from a direct integration of the bulk density measured in the well of the interest area. Since the density logs (RHOB) typically recorded only at deeper intervals, the synthetic log is built and constrained using the indicative trends observed in the available section and or in a nearby offset well if the density log is not collected. Also need to be taken into accounts is the effects of near-wellbore washouts and adverse water-shale interactions that will affect the bulk density value. van Oort et al. (2001) reported that the "stress arching" effect can deflect the calculated overburden stress from the actual one. In this study, the "stress arching" effect is not considered. Density logs are available for 50% of wells in this field, yet mostly only measured 10% of the total depth. Therefore, the overburden stress is obtained from integrating the measured density log RHOB and synthetic density logs. The equation for overburden stress expressed as follows:

$$S_v = \int \rho(z)gz = \tilde{\rho}gz \tag{4.1}$$

where $\rho(z)$ is density as a function of depth and g is gravitational acceleration. In terms of a 1D geomechanical model, overburden stress corresponds to the vertical stress, one of the principal stresses. The determination of density synthetic log in this study is described by Figure 4.1 where extrapolation and Gardner methods deliver the best fit. The value of bulk density that is used for overburden calculation is the combination of RHOB log value with the RHOB extrapolation log as shown in Figure 4.2.

There are several correlations that can be used to create the synthetic density logs:

4.1.1 Extrapolated Density

Density is extrapolated from the mud line using following correlation:

$$\rho_{extrapolated} = A_o(TVD)^{\alpha} \tag{4.2}$$

where A_o and α are the fitting parameters.

4.1.2 Amoco Density

The average bulk density below the sea floor is estimated by an empirical equation obtained from statistical data from the Gulf of Mexico.

$$\rho_{Amoco} = A_o[(TVD)/3125]^{\alpha} \tag{4.3}$$

where A_o and α are the fitting parameters.

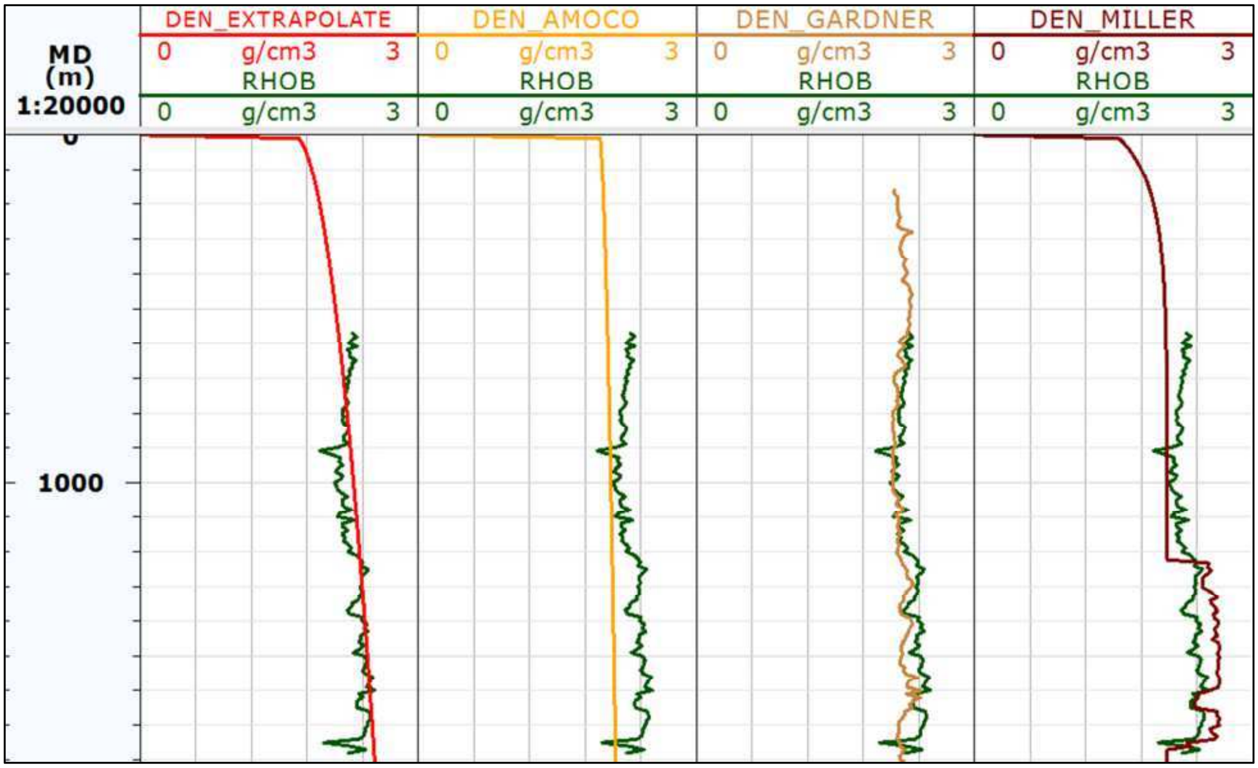

Figure 4.1 Synthetic density for the well X-01.

4.1.3 Gardner Density

This correlation calculates the synthetic density from sonic or seismic data.

$$\rho_{Gardner} = a \; x \; V^{\beta} \tag{4.4}$$

where α and β are two fitting parameters respectively named velocity factor and velocity exponent, and *V* is sonic or seismic formation velocity in ft/s.

4.1.4 Miller Density

Miller density is calculated from porosity log, expressed as follows:

$$\rho_{Miller} = \rho_{matrix}(1 - \emptyset_{Miller}) \tag{4.5}$$

$$\emptyset_{Miller} = \emptyset_a + \emptyset_b{}^{e^{\left(-k(TVD)^{\frac{1}{N}}\right)}} \tag{4.6}$$

where ρ_{matrix} is matrix density (default 2.65 g/cm3, $\emptyset_a$ sediment porosity at great depth, $\emptyset_b$ sediment porosity fitting parameter equal, k is porosity decline parameter, and N is curvature parameter.

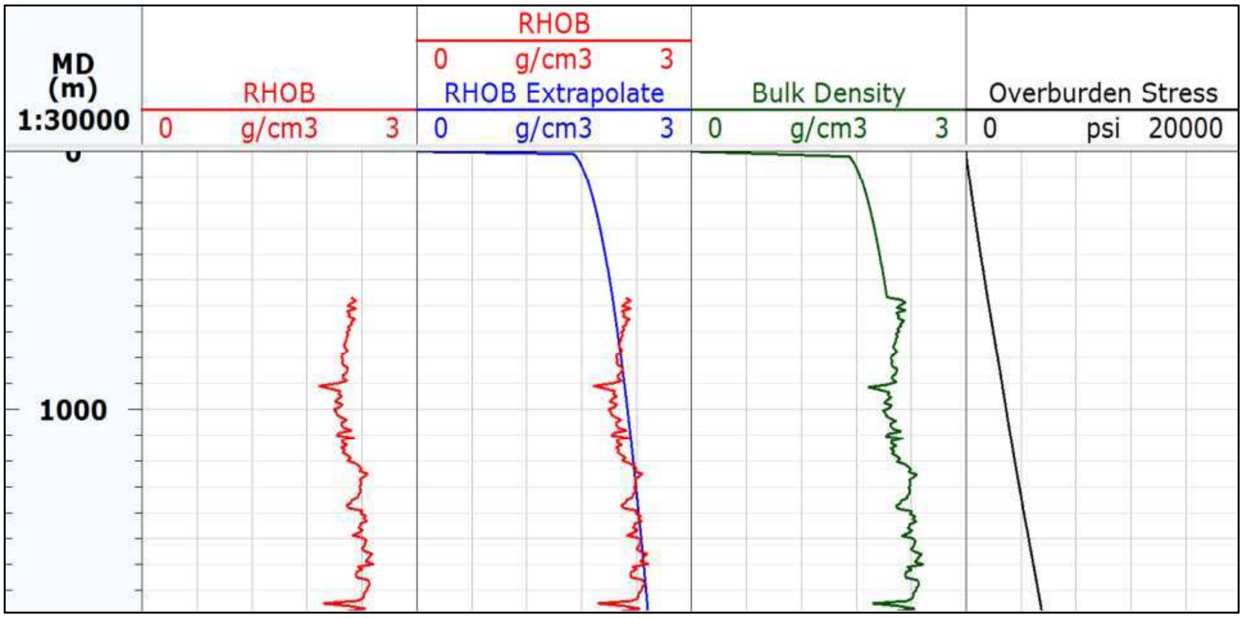

Figure 4.2 The overburden stress for the well X-01.

4.2 Pore Pressure

Formation pore pressure is one of the most challenging input that will impact having successful drilling operations, reservoir characterization, and production optimization. In integrated wellbore stability studies, pore pressure is an important input parameter to determine the in-situ stress state. The most reliable method to determine pore pressure obtained from wireline measurements at the productive reservoir intervals, such as the data from well testing analysis. However, in solving wellbore stability problems it is critical to determine the pore pressure of other formations outside the productive reservoirs, especially the overburden intervals along the proposed well path profile. Based on data availability, there are two types of methods that will be used in this study to determine the pore pressure; the normal trend method (Eaton), and explicit method (Holbrook).

4.2.1 Eaton Pore Pressure

This method was introduced by Eaton (1975) and perhaps the most widely publicized pore-pressure-estimation technique. It is based on the relationship between the observed parameter/normal parameter ratio and the formation pressure on the changes in the overburden gradient, i.e. compaction rate. To deliver the pore pressure gradient with this method, we need to determine the shale depth-dependent normal compaction trendline (NCT) in the condition of hydrostatic pore pressure. Eaton empirical relationship from sonic or resistivity log data can be expressed as:

$$Pp = S_v - Pp_{normal}\left(\frac{\Delta t_{normal}}{\Delta t_o}\right)^3 \tag{4.7}$$

$$Pp = S_v - Pp_{normal}\left(\frac{R_o}{R_{normal}}\right)^{1.2} \tag{4.8}$$

where P_p is formation pressure gradient, S_v is overburden gradient, $P_{pnormal}$ is normal hydrostatic pressure gradient, Δt_{normal} is normal shale compressional slowness, Δt_o is compressional slowness observed form sonic log, R_o is resistivity observed from log, and R_{normal} is normal shale resistivity. The original exponent values reported by Eaton has been obtained using Gulf Coast data while in other regions of the US and globally, the exponents needs to be revised for the regional exponents where the study area is. An example for pore pressure calculation using this method is shown in Figure 4.3.

Figure 4.4 presents the results of Eaton pore pressure calculation in comparison with field data that are obtained from the wireline measurements. The field pressure data were gathered not long after wireline logging to avoid the depletion effects. The comparison of the predicted pore pressure from Eaton method with real field measurements presented good agreement.

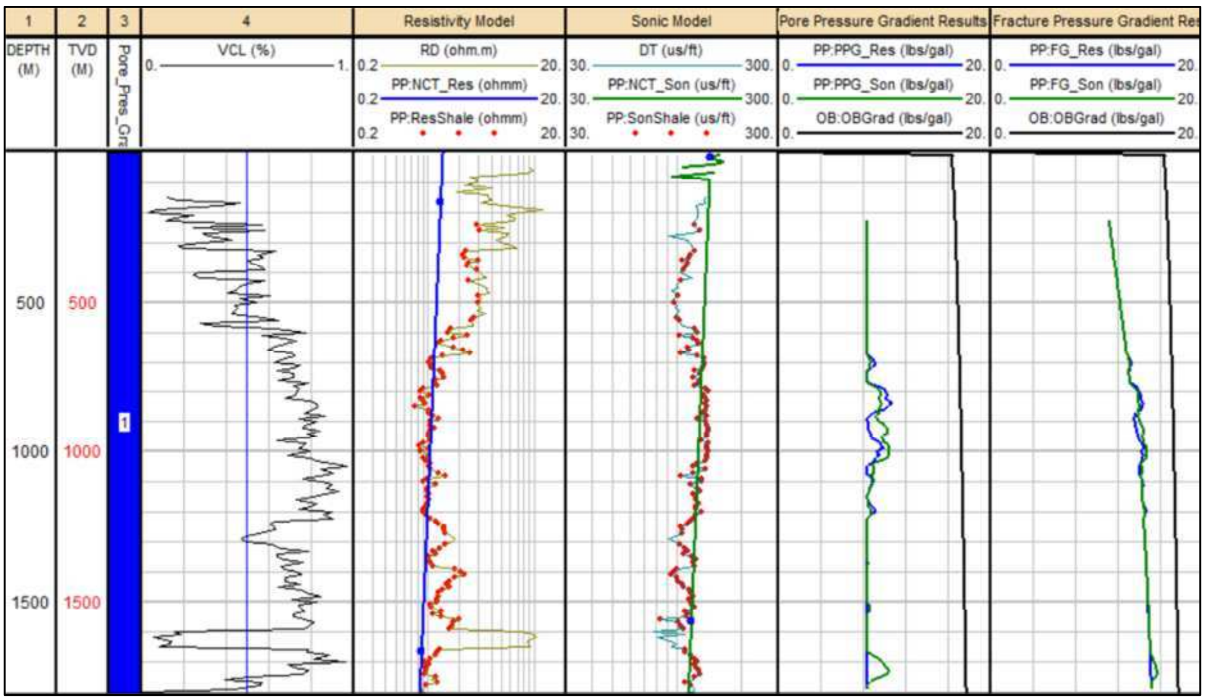

Figure 4.3 Eaton pore pressure calculation using resistivity and sonic model well X-01.

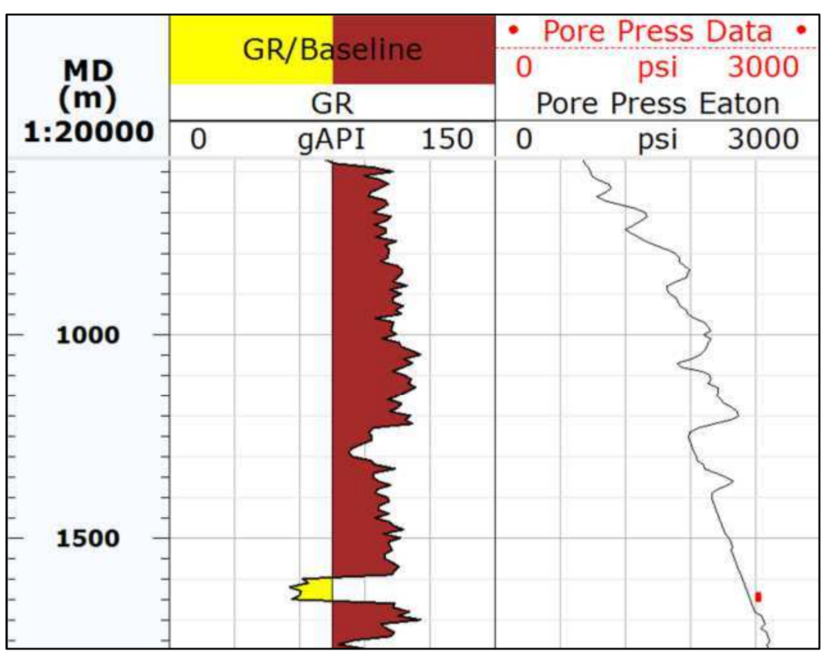

Figure 4.4 Comparison Eaton pore pressure vs field data well X-01.

4.2.2 Holbrook Pore Pressure

Holbrook method is one of the explicit pore pressure prediction techniques that has been implemented in this project. This method was introduced by Holbrook (1999) and used successfully in the North Sea to predict pore pressure in limestone, shaly limestone and sandstone intervals. It was also effectively utilized for pore pressure prediction in Deepwater Gulf of Mexico wells (Tutuncu et al. 2006). Unlike Eaton method, there is no normal trend line necessary for this method. The principle of this method is using the relationship between the porosity, mineralogy, and effective stress in granular sedimentary rocks.

The Holbrook method can be expressed in Equation 4.9.

$$\sigma_{eff} = \sigma_{max}\ x\ (1 - \emptyset)^{\beta} \tag{4.9}$$

and since Terzaghi effective stress law stated:

$$Pp = S_v - \alpha * \sigma_{eff} \tag{4.10}$$

Therefore,

$$Pp = S_v - \sigma_{max}\ x\ (1 - \emptyset)^{\beta} \tag{4.11}$$

where S_v is overburden stress, σ_{eff} is the effective stress required to reduce the mineral porosity to zero, σ_{max} is theoretical maximum vertical effective stress depends on the lithology, Ø is porosity from well logs, β is the compaction strain-hardening coefficient for the type of minerals.

The results of Holbrook pore pressure calculation for the study field is shown in Figure 4.5. Calculation was conducted on limited depth due to the availability of porosity log, the value of σ_{max} and β were taken from Table 4.1 based on the lithology at depth, with the exception of two points of depth, the pore pressure derived from this method indicated negative values.

Table 4.1 The Holbrook coefficients used to predict pore pressure (Holbrook, 1999)

Mineral	σ_{max}, psi	β	Hardness (m ohs)	Solubility (ppm)	Grain density (gr/cm3)
Quartz sand	130000	13.219	7	6	2.65
Average shale	18461	8.728	3	20	2.54-3.15
Calcite sand	12000	13	3	140	2.71
Anhydrite	1585	20	2.5	3000	2.87
Halite sand	85	31.909	2	350000	2.16

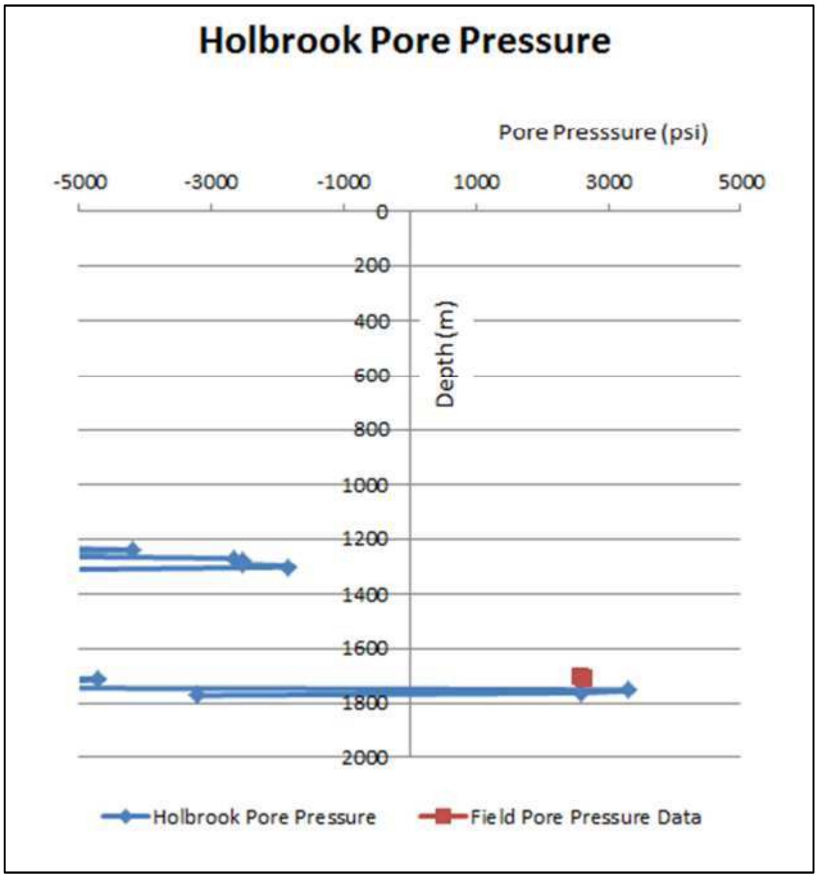

Figure 4.5 Holbrook pore pressure calculation.

Based on the results, it was concluded that Holbrook method is not suitable for this region. To use this method in this region, core measurements with different facies from the study area are required to customize and improve the power-law-compaction coefficients for more accurate pore prediction.

After reviewing the results from these two predictive methodologies, the pore pressure prediction in this field was obtained utilizing the Eaton model with 0.3 exponential coefficients. Eaton method also predicts the overpressure zone in the upper shale formation above the targeted reservoir. This knowledge is crucial for well drilling design.

4.3 Overpressure Zone

Most sedimentary formations do not have hydrostatic pore pressure. The presence of overpressure zone is important to predict accurately. When they are not accurately predicted before drilling, abnormal pressure zones can cause increasing drilling non-productive time and serious incidents in the drilling operation, such as well blowouts, pressure kicks, and fluid influx. In highly severe conditions, abnormally high pore pressures can lead to geologic disasters, such as mud volcano eruptions.

Several mechanisms can cause the overpressure in a formation. One of these mechanisms is the abnormal formation compaction (under-compaction). When sediments compact in a slow rate, there is equilibrium between increasing overburden and the reduction of pore fluid volume due to compaction, normal hydrostatic pressure generated in this condition. When overburden stress increase rapidly that leads to rapid burial, the sediments subside quickly and fluids only partially expelled from the pores. Due to the overburden pressure that the fluids have to support, the fluid pore pressure increases. This situation create overpressure zone in the formations. Figure 4.6 shows the determination of the depth of top under-compaction zone in Well X-01.

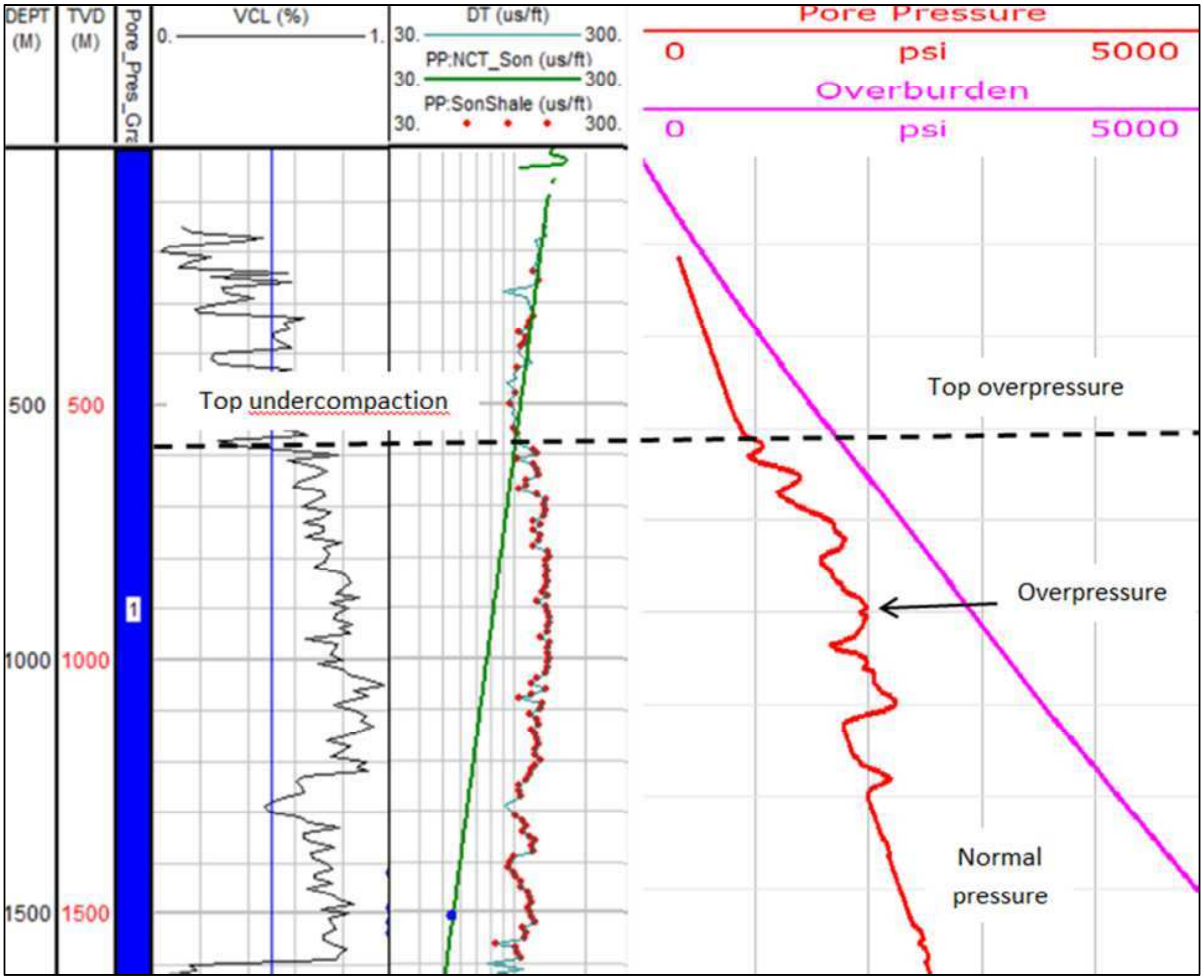

Figure 4.6 Top under-compaction zone.

In Field "X", overpressure zone is detected from the Eaton pore pressure prediction method (Figure 4.4). The fundamental theory for pore pressure prediction is based on Terzaghi's and Biot's effective stress law (Terzaghi et al. 1996 and Biot 1941), which indicates that pore pressure in the formation is a function of total stress (or overburden stress) and effective stress. When the overburden and effective vertical stresses are known, the pore pressure can be expressed in the following form:

$$P_p = \frac{(\sigma_v - \sigma_{eff})}{\alpha} \tag{4.12}$$

where P_p is pore pressure, α is Biot constant, σ_v is overburden stress, and σ_{eff} is effective stress. The effective stress is defined as the subtraction of pore pressure from overburden stress, as shown in Figure 4.7. The increase in overpressure causes reduction in the effective stress. Normally, the overpressure zone is found in deeper formations (more than 2000 m), however, in field "X" overpressure was detected at shallower depth, in 550 m.

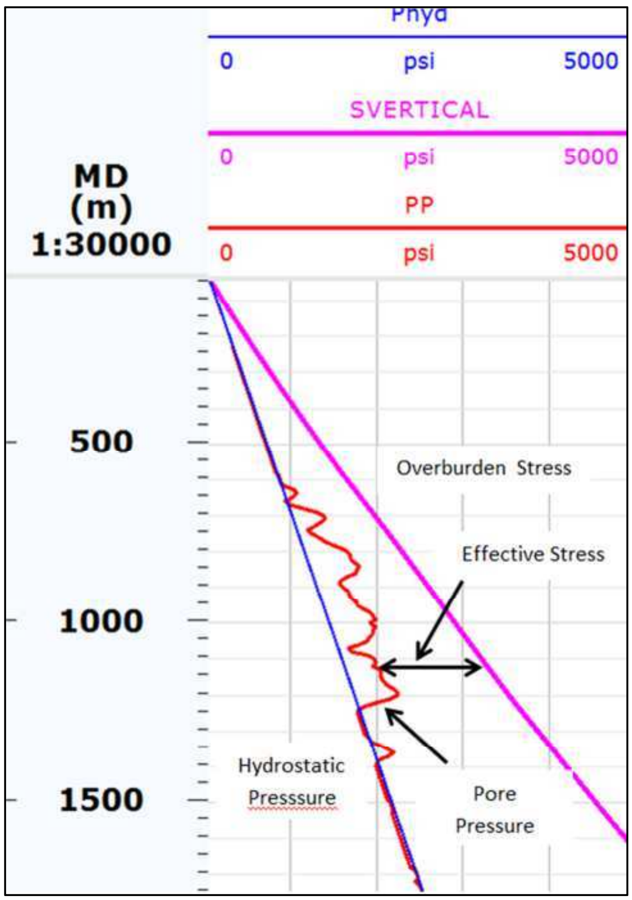

Figure 4.7 Effective stress Well X-01.

The pore pressure gradient in the study field for well design and to determine mud weight is shown in Figure 4.8. The mud weight should be able to support the wellbore walls for preventing influx and wellbore collapse during drilling. To avoid influx, mud weight should be set higher than the pore pressure predicted. However, the upper limit of the mud weight should not cause fracture in the formation, resulting mud losses or lost circulation. In the case of Well X-52 (Chapter 3), the mud weight is set higher to overcome the overpressure upper shale zone, but high mud weight caused loss circulation in the sandstone, below the upper shale zone. The mud losses due to loss circulation lead to BHA stuck and cause non-productive time.

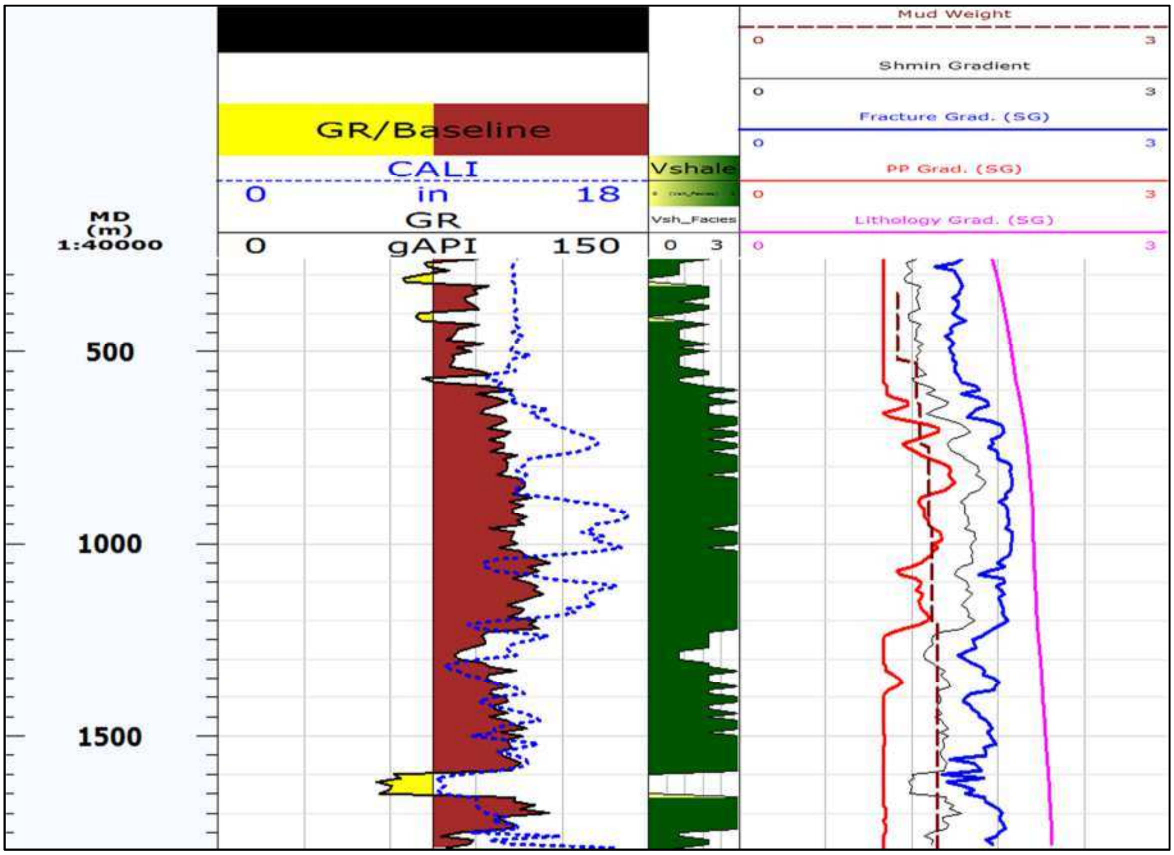

Figure 4.8 Pore pressure and fracture gradient Well X-01.

4.4 Formation Geomechanical Properties

Formation geomechanical properties such as Poisson’s ratio, Young’s modulus, tensile strength, uniaxial compressive strength (UCS), and friction angle, are important in conducting wellbore-stability analysis. They also have a role in determining the local formation stress regime, key information in wellbore stability analysis. The best way to gather the formation properties data are through combination of coupled laboratory experiments of geomechanics and acoustic velocities, permeability, porosity for calibration with the wireline and/or LWD/MWD log log data. However, since there is no cores were made available for this study, all parameters were obtained utilizing well-log data and appropriate empirical correlations. The methods of property determination are described in the subsequent sections.

4.4.1 Elastic Modulus

An elastic material can be represented using two elastic moduli. Depending on the stress state and type of input data is needed, measuring two of the moduli can provide all other moduli with the assumption of elastic material. Young's Modulus, E, is the relationship between axial stress and axial strain. The bulk modulus, K, is the stiffness under volume metric compression (hydrostatic stress state condition). Poisson's Ratio, v, is the proportional lateral expansion to axial shortening in a rock when a longitudinal stress is applied. Shear Modulus, G, provides information on how much the rock deforms in response under simple shear.

Deriving the dynamic elastic moduli from bulk density and dipole sonic logs (DSI) when the log data are available is not a very challenging task if the linear elastic rock assumption is used. P wave and shear wave velocity hold information about the elastic parameters, and the elastic moduli can be calculated using 4.13 through 4.17.

Dynamic Compressive Modulus (pressure units):

$$M = \frac{\rho}{{\Delta t_{co}}^2} \tag{4.13}$$

Dynamic shear modulus (pressure units):

$$G_s = \frac{\rho}{\Delta t_s{}^2} \quad (4.14)$$

Dynamic Bulk Modulus (pressure units):

$$K = M - \left(4\frac{G_s}{3}\right) \quad (4.15)$$

Dynamic Poisson's Ratio:

$$v = \frac{3K - 2G_s}{6K + 2G_s} \quad (4.16)$$

Dynamic Young's Modulus (pressure units):

$$E = \frac{9G_s K}{G_s + 3K} \quad (4.17)$$

In this study, only 7 out of 54 wells have compressional wave data, only two of them cover the depth of interest for this study. Numerous researchers have studied the relationship between compressional velocity (V_p) and shear velocity (V_s). Previous researchers (Mavko et al. 1998) concluded that the relationship between V_p and V_s for generally porous sedimentary rocks (such as sandstone, limestone, dolomite, shale, and mudstone), can be described by a linear correlation. Brocher (2005, 2008) studied thousands of V_p and V_s data obtained from various methods for a wide variety of lithologies and reported a conclusion of the V_p and V_s relationship in a nonlinear curve described in equations 4.18 and 4.19.

$$V_p = 0.9409 + 2.094V_s - 0.8206V_s{}^2 + 0.2683V_s{}^3 - 0.0251V_s{}^4 \quad (4.18)$$

or

$$V_s = 0.7858 - 1.2344V_p + 0.7949V_p{}^2 - 0.1238V_p{}^3 + 0.0061V_p{}^4 \quad (4.19)$$

These equations are valid for V_s between 0.3373 km/s and 5.0 km/s and V_p between 1.5 km/s and 8.5 km/s.

Several researchers came up with models for estimating compressional and shear velocities for the depths of interest when no compressional velocity logs are available. Brie (2001) developed a model for estimating compressional and shear velocities for a wide variety of lithology including shaly sand and carbonates. Eskandari et al. (2003) proposed the statistical approach of correlating a shear-wave velocity with some petrophysical parameters. They used five parameters (compressional velocity, neutron porosity, bulk density, gamma ray, and deep resistivity) in a multivariate model to obtain a shear-wave velocity. The correlation coefficient of this methodology was approximately 0.94. Rezaee et al. (2007) came up with another approach of shear-wave velocity prediction using fuzzy logic, neuro-fuzzy, and artificial neural network (ANN) techniques. They successfully utilized a back propagation ANN approach which takes input parameters in a network and computes a difference between a desired output and calculated one. Then, the error is back propagated to obtain the optimal weights. The training iterations stop when calculated and desired outputs are in a close proximity. They obtained good agreement between output data utilizing these three methodologies validating the feasibility of utilizing fuzzy logic, neuro-fuzzy, and ANN in shear-wave velocity prediction. However, the successes of all of these methods depend on the availability of other logs for the well, mainly porosity, bulk density, gamma ray, and deep resistivity logs. This is the biggest challenge for our study, since not only for every depth of interest there is no sonic log, but also there are no other logs available. Therefore, the input data needed at the depth of interest was obtained using compressional velocity logs where available.

Eissa and Kazi (1988) explained in their research results that the static elastic moduli are preferred over moduli obtained using dynamic approaches, based on the theory of the pseudo-static behavior of rock. The stress-strain relations for rocks are often non-linear, hence the ratio of stress to strain over a very small strain measurements is different from the ratio of stress to strain in a very large strain measurement (Tutuncu et al. 1998 a, b). The dynamic Young's Modulus is typically greater than static Young's Modulus, the dynamic Poisson's Ratio is typically lower than the static, and the ratio between the dynamic and static moduli approaches typically gets smaller as the confining pressure increases. The difference between the dynamic to static moduli typically increases in tight gas sands and in shale reservoirs. Therefore, for the best results many researches were done by correlating the static and dynamic moduli. Since there have been no core measurements to obtain the formation mechanical properties in this field, a review of the some static to dynamic modulus correlations was performed.

There are several reasons for the complexity of the relationship between the dynamic and static moduli: the first reason is since the elastic-wave velocity in a sample and the resulting dynamic elastic moduli depend on the condition of the measurement, mainly the effective pressure and pore fluid. Hence the frequency of the measurements will be different causing dispersion at high frequency measurements like in log measurements and ultrasonic core velocity measurements (Tutuncu, 2010 and Tutuncu et al. 1995, 1998a). The second reason is the static moduli depend on the detail of strain amplitudes applied during the triaxial experiment. The static Young's modulus is typically strongly affected by the overall stress state applied to the sample, as well as the measurement frequency and the strain amplitude of the measurement.

Presented below are several correlations published in the literature. The moduli are in GPa and the impedance is in km/s g/cc in these correlations. E_{stat} represents the static Young's modulus and E_{dyn} is the dynamic Young's modulus (Mavko, 2009).

Belikov (1970) correlation for microcline-granite:

$$E_{stat} = 1.137E_{dyn} - 9.685 \tag{4.20}$$

King (1983) correlation for igneous and metamorphic rocks from the Canadian Shield:

$$E_{stat} = 1.263E_{dyn} - 29.5 \tag{4.21}$$

McCann and Entwisle (1992) correlation for granites and Jurassic sediments in the UK:

$$E_{stat} = 0.69E_{dyn} + 6.4 \tag{4.22}$$

Eissa and Kazi (1988) correlation for a wide range of rock types:

$$E_{stat} = 0.74E_{dyn} - 0.82 \tag{4.23}$$

Gorjainov and Ljachowickij (1979) for equation for shallow clay samples:

$$E_{stat} = 0.033E_{dyn} + 0.0065 \tag{4.24}$$

and for sandy, wet soil:

$$E_{stat} = 0.061E_{dyn} + 0.00285 \tag{4.25}$$

Wang and Nur (2000) prepared a review article to summarize these relations for a variety of lithologies:

For soft rocks with the static Young's Modulus < 15 GPa, Wang and Nur (2000) defined E_{stat} in equation 4.26.

$$E_{stat} = 0.41E_{dyn} - 1.06 \tag{4.26}$$

and for hard rocks with the static Young's Modulus > 15 GPa:

$$E_{stat} = 1.153E_{dyn} - 15.2 \tag{4.27}$$

Mavko et al. (2009) reported the correlation from Mese and Dvorkin, which presented the relationship between the static Young's modulus and static Poisson's Ratio (v_{stat}) to the dynamic shear modulus calculated from the shear-wave velocity in shales and shaley sands given in equation 4.28.

$$E_{stat} = 0.59G_s - 0.34 \tag{4.28}$$

and

$$v_{stat} = -0.0208G_s + 0.37 \tag{4.29}$$

where G_s is the dynamic shear modulus:

$$G_s = \rho {V_s}^2 \tag{4.30}$$

and the relationship between the static moduli and the dynamic moduli is provided in equations 4.31 and 4.32.

$$E_{stat} = 0.29E_{dyn} - 1.1 \tag{4.31}$$

$$v_{stat} = -0.00743E_{dyn} + 0.34 \tag{4.32}$$

In this research study, the equations proposed by Mese and Dvorkin for shales and shaly sand, Eissa and Kazi, and Wang and Nur were used for the relationships between the dynamic and static moduli and the values obtained from sonic logs were converted to static moduli using these correlations based on the lithology at each depth. The results of dynamic to static conversion of Young's Modulus and Poisson's Ratio are shown in Figure 4.9.

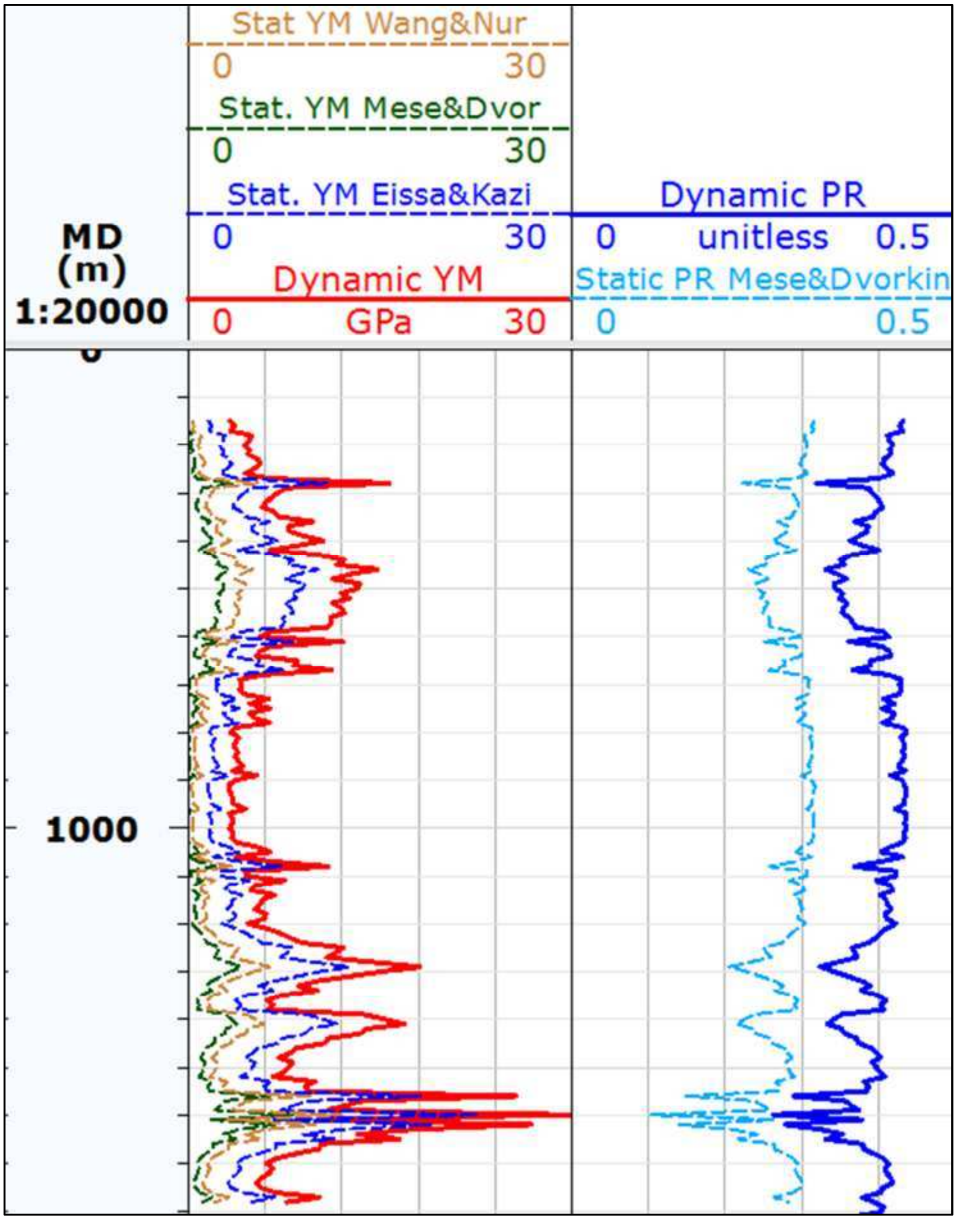

Figure 4.9 Dynamic to static elastic properties well X-01.

4.4.2 Unconfined Compressive Strength (UCS)

Unconfined Compressive Strength (UCS) is a critical parameter to obtain an appropriate rock-failure envelope for the formation and constrain the maximum horizontal stress magnitude.

The best prediction of UCS value comes from laboratory core measurements under uniaxial loading stress condition. The core samples are extracted from various lithologies along the wellbore, and the obtained UCS values are correlated to the different petrophysical and geomechanical characteristics. This correlations increase the accuracy of the well-log derived properties.

UCS correlations for specific regions, are not necessary applicable for another regions. However, correlations derived in the regions geographically close to the field of study or with similar tectonic history, stress regime, lithology, and petrophysical properties might be applicable to obtain initial constraints of UCS. There are also possibilities that the empirical values contain some error compared to the actual UCS. Extensive works for validation and calibration using laboratory measurement should be applied. In this study, since there are no core samples available, the UCS values are taken from existed empirical correlations from the literatures for similar lithology and petrophysical properties.

Zoback (2010) listed a number of correlations available for UCS calculation in sandstone, shale, and limestone formations. The lists for sandstone and shale formation are presented in Table 4.2 and 4.3. To empirically obtain UCS for this study, Equations 2 and 5 (for sandstone), and 17 (for shale) were utilized. Chang, Zoback, and Khaksar (2006) listed additional correlations for UCS calculations in sandstone and shale formation from various regions that could be used in this study.

For sandstone formation worldwide

$$\mathrm{UCS} = 2.28 + 4.1089 * E \tag{4.33}$$

For sedimentary formation worldwide

$$\mathrm{UCS} = 254 * (1 - 2.7 * \emptyset)^2 \tag{4.34}$$

For shale formation worldwide

$$\mathrm{UCS} = 1.35 * \left(\frac{304.8}{\Delta t_{co}}\right)^2 \tag{4.35}$$

For strong and compacted shale

$$\mathrm{UCS} = 7.22 * E^{0.712} \tag{4.36}$$

Table 4.2 UCS correlations for sandstone formations (Zoback, 2010)

Eq. No.	UCS, MPa	Region Where Developed	General Comments	Reference
1	$0.035\ V_p - 31.5$	Thuringia, Germany	-	(Freyburg 1972)
2	$1200\ exp(-0.036\Delta t)$	Bowen Basin, Australia	Fine grained, both consolidated and unconsolidated sandstones with wide porosity range	(McNally 1987)
3	$1.4138\times10^{7}\ \Delta t^{-3}$	Gulf Coast	Weak and unconsolidated sandstones	Unpublished
4	$3.3\times10^{-20}\ \rho^2 V_p^4\ [(1+\nu)/(1-\nu)]^2(1-2\nu)\ [1+0.78V_{clay}]$	Gulf Coast	Applicable to sandstones with UCS >30 MPa	(Fjaer, Holt et al. 1992)
5	$1.745\times10^{-9}\ \rho V_p^2 - 21$	Cook Inlet, Alaska	Coarse grained sands and conglomerates	(Moos, Zoback et al. 1999)
6	$42.1\ exp(1.9\times10^{-11}\ \rho V_p^2)$	Australia	Consolidated sandstones with $0.05<\phi<0.12$ and UCS>80MPa	Unpublished
7	$3.87\ exp(1.14\times10^{-10}\ \rho V_p^2)$	Gulf of Mexico	-	Unpublished
8	$46.2\ exp(0.000027E)$	-	-	Unpublished
9	$A\ (1-B\phi)^2$	Sedimentary basins worldwide	Very clean, well consolidated sandstones with $\phi<0.30$	(Vernik, Bruno et al. 1993)
10	$277\ exp(-10\phi)$	-	Sandstones with 2<UCS<360MPa and $0.002<\phi<0.33$	Unpublished

Table 4.3 UCS correlations for shale formations (Zoback, 2010)

	UCS, MPa	Region Where Developed	General Comments	Reference
11	$0.77\,(304.8/\Delta t)^{2.93}$	North Sea	Mostly high porosity Tertiary shales	(Horsrud 2001)
12	$0.43\,(304.8/\Delta t)^{3.2}$	Gulf of Mexico	Pliocene and younger	Unpublished
13	$1.35\,(304.8/\Delta t)^{2.6}$	Globally	-	Unpublished
14	$0.5\,(304.8/\Delta t)^{3}$	Gulf of Mexico	-	Unpublished
15	$10\,(304.8/\Delta t - 1)$	North Sea	Mostly high porosity Tertiary shales	(Lal 1999)
16	$0.0528\,E^{0.712}$	-	Strong and compacted shales	Unpublished
17	$1.001\phi^{-1.143}$	-	Low porosity (ϕ<0.1), high strength shales	(Lashkaripour and Dusseault 1993)
18	$2.922\,\phi^{-0.96}$	North Sea	Mostly high porosity Tertiary shales	(Horsrud 2001)
19	$0.286\,\phi^{-1.762}$	-	High porosity (ϕ>0.27) shales	Unpublished

The calculated UCS were used in the wellbore stability models and validated by the available field data. In the future, the UCS should be checked through the quality control process by measuring the actual UCS values in the geomechanics laboratory if core samples are made available.

4.4.3 Tensile Strength

Tensile strength of rock is one of the key parameters in calculating and constraining the minimum and maximum horizontal stresses. For unconsolidated formations, the tensile strength is typically assumed to be zero, based on the disturbance of an intact condition of rock by bit penetration. This assumption will not be true in the highly compacted and strength formations under high in-situ stresses.

The best way to obtain tensile strength data is by conducting laboratory core measurements. However, in the absence of core data such as this study, the tensile strength is usually estimated at 10-12% of the UCS for all facies. This approach might be incorrect because tensile strength is typically impacted by the lithology type, compaction level, lamination orientation, and presence of microcracks (Hobbs, 1964).

4.4.4 Internal Friction Angle and Friction Coefficient

Internal friction angle (Φ) is a measure of the ability of a unit of rock to withstand a shear stress. Rock formation, even the weak one, can have a high friction angle. The best way to obtain the value of friction angle is when a uniaxial compressive strength test is conducted. In a case with no core measurements available, friction angle is obtained from available empirical correlations. Zoback (2010) reported empirical correlations for shales and shaly sedimentary formations, which are used in this study.

For shaly sedimentary rock with 60<GR<120

$$\Phi = 70 - 0.417 * GR \tag{4.37}$$

For shale

$$\Phi = \tan^{-1}\left(\frac{78 - 0.4 * GR}{60}\right) \tag{4.38}$$

where internal friction angle (Φ) is in degrees, and gamma ray (GR) is in gAPI.

Friction coefficient is calculated by using following equation:

$$\mu_i = \frac{1 + \sin \Phi}{1 - \sin \Phi} \tag{4.39}$$

As reported by Peng and Zhang (2007), Weingarten and Perkins in 1992 presented the correlation to predict sandstone internal friction angle using porosity as follows:

$$\Phi = 57.8 - 105\phi \tag{4.40}$$

where internal friction angle (Φ) is in degrees, and porosity ($\emptyset$) is in fraction.

For this study, the correlation reported by Zoback for shale and Weingarten and Perkins for sandstone were used to obtain the internal friction angle.

A histogram for the calculated coefficient of internal friction is illustrated in Figure 4.10, and the correlation between log-derived internal friction angle and shale volume is presented in Figure 4.11.

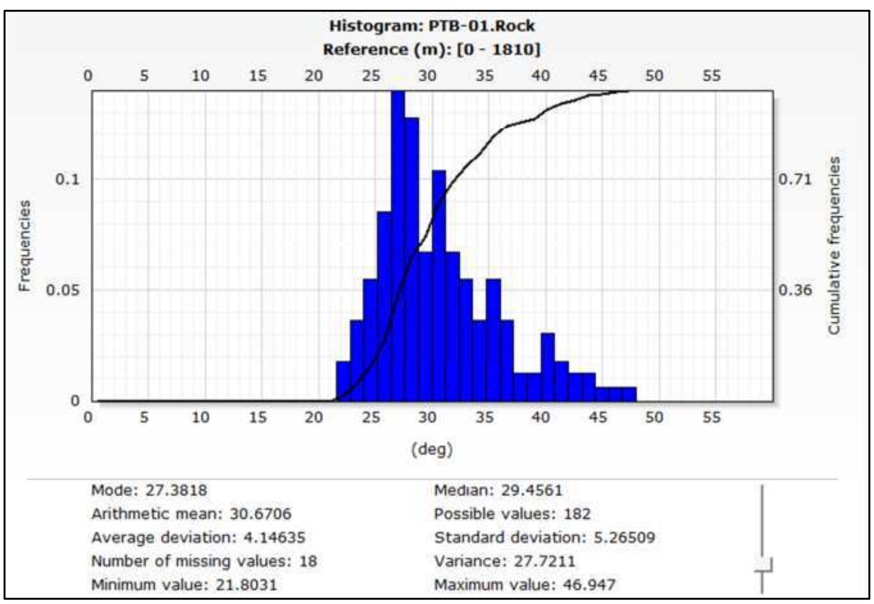

Figure 4.10 Histogram of the log-derived internal friction angle values.

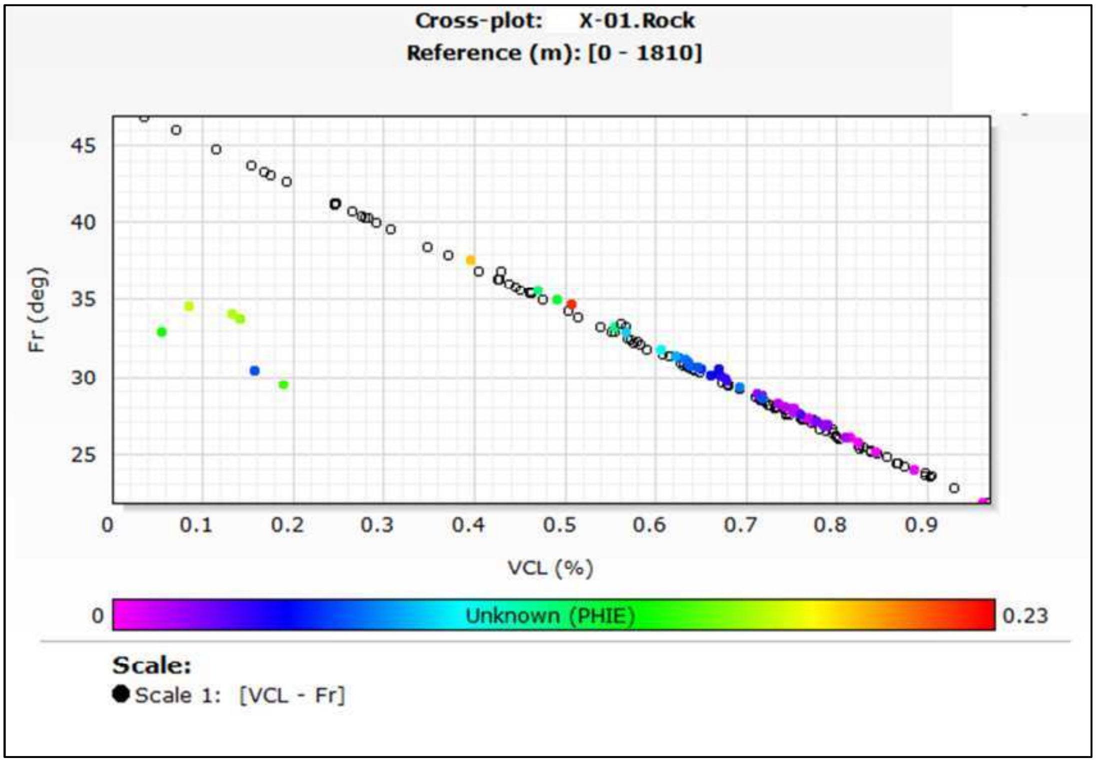

Figure 4.11 Correlation between log-derived internal friction angle, Vcl, and porosity.

4.4.5 Biot Coefficient

Biot's coefficient (α) is a measure of how well grains in the rocks are connected with each other. The amount of contact cements between the grains determines the stiffness of rocks. It also helps determining the effect of pore pressure on the effective stresses.

There are many empirical relations for Biot's coefficient, most of them mainly through porosity. Wu (2001) presented the correlation for consolidated sediments as follows:

$$\alpha = 1 - (1 - \emptyset)^{3.8} \tag{4.41}$$

Krief (1990) presented similar correlation from his experiment for dry rock as follows:

$$\alpha = 1 - (1 - \emptyset)^{\left(\frac{3}{1-\emptyset}\right)} \tag{4.42}$$

Lee (2002) proposed the correlation for unconsolidated sediments, described as:

$$\alpha = \frac{-184.05}{1 + exp\left(\frac{\emptyset + 0.5646}{0.09425}\right)} + 0.99494 \tag{4.43}$$

For this study, the correlation for consolidated sediments was used to calculate the Biot coefficient.

4.4.6 Orientations of the Principle Horizontal Stresses

Orientations of the principle horizontal stresses are important factors that affect the wellbore stability. Breakouts on the wellbore indicate the azimuth of the principle stresses, it happens when the hoop stress is the most compressive at the direction of the minimum horizontal stress and when the stress concentration exceeds the rock strength. The circumferential stress has the least compression at the orientation of the maximum principle horizontal stress, causing the drilling-induced fractures (Barton et al. 2002). Therefore, FMI log data typically used to determine the orientation of principle horizontal stresses. There are other tools to determine the stress orientation among which 4-arm/6-arm caliper logs, fast shear azimuth from shear sonic in cross-dipole mode are among a few.

One method to determine the azimuth of horizontal stresses when there is no wireline measurement available is to use the world stress map. The World Stress Map (WSM) is the global compilation of information on the present-day stress field of the Earth's crust with 21,750 stress data records in its current database released in 2008 (Heidbach, 2010). More than 7300 in situ stress orientations have been compiled as part of the WSM project. The data of stress orientations came from in situ stress measurements and geologic observations made in the upper

1–2 km, well bore breakouts extending to 4–5 km depth and earthquake focal mechanisms to depths of ∼20 km.

In this study, we used world stress map data to determine the orientation of horizontal stresses, the regional stress map can be described as follows:

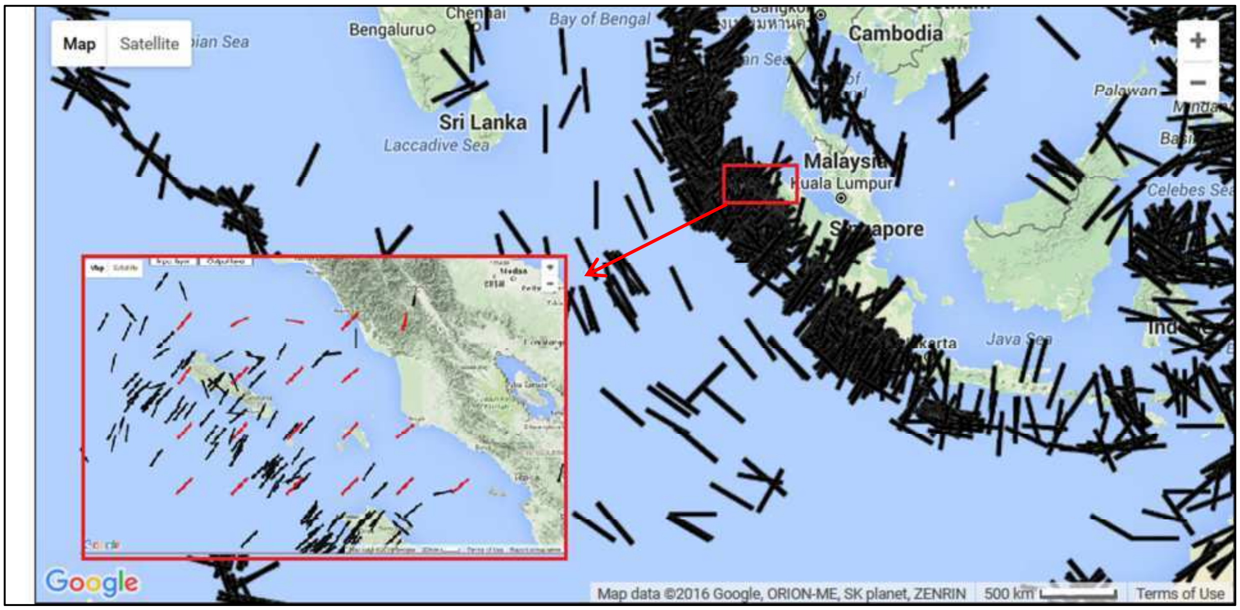

Figure 4.12 Regional stress map.

Since the regional stress map indicates relatively consistent stress orientation, this method is considered adequate to determine horizontal stress azimuth in the study field. The Rosette diagram for this map is as follows:

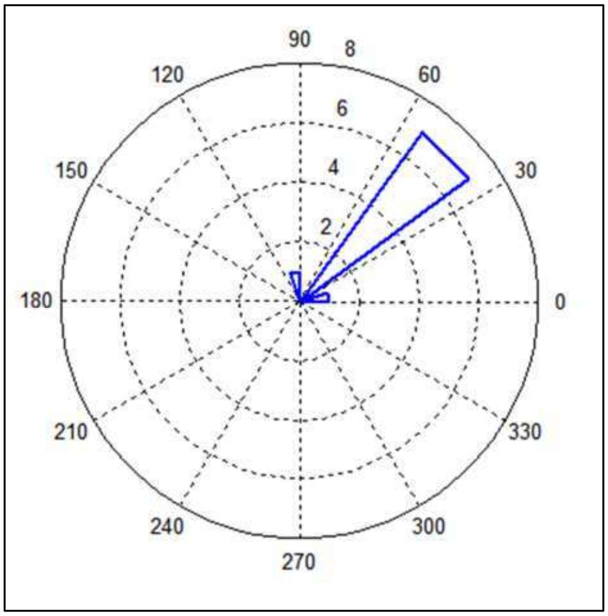

Figure 4.13 Rosette diagram for horizontal stress azimuth.

Based on the Rosette diagram, the azimuth of maximum horizontal stress in this field is ± 45^{o} clockwise from the North.

4.4.7 The Magnitude of Horizontal Stresses

The magnitude of minimum horizontal stress is important to determine the stress regime. The most accurate value of the minimum horizontal stress is obtained from the Extended Leak-off Tests (XLOT) or minifrac test determining the fracture closure pressure. The pressure required to propagate the fracture will be equal to or greater than the minimum principle stress magnitude at the depth of interest. The fracture will close as soon as the pressure drops below the stress acting normal to the fracture, which is the minimum principle stress.

In this research case study, there is only one hydraulic fracturing data available, which is for well X-27 at 1675 m. From the test data, the closure pressure at that depth is measured at 3600 psi.

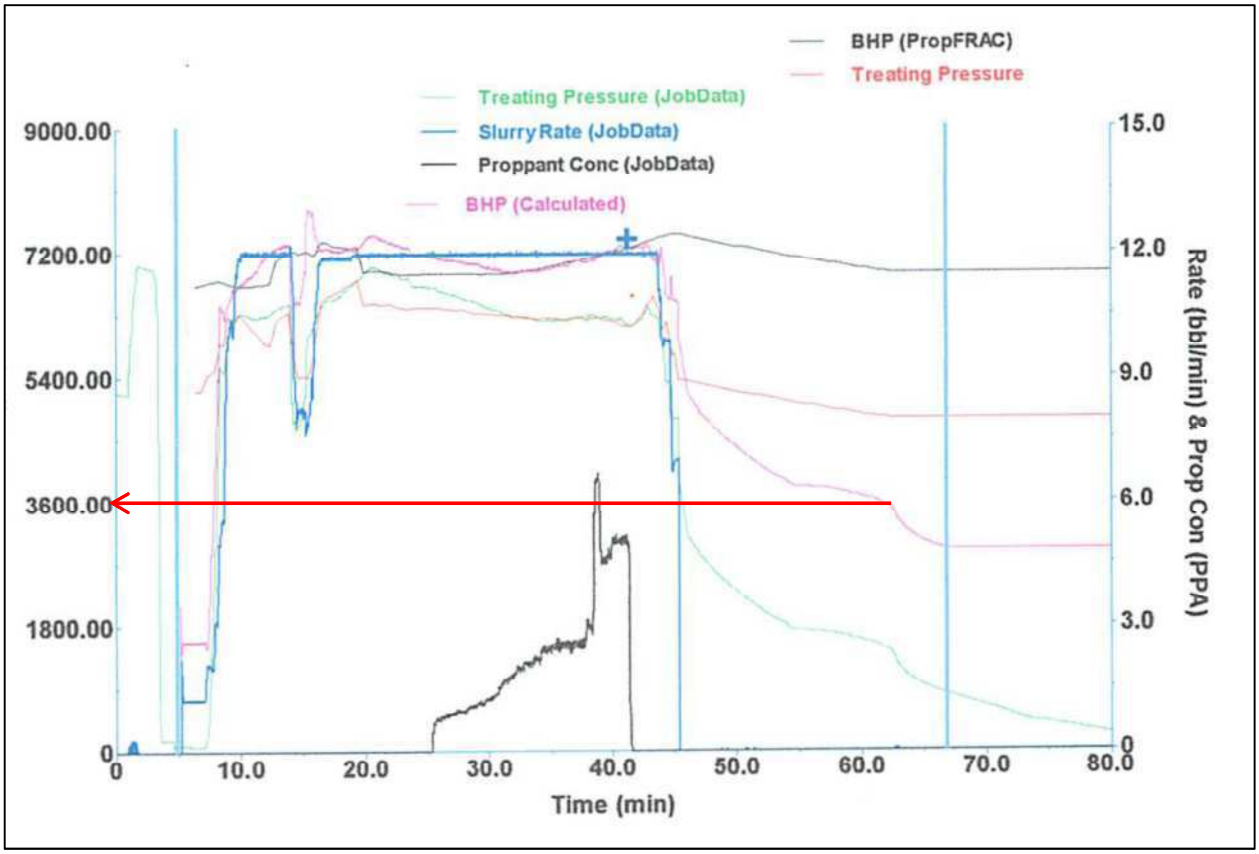

Figure 4.14 Hydraulic fracturing data well X-27.

Unfortunately, since there are no other logs available for well X-27, the closure pressure data from this well could not be tied into formation properties to help calibrating the calculation of minimum horizontal stresses using empirical calculation. Mitchell (1995) used Eaton method to derive the correlation for minimum horizontal stress, the equation is as follows:

$$\sigma_{hmin} = \left(\frac{v}{1-v}\right)\left(\sigma_v - \alpha * P_p\right) + \alpha * P_p + T_s \tag{4.44}$$

where v is Poisson's ratio, α is Biot's coefficient, σ_v is overburden stress (psi), P_p is pore pressure (psi), and T_s is rock tensile strength (psi).

To constrain the magnitude of the σ_H using wellbore tensile fractures:

$$\sigma_{Hmax} = 3 * \sigma_{hmin} - 2 * P_p - \Delta P - T_s \tag{4.45}$$

where ΔP is the difference between drilling Equivalent Circulating Density (ECD) and pore pressure in psi.

Using elasticity theory and Mohr-Coulomb failure criterion, Addis et al. (1996) presented the relationship between horizontal stress and pore pressure as follows:

For normal faulting:

$$\sigma_H = \frac{2v}{1 - sin\Phi}\left(\sigma_h - P_p\right) + P_p \tag{4.46}$$

For strike slip faulting:

$$\sigma_H = \frac{1}{v\left(q_f + 1\right)}\left(q_f\sigma_h - P_p\left(q_f(1 - v\right) - v\right) \tag{4.47}$$

With

$$q_f = \frac{1 + \sin\Phi}{1 - sin\Phi} \tag{4.48}$$

where Φ is internal friction angle and P_p is pore pressure.

4.4.8 Derived Stress Regime

From the Figure 4.15, it is evident that the stress regime in the entire interval is in the strike slip fault regime (S_H>S_v>S_h). This is not in accordance with the geological map that shows that Well X-01 is located in between of reverse faults. However, the strike slip stress regime is consistent with the dominantly strike-slip earthquake focal mechanism in the region.

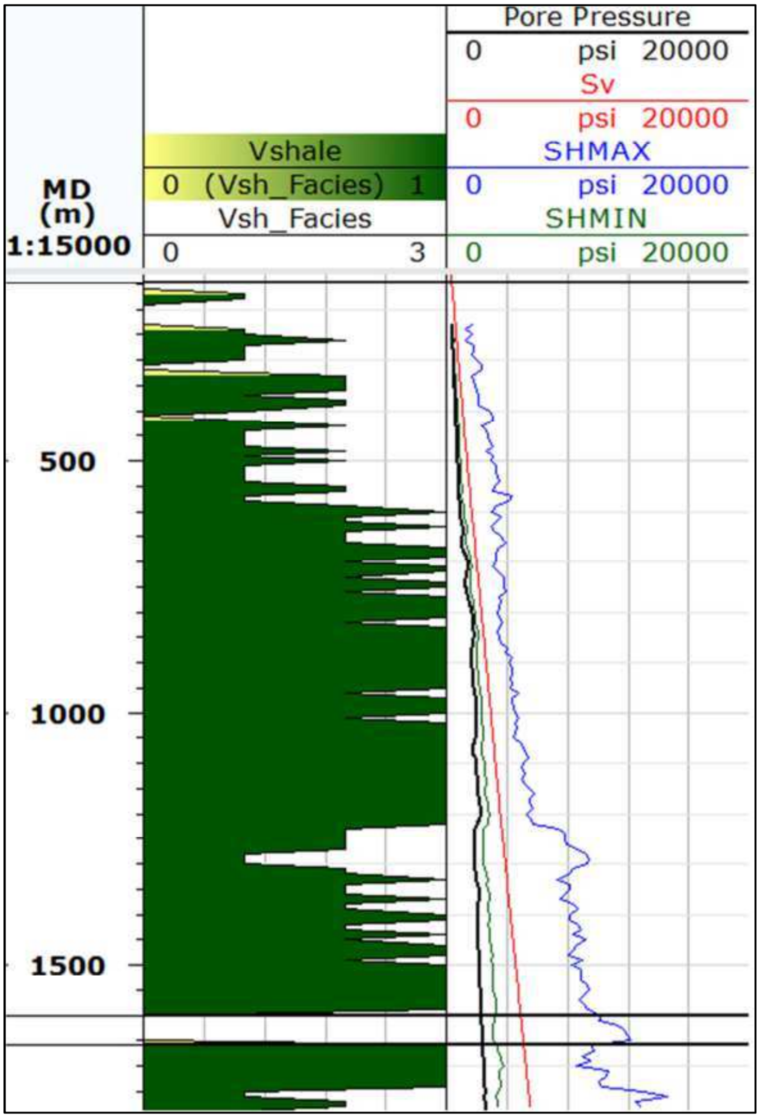

Figure 4.15 Magnitude of pore pressure and principle stresses as a function of depth Well X-01.

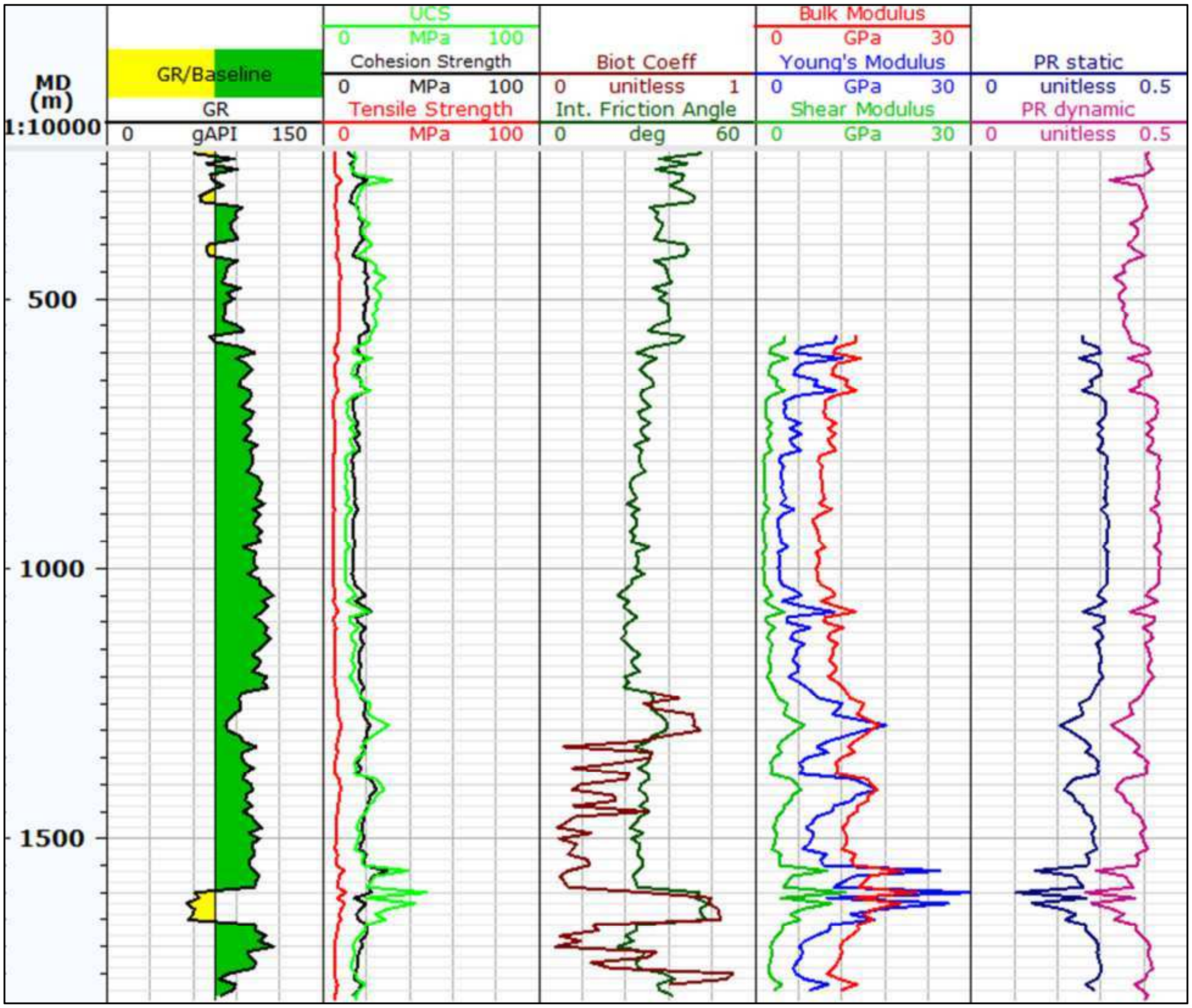

Figure 4.16 Rock elastic properties Well X-01.

CHAPTER 5

NUMERICAL MODEL FOR WELLBORE STABILITY

The numerical model for stress alteration around the wellbore has been described in Chapter 3, including the effects of chemical interaction, temperature alteration, and flow induced stress. The equations are as follows:

$$\sigma_r = \Delta p_w$$

$$\sigma_\theta = \left(\sigma_x + \sigma_y - \Delta p_w\right) - 2\left(\sigma_x - \sigma_y\right)\cos 2\theta$$

$$- 4v\tau_{xy}\sin 2\theta + \alpha\frac{1-2v}{1-v}\Delta\Pi + \frac{\alpha_m * E * (T - T_o)}{1-v} - (1$$

$$- \alpha)\frac{1-2v}{1-v}(P_w - P_o)$$

$$\sigma_z = \sigma_{zz} - 2v\left(\sigma_x - \sigma_y\right)\cos 2\theta$$

$$- 4v\tau_{xy}\sin 2\theta\alpha\frac{1-2v}{1-v}\Delta\Pi + \frac{\alpha_m * E * (T - T_o)}{1-v}$$

$$- (1-\alpha)\frac{1-2v}{1-v}(P_w - P_o)$$

$$\tau_{r\theta} = \tau_{rz} = 0$$

$$\tau_{\theta z} = 2\left(\tau_{yz}\cos\theta - \tau_{xz}\sin\theta\right) \tag{5.1}$$

5.1 Sensitivity Analysis

Sensitivity analysis was conducted due to the uncertainties involved in the determination of wellbore stability model input data. Sensitivity analysis was conducted with the @RISK

Excel, a program that provided calculation of the risk severity using Monte Carlo simulations to show probabilities of specific input parameters. For each input parameter, probable ranges are determined by considering variations of input data as described in Table 5.1.

Table 5.1 Input data ranges for the wellbore-stability sensitivity analysis

PARAMETERS	Min	Most Likely	Max	Case 1	Case 2
Pore Pressure, MPa	2.26	10.97	17.56	6.99	8.20
Drilling ECD, MPa	15.86	17.24	24.83	16.00	16.25
Static Poisson's ratio	0.26	0.39	0.44	0.32	0.39
Static Young's modulus, GPa	3.15	8.06	31.80	10.30	8.57
UCS, MPa	1.43	6.08	40.36	17.90	20.00
Tensile strength, MPa	0.15	1.48	3.44	1.80	2.00
Friction angle, deg	21.80	27.38	46.90	31.30	31.00
Cohesion, MPa	Calculated from UCS and friction angle				
OBS, MPa	0.69	18.58	39.43	12.43	15.00
Shmin, MPa	2.54	16.26	25.75	8.74	9.20
SHmax, MPa	8.32	39.00	44.83	18.00	21.30
Biot's coefficent	0.05	0.26	0.82	0.12	0.12
Aw_fl	0.65	0.90	0.95	0.90	0.90
Aw_sh	0.90	0.95	0.98	0.95	0.95
Membrane efficiency	0.00		0.10	0.10	0.10
alfa_m, C-1	0.00		0.00	0.00	0.00
T, °C	60.00	65.00	75.00	65.00	65.00
To, °C	83.00	85.00	87.00	85.00	85.00

The probability densities and identifying P10 and P90 values are simulated using @RISK Excel to determine the key controlling factors under the given uncertainties in order to prevent breakouts and fracture pressures. The results of probability density simulations are shown in Figure 5.1 and 5.2. For breakout prevention, the P10 value was calculated to be 15.16 MPa, and the P90 value is 28.75 MPa. This program also simulates the probability densities for the critical pressure, beyond which wellbore fracture would occur. The P10 value is 61.4 MPa and the P90 value is 111.3 MPa, which means there is 10% probabilities for the wellbore pressure will be less than 63 MPa, and 90% probability that the critical pressure will be less than 112 MPa.

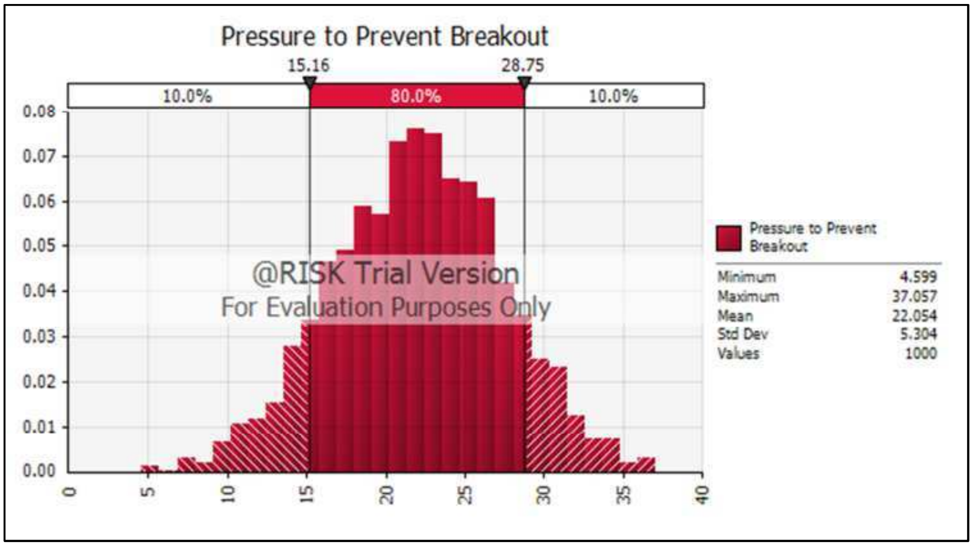

Figure 5.1 Probability density of the pressure to prevent the wellbore collapse.

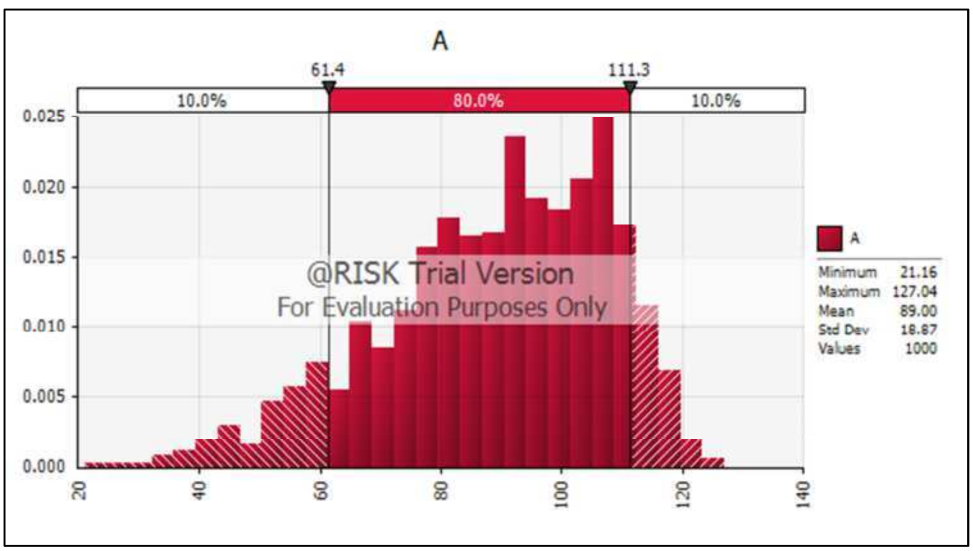

Figure 5.2 Probability density of the critical fracture pressure.

The density charts show the level of confidence of the probability for particular values of mud weight to prevent breakouts or critical pressure for tensile fracture. However, it is still necessary to evaluate the sensitivity of the output data to see the dominant parameters affecting the wellbore breakouts. In Figure 5.3, a tornado chart shows that the most dominant parameters affecting the required minimum mud weight to prevent wellbore breakouts are horizontal stresses, friction angle, pore pressure, and UCS. Figure 5.4 shows the parameters that are dominant in determining the critical fracture pressure in this well, those are horizontal stresses, friction angle, UCS, pore pressure and overburden stress. The impact of chemical, temperature alteration, and flow induced stress in wellbore breakout and tensile failure is very small and did not show up in the tornado chart. The effect of overburden pressure was also indicated insignificant in this case. Based on this sensitive analysis, emphasis in input data acquisition has been given in this study and should be continued to be paid attention in the future studies for reliable geomechanical data and in situ principle stresses.

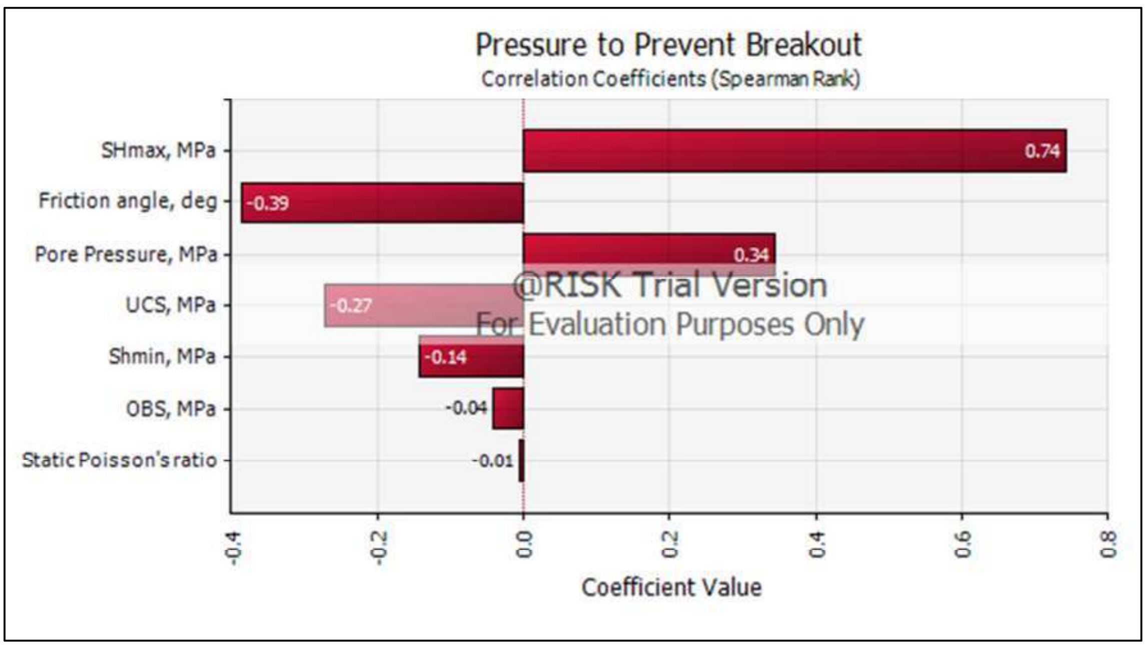

Figure 5.3 Contribution of various input parameters to minimum pressure to prevent breakouts.

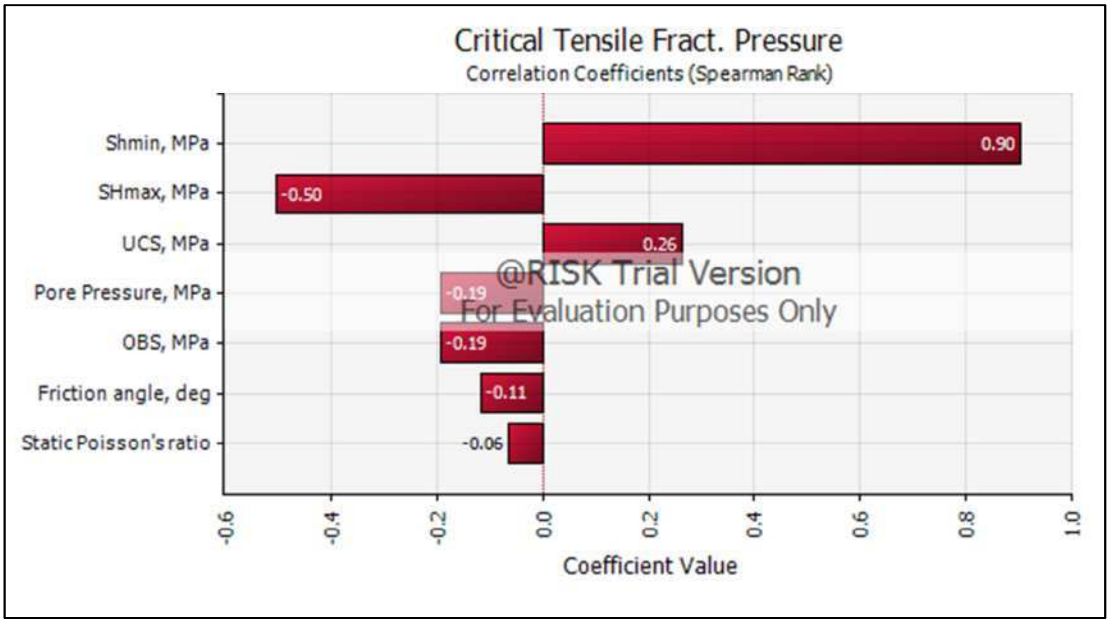

Figure 5.4 Contribution of the various input parameters to critical wellbore fracturing pressure.

5.2 Numerical Model Results and Discussion

The numerical model was written using MATLAB programming software to evaluate the critical mud weights to prevent breakouts and tensile fractures in vertical and arbitrarily oriented wellbores. The Mohr-Coulomb and Mogi-Coulomb failure criteria have been utilized in the numerical model. Two cases from different depths from intervals of interest were selected to represent the instability problems in this field. Case 1 represents the in-gauge hole with no wellbore stability above the problematic upper shale formation, the input data for this case are presented in Table 5.2. Case 2 corresponds to the upper shale formation where wellbore breakouts are detected in many wells using input data in Table 5.3. All cases occur in shale formation with varieties of in situ principle stresses, lithology, and geomechanical properties. The results of the numerical modeling are the critical mud weight to avoid wellbore breakout and tensile failure for a wellbore that is drilled in arbitrary inclination and azimuth. The results for Cases 1 and 2 are presented in Figures 5.5 and 5.6, respectively.

In all cases, the required mud weight to avoid wellbore breakouts from Mohr-Coulomb method is higher than the calculated mud weight using Mogi-Coulomb method (by approximately 0.2 SG). Mogi-Coulomb method considers the effects of intermediate stress that is the reason for the difference.

Table 5.2 Input data for Case 1

TVD, m	430
Lithology	Shale
Rock tensile strength, MPa	1.80
Uniaxial compressive strength, MPa	17.90
Young's modulus, GPa	10.30
Poisson's ratio, unitless	0.35
Biot's coefficient, unitless	0.12
Internal friction angle, deg	31.30
Overburden stress, MPa	12.43
Minimum horizontal stress, MPa	8.74
Maximum horizontal stress, MPa	18.00
Azimuth of max. horizontal stress, deg	45.00
Pore pressure, MPa	6.99
Thermal expansion coefficient, C-1	0.00
Membrane efficiency, unitless	0.10
Chemical activity of shale pore water	0.95
Chemical activity of drilling fluids	0.90
Formation temperature, °C	85.00

The results shown in Figures 5.5-5.8 show that it is recommended to drill deviated wells in the direction ±30 degrees from the direction of maximum horizontal stress with less possibilities of wellbore breakout. Wellbore inclination at the interval of interest should be above 60 degrees to avoid using high mud weights.

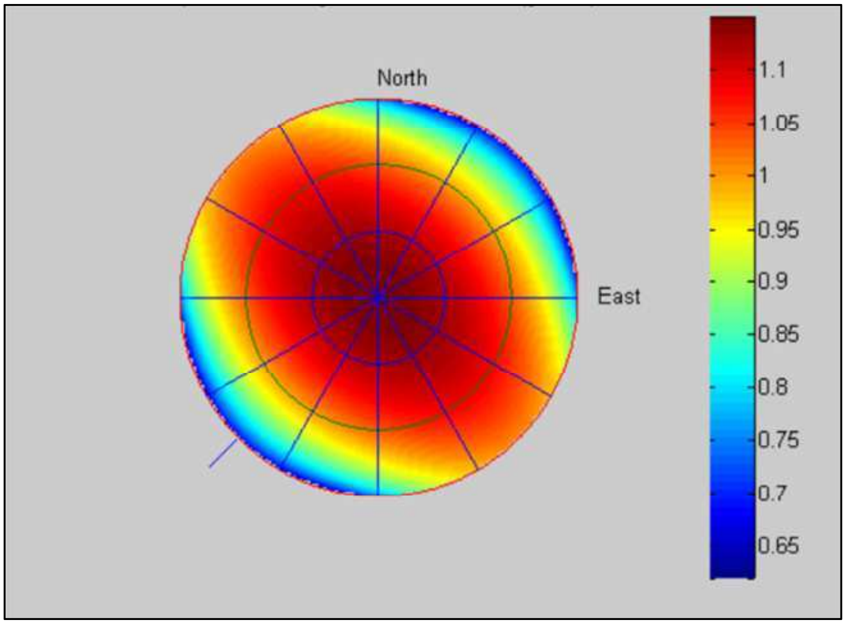

Figure 5.5 Required mud weight to prevent wellbore breakout for Case 1 utilizing Mohr-Coulomb failure criterion, colorbar indicates mud weight in SG.

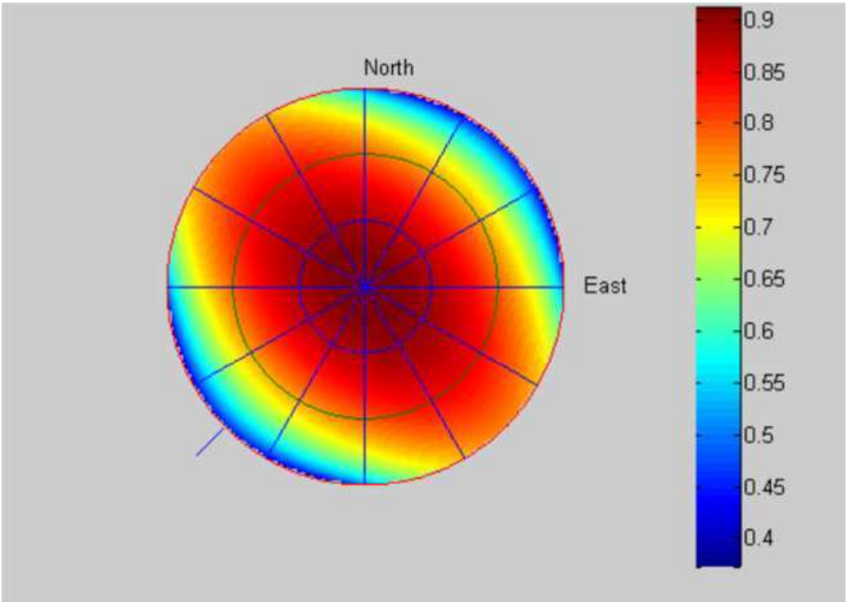

Figure 5.6 Required mud weight to prevent wellbore breakout for Case 1 utilizing Mogi-Coulomb failure criterion, colorbar indicates mud weight in SG.

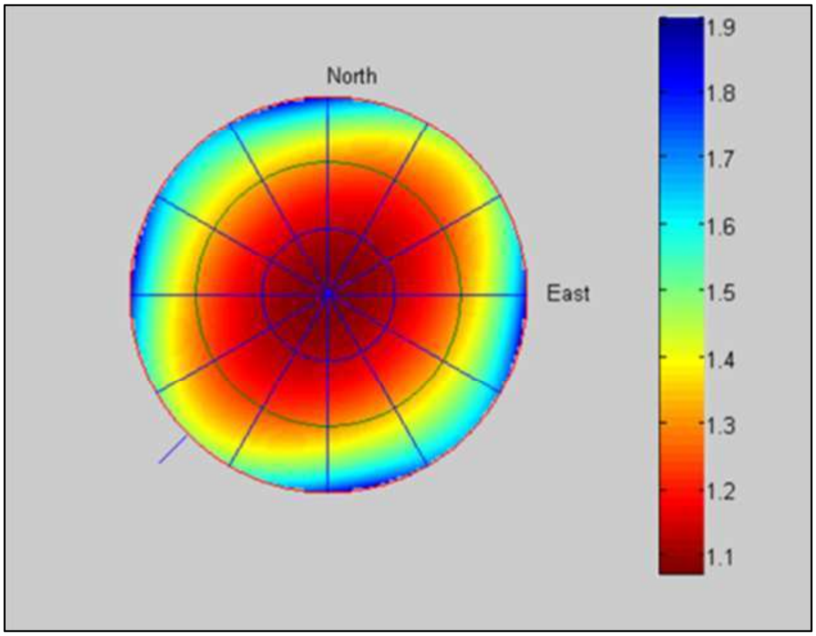

Figure 5.7 Maximum mud weight before wellbore fracturing for Case 1, colorbar indicates mud weight in SG.

Table 5.3 Input data for Case 2

TVD, m	650
Lithology	Shale
Rock tensile strength, MPa	2.00
Uniaxial compressive strength, MPa	20.00
Young's modulus, GPa	8.57
Poisson's ratio, unitless	0.39
Biot's coefficient, unitless	0.12
Internal friction angle, deg	31.00
Overburden stress, MPa	15.00
Minimum horizontal stress, MPa	9.20
Maximum horizontal stress, MPa	21.30
Azimuth of max. horizontal stress, deg	45.00
Pore pressure, MPa	8.20
Thermal expansion coefficient, C-1	0.00
Membrane efficiency, unitless	0.10
Chemical activity of shale pore water	0.95
Chemical activity of drilling fluids	0.90
Formation temperature, °C	85.00

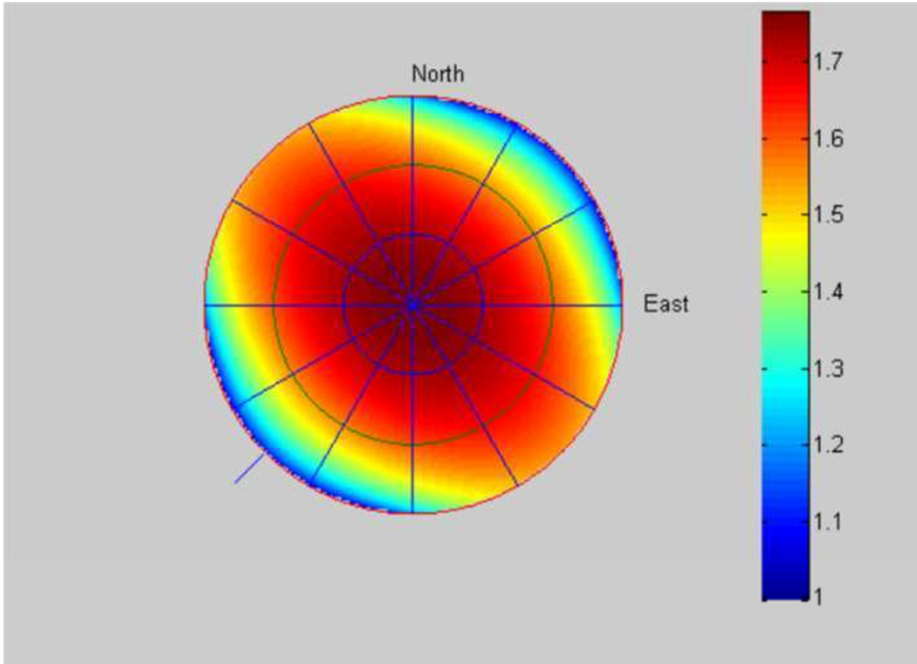

Figure 5.8 Required mud weight to prevent wellbore breakout for Case 2 utilizing Mohr-Coulomb failure criterion, colorbar indicates mud weight in SG.

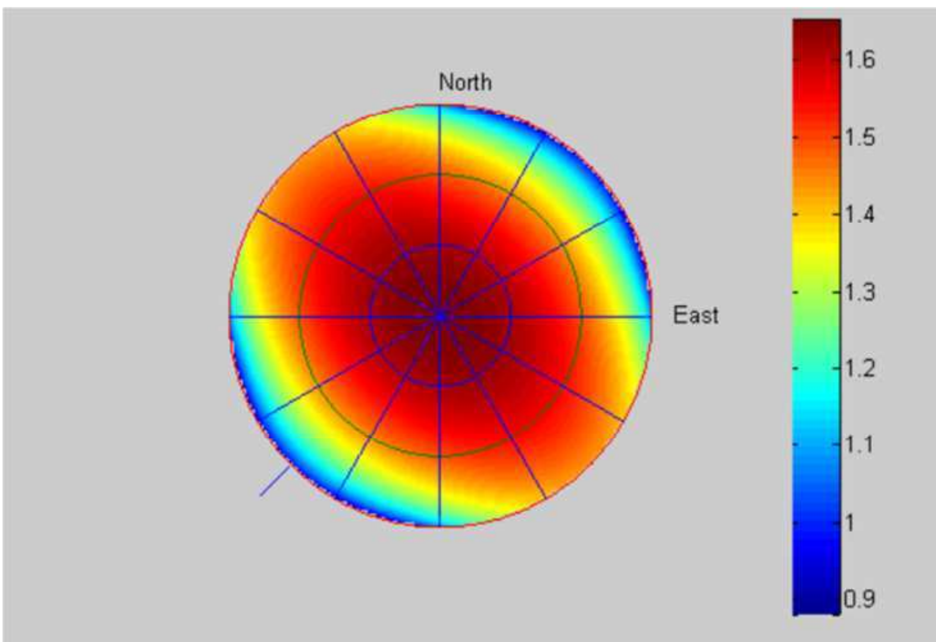

Figure 5.9 Required mud weight to prevent wellbore breakout for Case 2 utilizing Mogi-Coulomb failure criterion, colorbar indicates mud weight in SG.

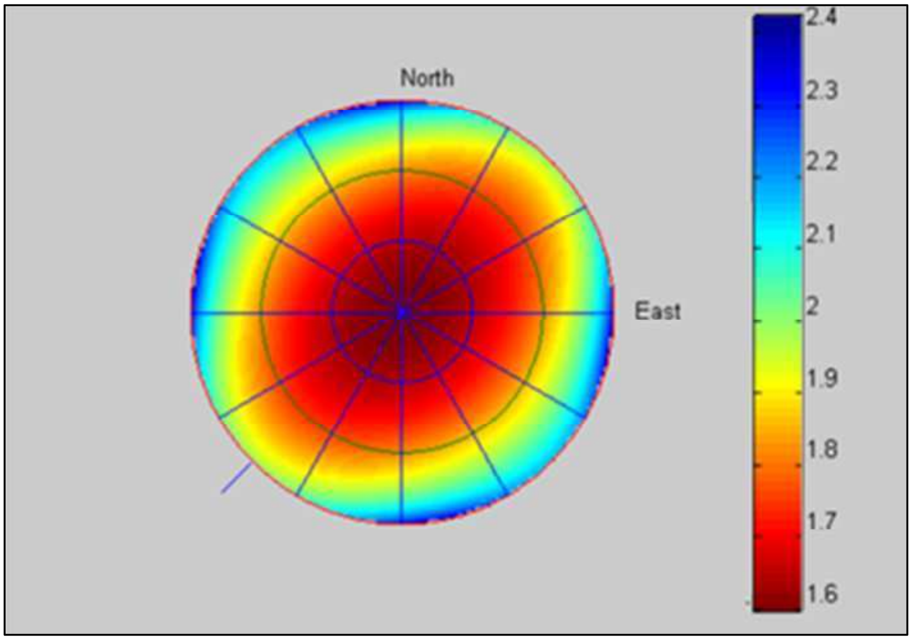

Figure 5.10 Maximum mud weight before wellbore fracturing for Case 2, colorbar indicates mud weight in SG.

The results of numerical modeling are presented in lower hemisphere diagrams (Figure 5.5-5.10), where each point in the diagram represents a well with any given azimuth and deviation. A point at the center of the diagram corresponds to vertical well, while horizontal wells are located on the periphery of the diagram at the appropriate azimuth and radial distance.

In the wellbore breakout model, the color shown represents the mud weight required to prevent wellbore breakout, with red colors as the relatively unstable well orientations as higher mud weight is needed to prevent breakout. The results show that the vertical wells are the most likely to fail, while horizontal wells drilled parallel to the azimuth of S_{Hmax} are the most stable. Therefore, the mud weight needed to prevent wellbore breakout in deviated wells is lower compared to the mud weight for vertical wells.

In the tensile fracture model, the color represents the maximum mud weight before tensile fractures take place. Dark blue colors mean that higher mud weight is needed to induce tensile fracture of the wellbore wall. The results for both cases show that in vertical wells, the tensile fracture will occurs in wellbore pressure only slightly higher than the pore pressure, while in deviated wellbore the tensile fracture will only form at correspondingly higher mud weights.

5.3 The Effects of Mud Properties

Composition and properties of drilling fluids play an important role in maintaining the wellbore stability during drilling activity. Unfortunately, there is little information available on the mud properties used in this field to study their effects on wellbore instabilities. A document was found in drilling reports of Well X-53 implied that there was incompatibility between the real properties of drilling fluids provided with the required properties, which could be the cause of instability issues.

Other information available on mud properties is the type of drilling fluid used for Well X-51, X-52, and X-53, which is oil based mud. The intention of using oil based mud in this field was to handle on troublesome shales that would otherwise swell and disperse in water based mud. However, this choice might have helped the loss circulation after tensile fracture occurred, like what happened in Well X-53. Cook et al. (2012) explained how the type of drilling mud affects the fracture propagation that causes lost circulation. When fracture growth begins, the wellbore loses drilling fluid into the fracture. If the fluid contains Loss Circulation Material (LCM), it will isolate or screen the fracture tip from the fluid pressure of invading mud. An example of this LCM is the mud cake that is created by water based mud. In a system using oil based mud, the internal filter cake allows for full pressure communication to the tip which extends the fracture (Figure 5.11 and 5.12), hence allows further lost circulation.

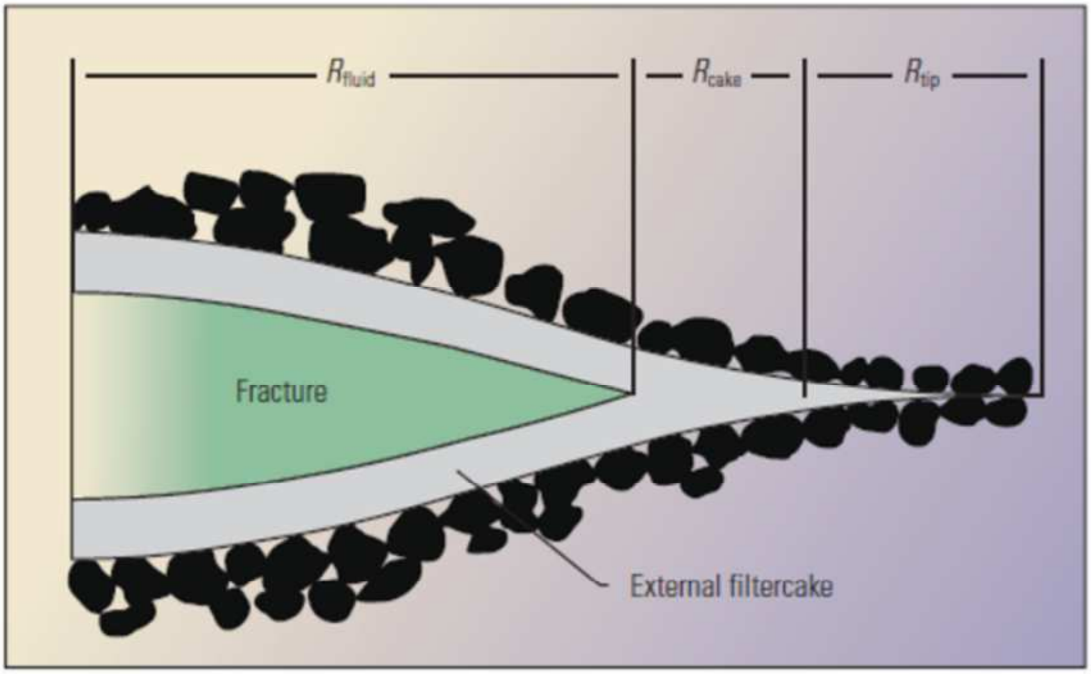

Figure 5.11 Filter cake and fracture propagation in Water Based Mud system (Cook et al. 2012).

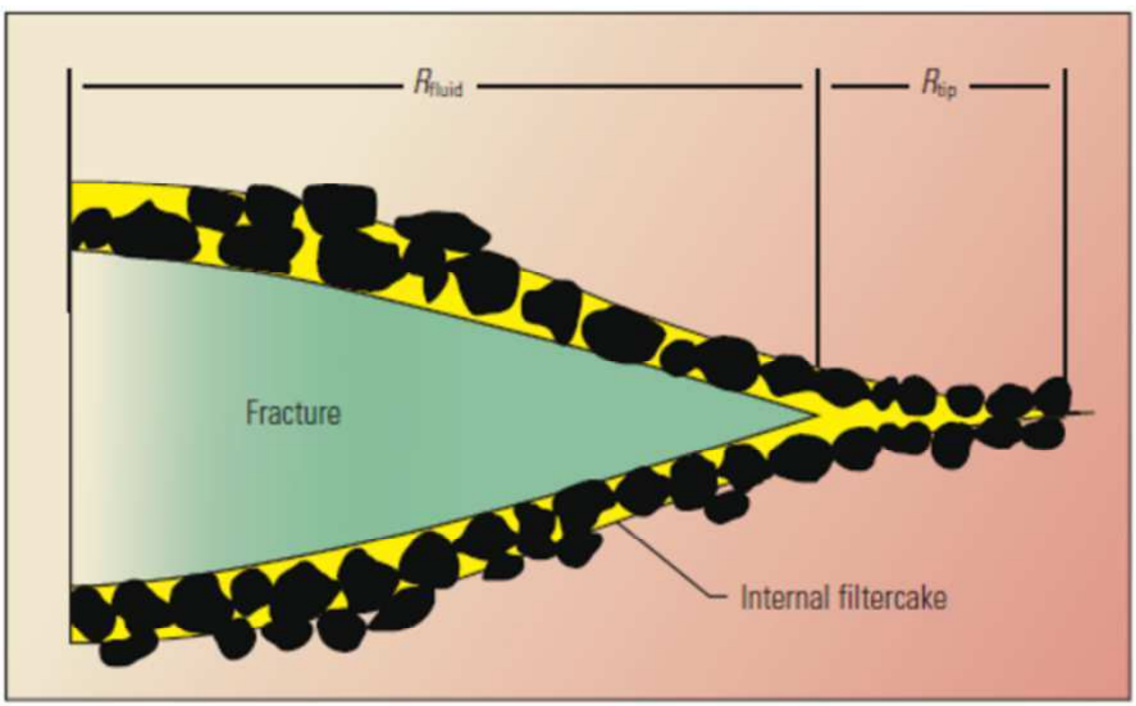

Figure 5.12 Filter cake and fracture propagation in Oil Based Mud system (Cook et al. 2012).

5.4 Hole Cleaning Performance

One approach to evaluate the hole cleaning performance is the Minimum Transport Velocity (MTV), which is defined as the minimum velocity required to initiate cuttings bed heights. Several factors that affect MTV are flow rate, angle of inclination, mud rheology, mud density, cuttings size, and rate of penetration.

MTV values for well X-51 at depth 500, 700, 1075, and 1175 m MD were calculated using empirical correlation that was developed by Larsen et al. (1997). Figure 5.13 shows MTV after being converted into Q_{crit} (critical flow rate), the critical flow rate required to lift the cuttings to the surface were far above the actual flow rate at depth 1075 and 1175 m MD, which cause cuttings to settle inside the wellbore. Figure 5.14 shows the increase of MTV values as the well inclination is higher.

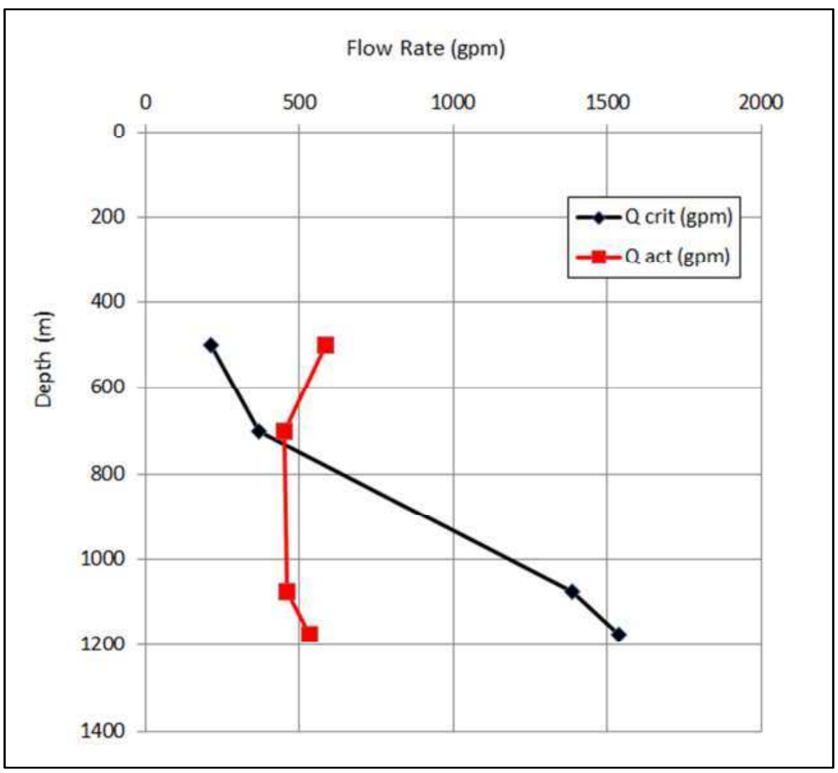

Figure 5.13 Critical and actual mud flow rate in Well X-51.

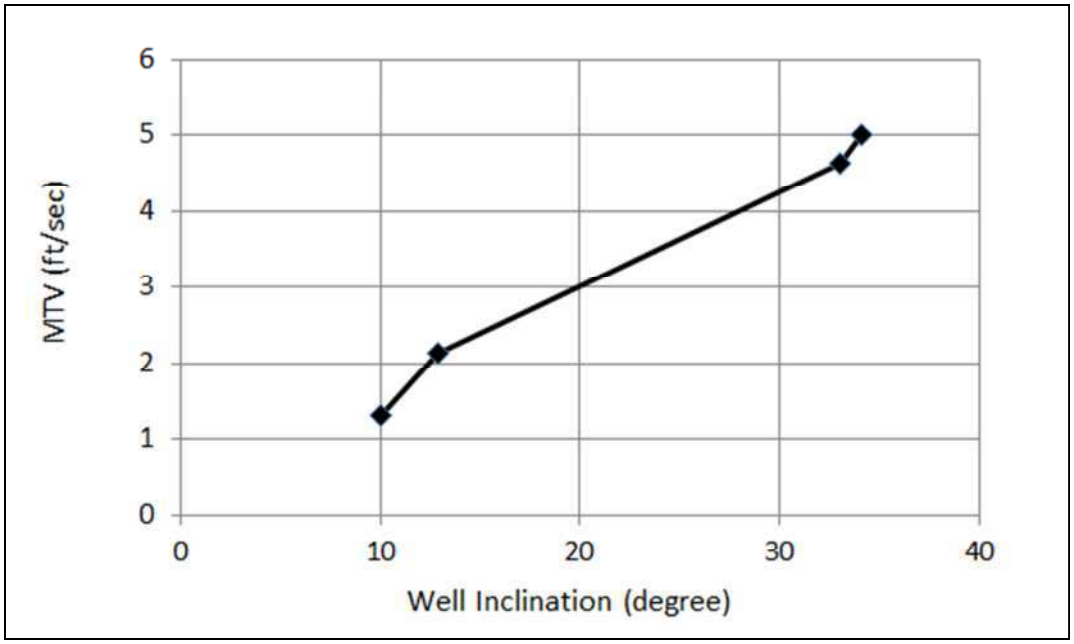

Figure 5.14 MTV for different well inclination in Well X-51.

CHAPTER 6

CONCLUSIONS AND FUTURE WORK

6.1 Conclusions

From the detailed study of the Field “X” wells, the following conclusions can be derived.

We determine through our problem diagnosis that Baong upper shale formation in the studied wells is a problematic zone with high frequency of wellbore breakout.

It was found that the well trajectory, drilling fluid density, type and chemical composition of the drilling fluid used in the operation have a significant impact on the wellbore stability in the study area.

Pre-drilling identification of overpressure zone is very important to avoid non-productive time.

The dominant stress regime around the well is strike slip faulting ($S_H>S_v>S_h$); this result is different than the geology log interpretation, where the faults regime are predicted to be reverse faulting.

Core measurements are very important to deliver reliable results. In our study, no core samples or the core data was not available to be used in the study. Yet, we have used other datasets utilizing well log data, drilling, geological data, and tectonic history to create a wellbore stability model applicable in the study area.

Risk analysis shows that the key parameters in determining the right mud weight to avoid wellbore breakouts and tensile fractures are:

- The in situ principle stresses magnitudes and orientations
- Uniaxial compressive strength
- Pore pressure
- Internal friction angle of the formation

The chemical interaction, temperature alteration, and flow induced stress also contribute towards the determination of the mud weight and customizing a formulation for the composition in the study area.

Using oil based mud can accelerate the tensile fracture propagation which leads to lost circulation.

Results of this study can help well trajectory optimization, proper mud weight determination, and reduce non-productive time (NPT) while drilling.

6.2 Future Work

The following are recommendations for future work.

1. Validate geomechanical properties using coupled true-triaxial core measurements.
2. Calibrate the magnitude of minimum horizontal stress derived from correlations by first conducting Extended LOT measurements in the wells.
3. Develop new customized correlation for the study area to determine UCS value from laboratory core measurements.

4. Investigate the formation characteristics with stress alteration in the region.
5. Upscale the geomechanics properties using reservoir simulation software.

REFERENCES

Aadnoy, B.S. and Looyeh, R. 2011. *Petroleum Rock Mechanics: Drilling Operations and Well Design*, first edition. Oxford: Gulf Professional Publishing.

Addis, M.A., Last, N.C., and Yassir, N.A. 1996. Estimation of Horizontal Stresses at Depth in Faulted Regions and Their Relationship to Pore Pressure Variations. *SPE Res Eval & Eng* **11** (1): 11-18. SPE-28140-PA. http://dx.doi.org/10.2118/ 28140-PA.

Al-Ajmi, A.M. and Zimmerman, R.W. 2006. Stability Analysis of Deviated Boreholes Using the Mogi-Coulomb Failure Criterion, with Applications to Some North Sea and Indonesian Reservoirs. Presented at the IADC/SPE Asia Pacific Drilling Technology Conference and Exhibition, Bangkok, Thailand, 13-15 November. SPE-104035-MS. http://dx.doi.org/ 10.2118/104035-MS.

Al-Ajmi, A.M. and Zimmerman, R.W. 2006. Stability Analysis of Vertical Boreholes using the Mogi-Coulomb Failure Criterion, *International Journal of Rock Mechanics and Mining Sciences* **43** (8): 1200-1211. http://dx.doi.org/10.1016/j.ijrmms.2006.04.001.

Barber, A.J., Crow, M.J., and Milsom, J.S. 2005. Sumatra: Geology, Resources and Tectonic Evolution, Issue 31. London: Geological Society of London.

Barton, C.A. and Zoback, M.D. 2002. Wellbore Imaging Technologies Applied to Reservoir Geomachanics and Environmental Engineering. *Geological Application of Well Log, AAPG Methods in Exploration* **13**: 229-239.

Biot, M.A. 1962. Generalized Theory of Acoustic Propagation in Porous Dissipative Media. *Journal of Acoustical Society of America* **34** (9A): 1254-1264. http://dx.doi.org/ 10.1121/1.1918315.

Brie, A. 2001. A Micro-Structural Model for Compressional and Shear Slowness Interpretation in Carbonates. Presented at the SPWLA 42nd Annual Logging Symposium, Houston, Texas, 17-20 June. SPWLA-2001-J.

Brocher, T.M. 2005. Empirical Relations between Elastic Wavespeeds and Density in the Earth's Crust. *Bulletin of the Seismological Society of America* **95** (6): 2081–2092. http://dx.doi. org/10.1785/0120050077.

Brocher, T.M. 2008. Key Elements of Regional Seismic Velocity Models for Long Period Ground Motion Simulations. *Journal of Seismology* **12** (2): 217–221. http://dx.doi.org/ 10.1007/s10950-007-9061-3.

Chang, C.D., Zoback, M.D., and Khaksar, A. 2006. Empirical Relations between Rock Strength and Physical Properties in Sedimentary Rocks, *Journal of Petroleum Science and Engineering* **51** (3-4): 223-237. http://dx.doi.org/10.1016/j.petrol.2006.01.003.

Chen, G., Chenevert, M.E., Sharma, M.M. et al. 2001. The Poroelastic, Chemical, and Thermal Effect on Wellbore Stability in Shales. Presented at the 38th US Rock Mechanics Symposium in Washington D.C., 7-10 July. ARMA-01-0011.

Cook, J. et al. 2012. Stabilizing the Wellbore to Prevent Lost Circulation. *Schlumberger Oilfield Review Winter 2011/2012* **23** (4): 26-35.

Davies, P.R. 1984. Tertiary Structural Evolution and Related Hydrocarbon Occurrences, North Sumatra Basin. *Indonesian Petroleum Association Proceedings 13th Annual Convention* **1**, 19-49.

Eaton, B. 1975. The Equation for Geopressure Prediction from Well Logs, Paper SPE 5544 presented at the Fall Meeting of the Society of Petroleum Engineers of AIME, Dallas, Texas, 28 September-1 October. SPE-5544-MS. http://dx.doi.org/10.2118/5544-MS.

Eissa, E.A. and Kazi, A. 1988. Relation Between Static and Dynamic Young's Moduli of Rocks. *International Journal of Rock Mechanics and Geomechanics Abstract* **25** (6): 479-482.

Eskandari, H., Rezaee, M.R., Javaherian, A. et al. 2003. Shear Wave Velocity Estimation Utilizing Wireline Logs for a Carbonate Reservoir, South-West Iran. *Iranian International Journal of Science* **4** (2): 209-221.

Ewy, R.T. 1999. Wellbore-Stability Predictions by Use of Modified Lade Criterion. *SPE Drilling and Completion* **14** (2): 85-91. SPE-56862-PA. http://dx.doi.org/10.2118/56862-PA.

Fjær, E., Holt, R.M., Horsrud, P. et al. 2008. *Petroleum Related Rock Mechanics*, second edition. Amsterdam: Elsevier.

Heidbach, O., Tingay, M., Barth, A. et al. 2010. Global Crustal Stress Pattern Based on the World Stress Map Database Release 2008. *Tectonophysics* **462 (**1-4): 3-15. http://dx.doi.org/10.1016/j.tecto.2009.1007.1023.

Hobbs, D.W. 1964. The Tensile Strength of Rocks. *International Journal of Rock Mechanics and Mining Sciences* **1** (3): 115-127. http://dx.doi.org/10.1016/0148-9062(64)90005-1.

Holbrook, P. 1999. A Simple Closed Form Force Balanced Solution for Pore Pressure, Overburden and the Principle Stresses in the Earth. *Marine and Petroleum Geology* **16** (4): 303-319. http://dx.doi.org/10.1016/S0264-8172(98)00083-X.

Islam, M.A., Skalle, P., Al-Ajmi, A.M. et al. 2010. Stability Analysis in Shale Through Deviated Boreholes Using the Mohr and Mogi-Coulomb Failure Criteria. Presented at the 44th U.S. Rock Mechanics Symposium and 5th U.S.-Canada Rock Mechanics Symposium, Salt Lake City, Utah, 27-30 June. ARMA-10-432.

Kadyrov, T. 2012. *Integrated Wellbore Stability Analysis for Well Trajectory Optimization and Field Development: The West Kazakhstan Field*. MS thesis, Colorado School of Mines, Golden, Colorado.

Krief, M., Garat, J., Stellingwerf, J. et al. 1990. A Petrophysical Interpretation Using the Velocity of P and S Waves (Full-Wave form Sonic). *The Log Analyst* **31** (6): 355.

Larsen, T.I., Pilehvari, A.A., and Azar, J.J. 1997. Development of a New Cuttings-Transport Model for High-Angle Wellbores Including Horizontal Wells. *SPE Drilling & Completion* **12** (2): 126-136. SPE-25872-PA. http://dx.doi.org/10.2118/25872-PA.

Lee, M.W. 2002. Biot-Gassmann Theory for Velocities of Gas-Hydrate-Bearing Sediments. *Geophysics* **67** (6): 1711–1719. http://dx.doi.org/10.1190/1.1527072.

Mavko, G., Mukerji T., and Dvorkin J. 2009. *The Rock Physics Handbook*, second edition. Cambridge: Cambridge Press.

McCaffrey, R. 2008. The Tectonic Framework of the Sumatran Subduction Zone. *The Annual Review of Earth and Planetary Sciences* **37**: 345-366. http://dx.doi.org/ 10.1146/annurev.earth.031208.100212.

Meckel, L.D. 2012. Exploring a 19th Century Basin in the 21st Century: Seeing the North Sumatra Basin with New Eyes. Presented at the AAPG International Conference and Exhibition, Singapore, September 16-19.

Mese, A.I. and Tutuncu, A.N. 2011. Impact of Fluids and Formation Anisotropy on Acoustic, Deformation and Failure Characteristics of Reservoir Shales and Pure Clay Minerals. Presented at the International Society of Rock Mechanics Congress, Beijing, China, 16-21 October. ISRM-12CONGRESS-2011-242.

Mitchell, R. F., Miska, S. Z., and Aadnoy, B. S. 2011. *Fundamentals of Drilling Engineering* SPE Textbook Series No. 12. Texas: Society of Petroleum Engineers.

Pasic, B., Gaurina-Medimurec, N., and Matanovic, D. 2007. Wellbore Instability: Causes and Consequences. *Rudarsko-geološko-naftni zbornik* **19**: 87-98.

Peng, S. and Zhang, J. 2007. *Engineering Geology for Underground Rocks*, first edition. New York City: Springer.

Rezaee, M. R., Kadkhodaie, A., and Barabadi, A. 2007. Prediction of Shear Wave Velocity from Petrophysical Data Utilizing Intelligent Systems: an Example from a Sandstone Reservoir of Carnarvon Basin, Australia. *Journal of Petroleum Science and Engineering* **55** (3-4): 201-212. http://dx.doi.org/10.1016/j.petrol.2006.08.008.

Riadhy, S., Ismi, C., and Iriani, S. 1998. North Sumatra's Middle Miocene Reservoir Prediction and Characterization Using Sequence Stratigraphy, 2D Seismic Inversion and 3D Seismic Data. *Indonesian Petroleum Association 26th Annual Convention Proceedings* **1**: 239-250.

Terzaghi, K., Peck, R.B., and Mesri, G. 1996. *Soil Mechanics in Engineering Practice*, third edition. New York: John Wiley & Sons.

Tutuncu, A.N. 2010. Anisotropy, Compaction and Dispersion Characteristics of Reservoir and Seal Shales. Presented at the 44th U.S. Rock Mechanics Symposium and 5th U.S.-Canada Rock Mechanics Symposium, Salt Lake City, Utah, 27-30 June. ARMA-10-344.

Tutuncu, A.N. 2014. Reservoir Geomechanics: Course Notes. Colorado School of Mines, Golden, Colorado.

Tutuncu, A.N. 2015. Advanced Well Integrity: Course Notes. Colorado School of Mines, Golden, Colorado.

Tutuncu, A.N., Podio, A.L., and Sharma, M.M. 1998. Nonlinear Viscoelastic Behavior of Sedimentary Rocks: I. Effect of Frequency and Strain Amplitude. *Geophysics* **63** (1): 184-194. http://dx.doi.org/ 10.1190/1.1444311.

Tutuncu, A.N., Podio, A.L., and Sharma, M.M. 1998. Hysteresis Effect and Influence of Type of Fluid on Elastic Moduli. *Geophysics* **63** (1): 195-204. http://dx.doi.org/10.1190/ 1.1444313.

Tutuncu A.N., Sharma M.M., and Podio A.L. 1995. Hysteresis Observed in Stress-Strain Diagrams and Their Relation to Adhesion Hysteresis and Stick-Slip Sliding in Sedimentary Granular Rocks. Presented at the 35th U.S. Symposium on Rock Mechanics (USRMS), Reno, Nevada, 5-7 June. ARMA-95-0801.

van Oort, E., Nicholson, J., and D'Agostino, J. 2001. Integrated Borehole Stability Studies: Key to Drilling at the Technical Limit and Trouble Cost Reduction. Presented at the SPE/IADC Drilling Conference, Amsterdam, Netherlands, 27 February - 1 March. SPE-67763-MS. http://dx.doi.org/10.2118/67763-MS.

Vernik, L. and Zoback, M.D. 1992. Estimation of Maximum Horizontal Principle Stress Magnitude from Wellbore Breakouts in the Cajon Pass Scientific Research Borehole. *Journal of Geophysical Research* **97** (Issue B4): 5109-5119. http://dx.doi.org/ 10.1029/91JB01673.

Wu, B. 2001. Biot's Effective Stress Coefficient Evaluation: Static and Dynamic Approaches. Presented at the ISRM 2nd Asian Rock Mechanics Symposium, Beijing, China, 11–13 September. ISRM-ARMS2-2001-082.

Yu, M., Chenevert, M.E., and Sharma, M.M. 2001. Chemical and Thermal Effects on Wellbore Stability of Shale Formations. Presented at the SPE Annual Technical Conference and Exhibition, New Orleans, Louisiana, 30 September – 3 October. SPE-71366-MS. http://dx.doi.org/10.2118/71366-MS.

Zoback, M.D. 2010. *Reservoir Geomechanics*, first edition. New York: Cambridge University Press.

NOMENCLATURE

A	= area, m^2
a	= coefficient, unitless
a	= radius of the wellbore, inches
$a_{w,df}$	= chemical activity of the fresh water, unitless
$a_{w,sh}$	= chemical activity of shale or formation pore water, unitless
b	= coefficient, unitless
b	= Coulomb strength parameter, MPa (psi)
c	= coefficient, unitless
C	= formation cohesion, MPa (psi)
E	= Young's modulus, GPa (Mpsi)
F	= force, N ($kg.m/s^2$)
F_n	= normal force, N ($kg.m/s^2$)
F_s	= parallel force, N ($kg.m/s^2$)
E_d	= dynamic Young's modulus, GPa (Mpsi)
E_s	= static Young's modulus, GPa, (Mpsi)

r	= outer radius, inches
g	= gravitational acceleration, m/s^2
GR	= gamma ray, gAPI
G	= shear modulus, GPa (Mpsi)
I_m	= reactivity coefficient, unitless
K	= bulk modulus, GPa, (Mpsi)
K_d	= dynamic bulk modulus, GPa (Mpsi)
M	= compressional modulus, GPa (Mpsi)
MTV	= minimum transport velocity, ft/sec
P_p	= pore pressure, MPa (psi)
P_{wb1}	= critical wellbore breakout pressure, MPa (psi)
P_{wf1}	= critical wellbore breakdown pressure, MPa (psi)
Q_{crit}	= critical mud flow rate, gpm
R	= the universal gas constant, (J/K.mole)
S	= stress tensor, MPa (psi)
S_{Hmax}	= maximum horizontal stress, MPa (psi)
S_{hmin}	= minimum horizontal stress, MPa (psi)

S_v	= overburden stress, MPa (psi)
T	= circulation temperature, °K
T_o	= absolute temperature, °K
T_s	= tensile strength, MPa (psi)
UCS	= uniaxial compressive strength, MPa (psi)
V_p	= compressional-wave velocity, m/sec (ft/sec)
V_s	= shear-wave velocity, m/sec (ft/sec)
z	= depth, m (ft)
$\mathrm{z_w}$	= water depth, m (ft)
α	= Biot's coefficient, unitless
β	= compaction strain-hardening coefficient, unitless
γ	= wellbore inclination from the vertical, degrees
ΔP	= difference between wellbore pressure and pore pressure, MPa (psi)
Δt_{co}	= compressional-wave slowness, μsec/ft (μsec/m)
Δt_s	= shear-wave slowness, μsec/ft (μsec/m)
$\Delta\Pi$	= osmotic pressure, MPa (psi)
ρ	= bulk density, g/cm^3 (kg/m^3)

ρ_w = water density, g/cm^3 (kg/m^3)

σ = stress, MPa (psi)

σ_1 = maximum principle stress, MPa (psi)

σ_2 = intermediate principle stress, MPa (psi)

σ_3 = minimum principle stress, MPa (psi)

σ_{eff} = effective stress, MPa (psi)

$\sigma_{m,2}$ = effective mean stress, MPa (psi)

σ_{max} = effective stress required to reduce the mineral porosity to zero, MPa (psig)

σ_n = normal stress, MPa (psi)

σ_r = radial stress at the wellbore, MPa (psi)

σ_{rr} = radial effective principle stress at the wellbore, MPa (psi)

σ_r' = radial stress alteration due to the introduction of osmotic pressure, MPa (psi)

σ_r'' = radial stress alteration due to the flow-induced stress effect, MPa (psi)

σ_T = thermal stress, MPa (psi)

σ_{tmax} = maximum effective principle stress at the wellbore, MPa (psi)

σ_{tmin} = minimum effective principle stress at the wellbore, MPa (psi)

σ_x = stress in x-axis in Cartesian coordinate system, MPa (psi)

σ_y = stress in y-axis in Cartesian coordinate system, MPa (psi)

σ_z = axial stress at the wellbore, MPa (psi)

σ_{zz} = stress in z-axis in Cartesian coordinate system, MPa (psi)

σ_z' = axial stress alteration due to the introduction of osmotic pressure, MPa (psi)

σ_z'' = axial stress alteration due to the flow-induced stress effect, MPa (psi)

$\sigma_{\theta\theta}$ = hoop stress at the wellbore, MPa (psi)

σ_θ' = hoop stress alteration due to the introduction of osmotic pressure, MPa (psi)

σ_θ'' = hoop stress alteration due to the flow-induced stress effect, MPa (psi)

τ = shear stress, MPa (psi)

τ_{max} = maximum shear stress, MPa (psi)

τ_{oct} = octahedral shear stress, MPa (psi)

τ_{xy} = shear stress in x-y plane, MPa (psi)

τ_{xz} = shear stress in x-z plane, MPa (psi)

τ_{yz} = shear stress in y-z plane, MPa (psi)

τ_{rz} = shear stress in r-z plane, MPa (psi)

$\tau_{r\theta}$ = shear stress in r- plane, MPa (psi)

$\tau_{\theta z}$ = shear stress in θ-z plane, MPa (psi)

υ = Poisson's ratio, unitless

Φ = internal friction angle, degrees

φ = wellbore azimuth from the direction of , degrees

Ø = formation porosity, fraction